ARO 22806.17-EG

(2)

AD-A210 713

STUDIES IN PENETRATION MECHANICS

FINAL REPORT

R.C. BATRA

June 1989

U.S. ARMY RESEARCH OFFICE

CONTRACT NO. DAAG29-85-K-0238

UNIVERSITY OF MISSOURI - ROLLA
ROLLA, MO 65401

DTIC
ELECTE
AUG 0 2 1989
S D
B

APPROVED FOR PUBLIC RELEASE
DISTRIBUTION UNLIMITED

89 7 31 115

THE VIEW, OPINIONS, AND/OR FINDINGS CONTAINED IN THIS REPORT ARE THOSE OF THE AUTHOR(S) AND SHOULD NOT BE CONSTRUED AS AN OFFICIAL DEPARTMENT OF THE ARMY POSITION, POLICY, OR DECISION, UNLESS SO DESIGNATED BY OTHER DOCUMENTATION.

UNCLASSIFIED MASTER COPY - FOR REPRODUCTION PURPOSES

SECURITY CLASSIFICATION OF THIS PAGE

REPORT DOCUMENTATION PAGE

1a. REPORT SECURITY CLASSIFICATION: Unclassified	1b. RESTRICTIVE MARKINGS
2a. SECURITY CLASSIFICATION AUTHORITY	3. DISTRIBUTION / AVAILABILITY OF REPORT: Approved for public release; distribution unlimited.
2b. DECLASSIFICATION / DOWNGRADING SCHEDULE	
4. PERFORMING ORGANIZATION REPORT NUMBER(S)	5. MONITORING ORGANIZATION REPORT NUMBER(S): ARO 22806.17-EG
6a. NAME OF PERFORMING ORGANIZATION: University of Missouri-Rolla; 6b. OFFICE SYMBOL (If applicable)	7a. NAME OF MONITORING ORGANIZATION: U. S. Army Research Office
6c. ADDRESS (City, State, and ZIP Code): Rolla, MO 65401-0249	7b. ADDRESS (City, State, and ZIP Code): P. O. Box 12211 Research Triangle Park, NC 27709-2211
8a. NAME OF FUNDING / SPONSORING ORGANIZATION: U. S. Army Research Office; 8b. OFFICE SYMBOL (If applicable)	9. PROCUREMENT INSTRUMENT IDENTIFICATION NUMBER: DAAG29-85-K-0238
8c. ADDRESS (City, State, and ZIP Code): P. O. Box 12211 Research Triangle Park, NC 27709-2211	10. SOURCE OF FUNDING NUMBERS: PROGRAM ELEMENT NO; PROJECT NO; TASK NO; WORK UNIT ACCESSION NO

11. TITLE (Include Security Classification): Studies in Penetration Mechanics

12. PERSONAL AUTHOR(S): R. C. Batra

13a. TYPE OF REPORT	13b. TIME COVERED	14. DATE OF REPORT (Year, Month, Day)	15. PAGE COUNT
Final	FROM 9/23/85 TO 3/22/89	89-6-14	115

16. SUPPLEMENTARY NOTATION: The view, opinions and/or findings contained in this report are those of the author(s) and should not be construed as an official Department of the Army position, policy, or decision, unless so designated by other documentation.

17. COSATI CODES		
FIELD	GROUP	SUB-GROUP

18. SUBJECT TERMS (Continue on reverse if necessary and identify by block number): Steady State Deformations, Thermoviscoplasticity, Shear Bands, Penetration, Term...

19. ABSTRACT (Continue on reverse if necessary and identify by block number)

The details of a steadily growing plastic flow field a short while after a thick target has been impacted by a deformable penetrator have been studied with the ultimate objectives of identifying key material and kinematic variables that should be included in developing engineering models of target penetration. The problems studied include the axisymmetric thermomechanical deformations of a viscoplastic target being penetrated by a rigid cylindrical penetrator, and of a viscoplastic rod striking a known hemispherical rigid cavity. The effects of heat generated due to plastic deformations, compressibility of the material, work-hardening, strain-rate hardening, thermal softening, and the shape of the penetrator nose in the former case and the cavity shape for the latter problem have been investigated.

The material parameters that enhance/retard the initiation and growth of shear bands in viscoplastic materials undergoing overall adiabatic simple shearing deformations have

20. DISTRIBUTION / AVAILABILITY OF ABSTRACT	21. ABSTRACT SECURITY CLASSIFICATION
☐ UNCLASSIFIED/UNLIMITED ☐ SAME AS RPT. ☐ DTIC USERS	Unclassified
22a. NAME OF RESPONSIBLE INDIVIDUAL	22b. TELEPHONE (Include Area Code) / 22c. OFFICE SYMBOL

DD FORM 1473, 84 MAR — 83 APR edition may be used until exhausted. All other editions are obsolete.

SECURITY CLASSIFICATION OF THIS PAGE

UNCLASSIFIED

also been delineated.

TABLE OF CONTENTS

1. Statement of the Problem Studied 1

2. Summary of the Most Important Results 3

3. Brief Review of the Completed Work 4

4. List of Publications 12

5. List of Participating Scientific Personnel 16

6. Bibliography 17

7. Appendix 19

Accession For
NTIS GRA&I ☑
DTIC TAB ☐
Unannounced ☐
Justification
By
Distribution/
Availability Codes
Dist | Avail and/or Special
A-1

I. STATEMENT OF THE PROBLEM STUDIED

In simple theories of penetration, the material properties of target and penetrator are often represented only by constant characteristic stresses, as for example in Tate [1]. Although this approach leads to results that are qualitatively correct, it can be difficult to use quantitatively. Some problems have to do with actual deformations in target and penetrator including lateral motion, and others are associated with the fact that the plastic flow stress is determined only by the deviatoric components of stress whereas the spherical or pressure component, which may be quite large ahead of the penetrator and contributes significantly to the retardation of the penetrator, is unrelated to flow stress (e.g. see Wright [2]). Wright [2], in his survey article on long rod penetrators, ellucidated vividly some of the problems with the existing penetration models. In another extensive review article, Backman and Goldsmith [3] discussed superbly the work done in penetration mechanics until 1977. Jonas and Zukas [4] reviewed various analytical methods for the study of kinetic energy projectile-armor interaction at ordance velocities and placed particular emphasis on three-dimensional numerical simulation of perforation. Anderson and Bodner [5] have recently reviewed the status of the ballistic impact modeling. A penetration model that is not too difficult to use has been proposed by Ravid and Bodner [6]. They studied the penetration problem by presuming a kinematically admissible flow field in the target and found the unknown parameters by utilizing an upper bound theorem of plasticity modified to include dynamics effects.

In an attempt to shed some light on questions raised by Wright [2], Batra and Wright [7] recently studied an idealized penetration problem that simulates the following situation. Suppose that the penetrator is in the intermediate stages of penetration so that the active target/penetrator interface is at least one or two penetrator diameters away from either target face, and the

remaining penetrator is much longer than several diameters and is still traveling at a speed close to its striking velocity. This situation has been idealized as follows. It is assumed that the rod is semi-infinite in length, the target is infinite with a semi-infinite hole, the rate of penetration and all flow fields are steady as seen from the nose of the penetrator, and that no shear stress can be transmitted across the target/penetrator interface. This last assumption is justified on the grounds that a thin layer of material at the interface either melts or is severely degraded by adiabatic shear. These idealizations make it possible to decompose the penetration problem into two parts in which either a rigid rod penetrates a deformable target or a deformable rod is upset at the bottom of a hole in a rigid target. Of course, in the combined case the contour of the hole is unknown, but if it can be chosen so that normal tractions match in the two cases along the entire boundary between penetrator and target, then the complete solution is known irrespective of the relative motion at the boundary. Even without matching the normal tractions, it would seem that valuable qualitative information about the flow field and distribution of stresses can be gained if the chosen contour is reasonably close to that found in experiments.

We have continued the work initiated by Batra and Wright [7], and have studied the axisymmetric thermomechanical steady state deformations of a viscoplastic target being penetrated by a rigid cylindrical penetrator, and of a viscoplastic rod striking a known hemispherical rigid cavity. The effects of heat generated due to plastic deformations, compressibility of the material, work-hardening, strain-rate hardening, thermal softening, and the shape of the penetrator nose in the former case and the cavity shape for the latter problem have been investigated.

Another important and still totally unresolved problem is that of selecting the most appropriate constitutive relation for the material of the body.

The constitutive relation employed should adequately model the material response over the range of deformations expected to occur in the problem. However, the computed values of the deformation fields generally depend strongly upon the constitutive assumptions made. A way out of this dilemma is to choose a constitutive relation, solve the problem, check if the constitutive assumptions are valid over the range of computed deformations, and, if necessary, resolve the problem with the modified constitutive relation.

In the last few years, many new theories [8-10] of large deformation elasto-plasticity have been proposed. These theories make different kinematic assumptions thus necessitating the hypothesizing of constitutive relations for variables which may not be simply related with each other. In an attempt to determine which of these theories is the most appropriate for the analysis of penetration problems; we find the histories of the effective stress, second invariant of the strain-rate tensor, the temperature and the spin at a viscoplastic target particle being penetrated by a long rigid cylindrical penetrator.

An important failure mechanism in penetration mechanics is the development of adiabatic shear bands at or near the target/penetrator interface. In order to increase our understanding of the factors that enhance/retard the initiation and growth of adiabatic shear bands, we have analyzed the dynamic deformations of a viscoplastic block undergoing simple shearing deformations. The material inhomogeneity or defect has been modelled by assuming an initial non-uniform temperature distribution within the block.

Results for the aforementioned problems are summarized below.

II. SUMMARY OF THE MOST IMPORTANT RESULTS

From the results completed under this contract, the following salient conclusions can be drawn.

1) The peak hydrostatic pressure at a material particle is nearly 12 times its yield stress in a quasistatic simple compression test.

2) The plastic spin at a material particle is of the same order of magnitude as the plastic strain-rate at that particle.

3) Severest target deformations occur near the periphery of the blunt nose. The peak strain-rates there and in the target material ahead of the penetrator nose periphery are approximately an order of magnitude higher than that at other points. Also, for all nose shapes, strain-rates at target particles abutting the penetrator nose are very high and drop off rapidly within a short distance. The exact thickness of this layer has not yet been ascertained.

4) For a thermoviscoplastic rod striking a rigid cavity, peak strain-rates occur within the rod material adjacent to the cavity wall, and near the bottom-most point of the free surface.

5) The maximum temperature computed in the two problems equalled nearly one-half of the presumed melting temperature for the deformable material.

6) The presence of multiple initial imperfections delays considerably the initiation of shear bands as compared to the case when there is only one initial perturbation.

7) The consideration of dipolar effects delays the initiation of shear bands, and inertia forces start playing a noticeable role at an applied overall strain-rate of 5,000 s^{-1}.

III. BRIEF REVIEW OF THE COMPLETED WORK

In their analysis of the steady state axisymmetric deformations of a rigid perfectly/plastic target Batra and Wright [7] found that the nondimensional resisting force F acting on the hemispherical-nosed rigid cylindrical

penetrator is given by

$$F = 3.903 + 0.0773\,\alpha,\ 1 \le \alpha \le 5, \qquad (1)$$

where $\alpha = \rho v_o^2/\sigma_o$ is a nondimensional number, ρ is the mass density of the target material, σ_o its yield stress, and v_o is the striking speed of the penetrator. Wright [11] recently used this result to estimate one of the terms in his re-examination of Tate's theory. Wright [2] and Pidsley [12] have pointed out that if the equation of motion for steady flow is integrated along the central streamline, there is a contribution from transverse gradients of shear stress, unlike the case for a perfect fluid. Figure 1, taken from Batra and Wright's paper, shows the contributions from various terms and clearly establishes that the transverse gradients of shear stress make a significant contribution to the total and that the deviatoric component stays constant at approximately 0.75 (compared to the theoretical exact value of 0.667) out of a total of 8.5.

Batra [13] studied the effect of the nose shape and various material parameters on the steady-state penetration of viscoplastic targets by rigid cylindrical penetrators. The constitutive relation for the viscoplastic material was taken to be

$$\sigma = -p\,1 + \sigma_o(1 + bI)^m D/\sqrt{3I},\ 2I = \mathrm{tr}D^2\ , \qquad (2)$$

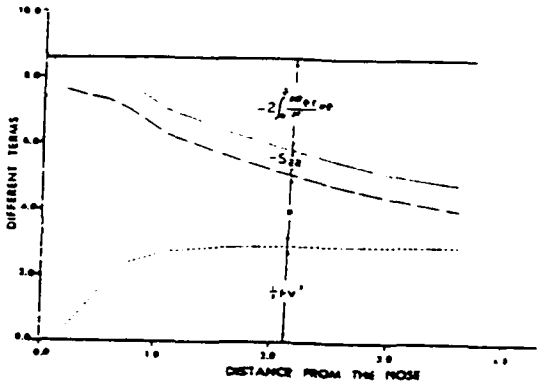

Figure 1. Contribution of Various Terms in the Bernoulli Equation.

where **D** is the stretching tensor, σ_o the yield stress in simple compression, σ the Cauchy stress tensor, p the hydrostatic pressure not determined by the deformation history of the target, and b and m are material parameters. Figure 2 shows that the change in nose shape from hemispherical to ellipsoidal reverses the curvature of the normal stress versus the angular position curve from convex downwards to concave downwards. Also, as is evident from Figure 3, the axial resisting force depends strongly upon the nose shape and rather weakly upon m and α.

When the effects of work-hardening of the target material are also considered, and the constitutive relation (2) is changed to

$$\sigma = -p\,\mathbf{1} + \sigma_o/(1 + bI)^m\left(1 + \frac{\psi}{\psi_o}\right)^n \mathbf{D}/\sqrt{3I} \qquad (3)$$

where ψ_o and n are material parameters, and ψ is an internal variable whose growth depends upon the plastic working, Batra [14] noticed that the results are very sensitive to the finite element mesh used. This is due to the absence of any diffusive term in the constitutive relation for ψ. Subsequently, Batra [15] accounted for material softening caused by the temperature rise due to plastic working and modified the constitutive relation to

$$\sigma = -p\,\mathbf{1} + \sigma_o (1 + bI)^m\left(1 + \frac{\psi}{\psi_o}\right)^n(1 - \gamma\theta)\,\mathbf{D}/\sqrt{3I} \qquad (4)$$

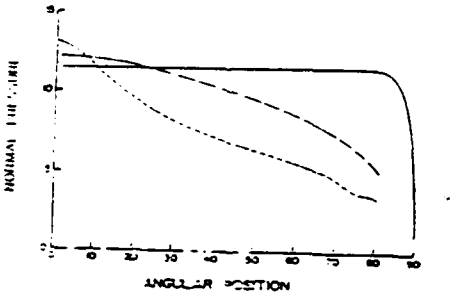

Figure 2. Distribution of the normal pressure on the penetrator nose for three different nose shapes. _____ Blunt nose (r_n/r_o = 0.2); _·_·_·_ hemispherical nose (r_n/r_o = 1.0); ----- ellipsoidal nose (r_n/r_o = 2.0).

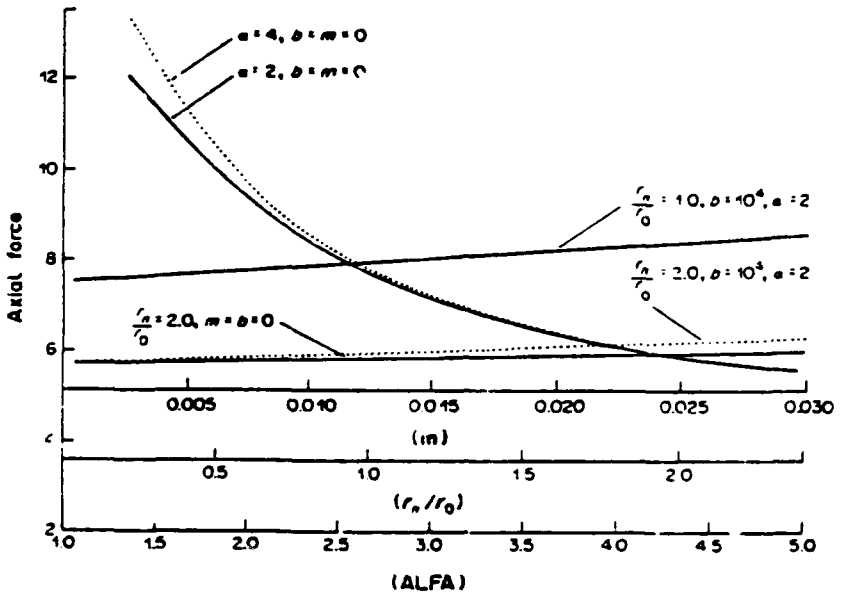

Figure 3. Dependence of the axial force upon various factors.

where γ is the thermal softening coefficient, and θ the temperature rise. For values of material parameters that correspond to a typical steel, Batra [15] computed the strain-rate distribution depicted in Figure 4. This agrees qualitatively with the experimental observation of Wingrove [16] that a shear band forms and thus very high rates occur in the target material near the periphery of a flat-ended projectile (cf. Fig. 5). Figure 6, taken from Lin and Batra's [17] paper, shows the stress and strain-rate histories at three material particles that were near the centroidal axis in the undeformed target being penetrated by a blunt-nosed penetrator. The time is clocked from the

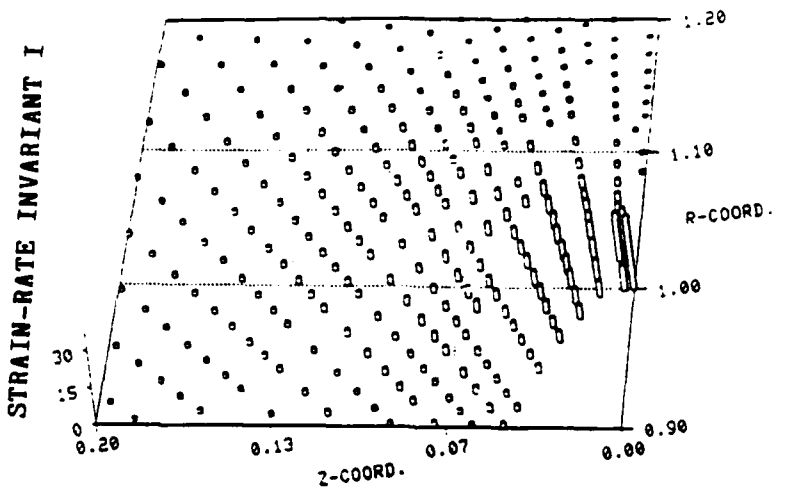

Figure 4. Distribution of the strain-rate invariant I near the periphery of a blunt-nosed penetrator.

Figure 5. Shear band produced below a flat-ended projectile showing the extent of shear in the band. Projectile velocity 140 m/s, flat-nosed penetrator. (Wingrove [16])

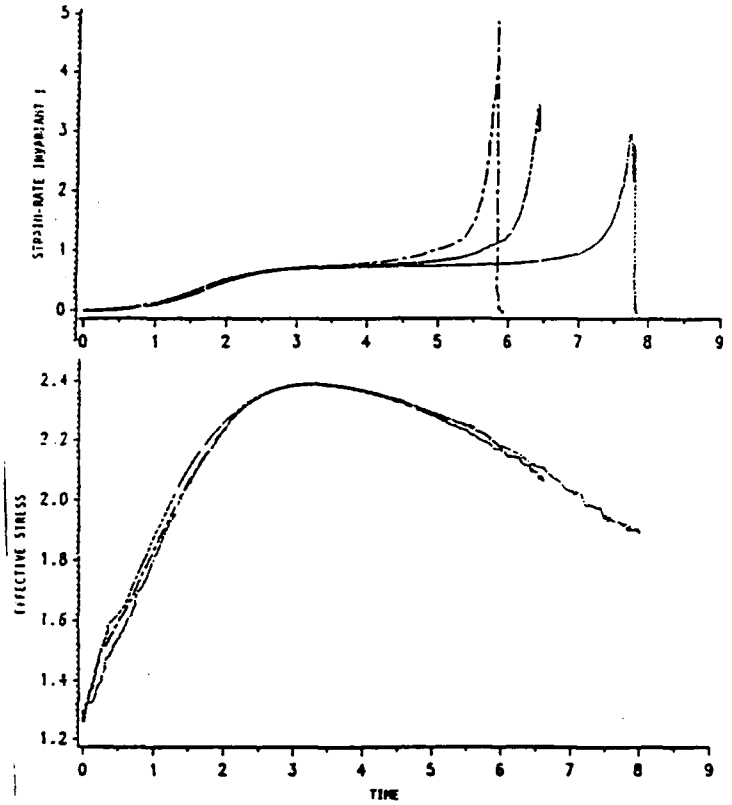

Figure 6. Histories of stress and strain-rate at three material particles that were initially near the centroidal axis.

instant these particles are on the boundary of the spatial domain analyzed. Clearly the effective stress at each of these particles attains a maximum and then decreases slowly due to the softening caused by the temperature rise. This drop in the stress is more pronounced for a blunt nosed penetrator as compared to that for a hemispherical nosed one. Since a shear band usually initiates at a point after the stress there has reached the peak value, there is more likelihood of a band being formed for a blunt-nosed penetrator as compared to that for a hemispherical one.

Batra and Gobinath [18] showed that the compressibility of the target material reduces the axial resisting force experienced by the penetrator by nearly 10 percent, and the peak values of the strain-rate invariant I and the normal stress, both of which occur at the target particle situated on the

penetrator nose-tip, by 8.8 percent and 3.2 percent, respectively.

Batra and Lin [19] have analyzed the steady state axisymmetric deformations of a rod striking a rigid cavity. This problem is more challenging than the one involving a deformable target and rigid penetrator because of the presence in it of a free surface whose shape is not known a priori. When the rod material is assumed to exhibit strain and strain-rate hardening and thermal softening, the axial force experienced by the rod was found to depend strongly upon α, the peak value of the nondimensional strain-rate invariant was found to depend weakly upon α, and the maximum temperature equal to nearly one-third the presumed melting temperature of the rod was found to occur. All of the material particles abutting the cavity wall had the same temperature, as shown in Figure 7. Figure 8 depicts the history of the effective stress at four material particles, two of which initially are located near the centroidal

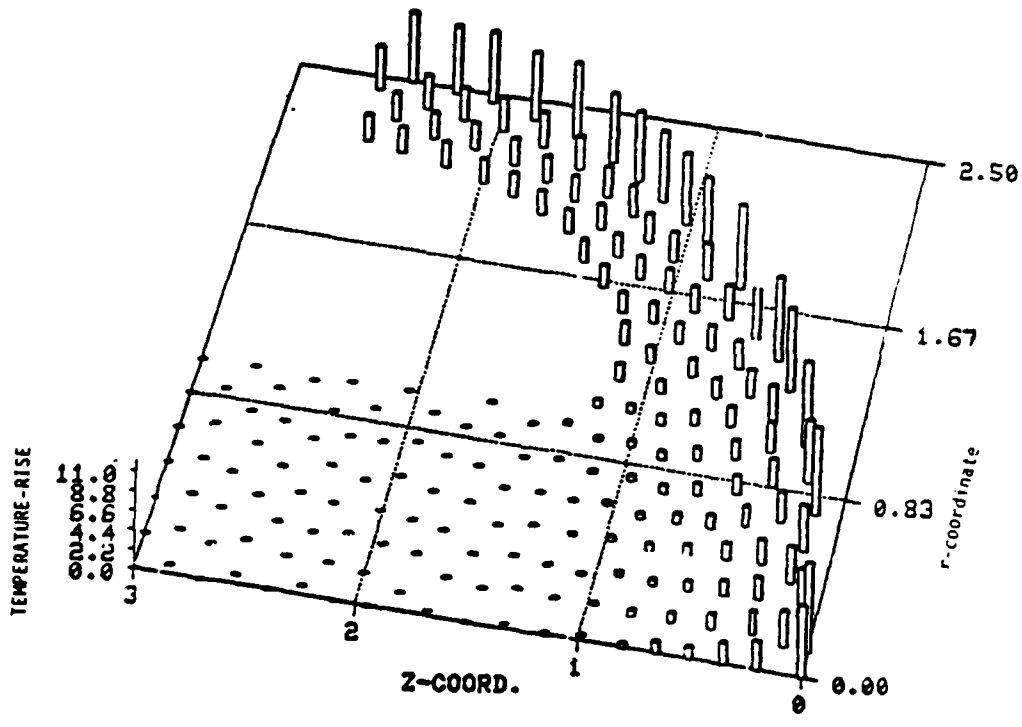

Figure 7. Temperature distribution in a viscoplastic rod upset at the bottom of a hemispherical cavity.

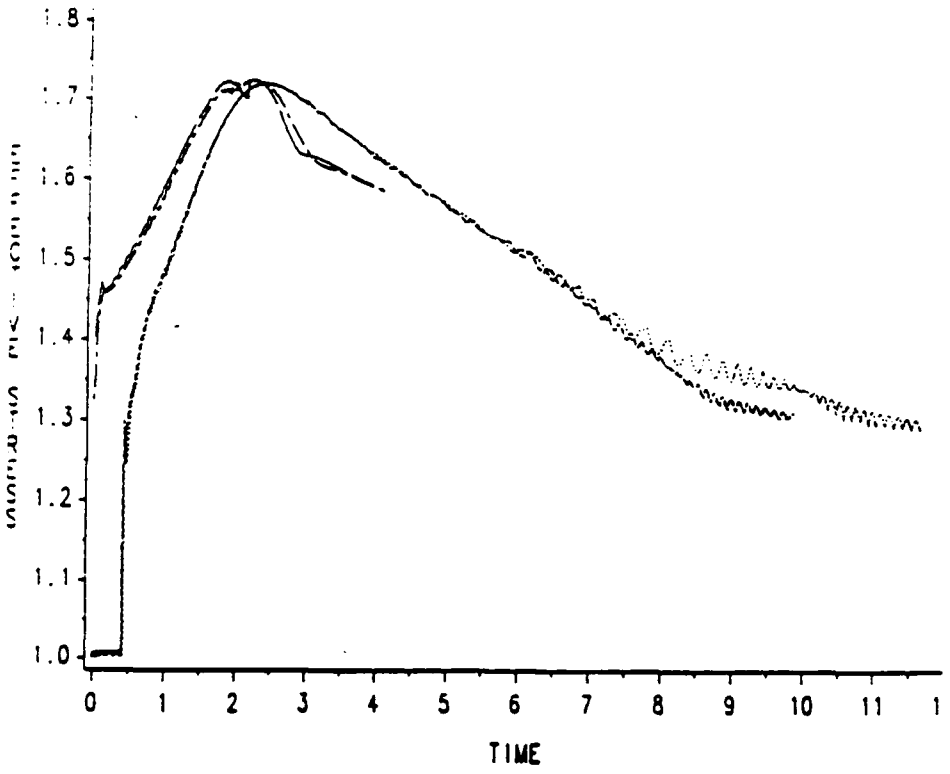

Figure 8. Stress histories at four material particles, two of these particles are initially near the centroidal axis and the other two are near the free surface.

axis and the other two near the free surface of the undeformed rod. The stress history experienced by the material particles initially near the centroidal axis suggests that the likelihood of a shear band being formed near the cavity wall is quite high.

In each of the two aforementioned problems, the peak hydrostatic pressure at a material point was found to be nearly twelve times the flow stress of the material and the peak plastic spin to be 10^5-10^6 sec^{-1}. We note that the constitutive relation employed neither accounted for the dependence of the flow stress upon the hydrostatic pressure nor accorded any importance to the plastic spin. Also, no fracture or failure criterion was included in the model.

In problems aimed at developing an understanding of factors that enhance/retard the initiation and growth of adiabatic shear bands in armor

materials, we found that the consideration of dipolar effects [20] delays significantly the initiation of adiabatic shear bands. Shear bands initiating at neighboring defects that would grow independently in nonpolar materials seem to merge together and develop as a single band in dipolar materials. Inertia forces start playing a significant role [21] when the applied strain-rate in a simple shearing problem exceeds 5,000 sec^{-1}. During the time the deformation is localizing, the shear stress in the region of localization collapses and, if the rate of collapse of the stress is dramatic, an unloading elastic wave emanates [22] out of this region.

IV. LIST OF PUBLICATIONS

A. PUBLICATIONS

1. R. C. Batra, "Steady State Penetration of Viscoplastic Targets", Intl. J. Eng. Science, 25, 1131-1141, 1987.
2. R. C. Batra, "Steady State Penetration of Thermoviscoplastic Targets", Computational Mechanics, 3, 1-12, 1988.
3. R. C. Batra, "Effect of Nose Shape and Strain-Hardening on Steady State Deformations of Viscoplastic Targets", in Computational Plasticity, Models, Software and Applications (D. R. J. Owen, E. Hinton and E. Onate, eds.), pp. 463-475, Pineridge Press, Swansea, U.K. 1987).
4. R. C. Batra and Pei-Rong Lin, "Steady State Deformations of a Rigid Perfectly Plastic Rod Striking a Rigid Cavity", Intl. J. Eng. Sci., 26, 183-192, 1988.
5. R. C. Batra and Pei-Rong Lin, "On Deformable Viscoplastic Penetrators" in Developments in Mechanics, W. Soedel and J. F. Hamilton eds., Vol. 14(a), 125-130, Purdue Univ., 1987.

6. R. C. Batra and T. Gobinath, "Steady State Penetration of Compressible Rigid Perfectly Plastic Targets", Intl. J. Eng. Sci., 26, 741-751, 1988.

7. R. C. Batra and Pei-Rong Lin, "Steady State Axisymmetric Deformations of a Thermoviscoplastic Rod Striking a Hemispherical Rigid Cavity", Intl. J. Impact Eng., 8, 1989 (to appear).

8. Pei-Rong Lin and R. C. Batra, "Histories of the Stress, Strain-Rate, Temperature, and Spin in Steady State Penetration Problems", Intl. J. Eng. Sci., 27, 1989 (to appear).

9. R. C. Batra, "The Initiation and Growth of, and the Interaction Among, Adiabatic Shear Bands in Simple and Dipolar Materials", Intl. J. Plasticity, 3, 75-89, 1987.

10. R. C. Batra, "Effect of Material Parameters on the Initiation and Growth of Adiabatic Shear Bands", Intl. J. Solids Structures, 23, 1435-1446, 1987.

11. R. C. Batra and C. H. Kim, "On the Interaction Among Adiabatic Shear Bands", in Developments in Mechanics, W. Soedel and J. F. Hamilton, eds., Vol. 14(a), 117-122, Purdue Univ., 1987.

12. R. C. Batra, "Effect of Nominal Strain-Rate on the Initiation and Growth of Adiabatic Shear Bands in Steels", J. Appl. Mechs., 55, 229-230, 1988.

13. Y. W. Kwon and R. C. Batra, "Effect of Multiple Initial Imperfactions on the Initiation and Growth of Adiabatic Shear Bands in Nonpolar and Dipolar Materials", Intl. J. Eng. Sci., 26, 1177-1187, 1988.

14. R. C. Batra and C. H. Kim, "Adiabatic Shear Banding in Elastic-Viscoplastic Nonpolar and Dipolar Materials", Intl. J. Plasticity (in press).

B. **PRESENTATIONS**

1. T. W. Wright and R. C. Batra, On Adiabatic Shear Bands, U. S. Army Workshop on Dynamic Deformation and Fracture, Leesburg, VA, May 1986.
2. R. C. Batra, Steady State Penetration of Viscoplastic Targets, 10th U.S. National Congress of Applied Mechanics, The University of Texas at Austin, June 1986.
3. R. C. Batra, Steady State Penetration of Strain and Strain-Rate Hardening Targets, 23rd Annual Meeting of the Society of Engr. Science, Buffalo, August 1986.
4. R. C. Batra and Pei-Rong Lin, On Deformable Penetrators Striking a Rigid Cavity, 1st World Congress on Computational Mechanics, The University of Texas at Austin, Austin, September 1986.
5. R. C. Batra, Steady State Penetration of Thermo-viscoplastic Targets, Univ. of Oklahoma, Norman, September 1986.
6. R. C. Batra, Adiabatic Shear Bands in Viscoplasticity, 29th Annual Meeting of the Society for Natural Philosophy, Univ. of Virginia, Charlottesville, October 1986.
7. R. C. Batra, Effect of Nose Shape and Strain Hardening on Steady State Penetration of Viscoplastic Targets, Int. Conf. on Computational Plasticity, Barcelona, Spain, April 1987.
8. R. C. Batra, Adiabatic Shear Banding, Technical University of Berlin, West Germany, June 1987.
9. R. C. Batra and C. H. Kim, The Interaction Among Adiabatic Shear Bands, 20th Midwestern Mechanics Conference, Purdue University, August-September 1987.
10. R. C. Batra and De-Shin Liu, Adiabatic Shear Bands in Plane Strain Problems, 20th Midwestern Mechanics Conference, Purdue University, August-September 1987.

11. R. C. Batra and Pei-Rong Lin, On Deformable Viscoplastic Penetrators, 20th Midwestern Mechanics Conference, Purdue University, August-September 1987.

12. R. C. Batra and T. Gobinath, Steady State Penetration of Compressible Rigid Perfectly Plastic Targets, 20th Midwestern Mechanics Conference, Purdue University, August-September 1987.

13. R. C. Batra, Steady State Penetration of Metallic Targets by Ogive-Nosed Penetrators, 24th Annual Meeting of the Society of Engineering Science, University of Utah, September 1987.

14. R. C. Batra, Solutions of the Steady State Thermoviscoplastic Problem by the Galerkin and the Petrov-Galerkin Formulation, Int. Conf. Engineering Science, Atlanta, April 1988.

15. R. C. Batra and T. Gobinath, On Axisymmetric Steady State Penetration Problems, Joint SES/ASME Conference, CA, June 1988.

V. PARTICIPATING SCIENTIFIC PERSONNEL

Persons, besides the principal investigator, who participated in the completion of the project in any meaningful way are listed below.

1. Pei-Rong Lin, Ph.D., May, 1988

   Dissertation Title: An Analysis of Steady State Penetration Problems by the Finite Element Method

2. De-Shin Liu, Ph.D., Jan. 1989

   Dissertation Title: Dynamic Adiabatic Shear Band Development in Plane Strain Deformations of a Viscoplastic Material

3. Chang-Ho Kim, Ph.D., Feb. 1989

   Dissertation Title: Shear Strain Localization in Elastic-Viscoplastic Materials

4. T. Gobinath, Ph.D., Dissertation work in progress
5. R. Jayachandran, Ph.D., Dissertation work in progress

Other persons who received some financial support from the grant are:

1. Lindley W. Bark
2. Mike Hilgers
3. Eddy Deng
4. Yixia Zhou

BIBLIOGRAPHY

1. A. Tate, J. Mech. Phys. Solids, 15, 387 (1967).
2. T. W. Wright, A Survey of Penetration Mechanics for Long Rods Lecture Notes in Engineering, Vol. 3, Computational Aspects of Penetration Mechanics (Edited by J. Chandra and J. Flaherty). Springer-Verlag, New York (1983).
3. M. E. Backman and W. Goldsmith, Int. J. Engr. Sci. 16, 1, 1978.
4. G. H. Jonas and J. A. Zukas, Int. J. Engr. Sci., 16, 879 (1978).
5. C. E. Anderson and S. R. Bodner, Int. J. Impact Engr., 7, 9 (1988).
6. M Ravid and S. R. Bodner, Int. J. Engr. Sci., 21, 577 (1983).
7. R. C. Batra and T. W. Wright, Int. J. Engr. Sci., 24, 41 (1986).
8. L. Anand, J. Appl. Mech., 47, 439 (1980).
9. S. Nemat-Nasser, Proc. Symp. Today (A. Sawczuk, Ed.) Elsevier Applied Science, London (1983).
10. Y. F. Dafalias, Current Theories of Plasticity and Their Applications, Univ. of Oklahoma-Norman (1984).
11. T. W. Wright, Proc. Joint SES/ASME - AMD Conf., Univ. of California-Berkeley, June 1988.
12. P. H. Pidsley, J. Mech. Phys. Solids, 32, 315 (1984).
13. R. C. Batra, Int. J. Engr. Sci., 25, 1131 (1987).
14. R. C. Batra, Effect of Nose Shape and Strain-Hardening on Steady State Penetration of Viscoplastic Targets, Computational Plasticity, Models, Software and Applications (D. R. J. Owen, E. Hinton and E. Onate eds.) Pineridge Press Ltd., Swansea (1987).
15. R. C. Batra, Comp. Mechs., 3, 1 (1988).
16. A. L. Wingrove, Metall. Trans. 4, 1829 (1973).
17. Pei-Rong Lin and R. C. Batra, Int. J. Engr. Sci., 27 (1989) (to appear).
18. R. C. Batra and T. Gobinath, Int. J. Engr. Sci., 26, 741 (1988).

19. R. C. Batra and Pei-Rong Lin, Int. J. Impact Engr., 8 (1989) (to appear).

20. R. C. Batra, Int. J. Plasticity, 3, 75 (1987).

21. R. C. Batra, J. Appl. Mechs., 55, 229 (1988).

22. R. C. Batra and C. H. Kim, Int. J. Plasticity, 5 (1989) (to appear).

APPENDIX

A copy of the following papers is included in the appendix.

1. Steady State Penetration of Viscoplastic Targets.

2. Steady State Penetration of a Rigid Perfectly Plastic Rod Striking a Rigid Cavity.

3. Steady State Penetration of Compressible Rigid Perfectly Plastic Targets.

4. Effect of Nose Shape and Strain-Hardening on Steady State Deformations of Viscoplastic Targets.

5. Steady State Penetration of Thermoviscoplastic Targets.

6. The Initiation and Growth of and the Interaction Among, Adiabatic Shear Bands in Simple and Dipolar Materials.

7. Effect of Material Parameters on the Initiation and Growth of Adiabatic Shear Bands.

8. Effect of Multiple Initial Imperfections on the Initiation and Growth of Adiabatic Shear Bands in Nonpolar and Dipolar Materials.

9. Effect of Nominal Strain-Rate on the Initiation and Growth of Adiabatic Shear Bands in Steels.

Int. J. Engng Sci. Vol. 25, No. 9, pp. 1131–1141, 1987
Printed in Great Britain All rights reserved

0020-7225/87 $3.00 + 0.00
Copyright © 1987 Pergamon Journals Ltd

STEADY-STATE PENETRATION OF VISCOPLASTIC TARGETS

R. C. BATRA

Department of Engineering Mechanics, University of Missouri-Rolla, Rolla, MO 65401-0249, U.S.A.

Abstract The problem of steady-state penetration by a semi-infinite, rigid cylindrical penetrator with an ellipsoidal nose into an infinite, rigid-viscoplastic target has been studied. The target material is assumed to obey a generalized form of Von Mises yield criterion to account for the strain-rate dependence. Contact between target and penetrator is assumed to be smooth. Computed results show that the deformation field adjacent to the nose of the penetrator is significantly different in the ellipsoidal case from what it is when the nose is hemispherical. Results presented graphically include the dependence of the axial resisting force on penetrator speed, the ratio of the major to minor axes of its ellipsoidal nose, and the strain-rate hardening parameter of the target. Also depicted are the normal pressure over the penetrator nose and the velocity field in different parts of the target.

INTRODUCTION

In simple theories of penetration, the material properties of target and penetrator are often represented only by constant characteristic stresses, as for example in Tate [1]. Although this approach leads to results that are qualitatively correct, it can be difficult to use quantitatively. Some of the problems have to do with actual deformations in target and penetrator including lateral motion, and others are associated with the fact that the plastic flow stress is determined only by the deviatoric components of stress whereas the spherical or pressure component, which may be quite large ahead of the penetrator and contributes significantly to the retardation of the penetrator, is unrelated to flow stress (e.g. see Wright [2]). In developing an engineering model for penetration and perforation, Ravid and Bodner [3] assumed simple kinematics for the flow around the penetrator and then adjusted the unknown parameters by utilizing an upper bound theorem of plasticity modified to include dynamic effects.

In [4], Batra and Wright have presented a detailed numerical solution to the following idealized penetration problem. It was assumed that

(1) the rod is semi-infinite in length and that the target is infinite with a semi-infinite hole,
(2) the rate of penetration and all flow fields are steady as seen from the nose of the penetrator,
(3) no shear stress can be transmitted across the target–penetrator interface,
(4) the deforming material was taken to be rigid–perfectly plastic.

They studied the problem of the deforming target and a rigid penetrator having a circular cylindrical body and a hemispherical nose.

Batra and Wright's calculations revealed that strain rates in the target material that is ahead of the penetrator are of the order of 10^5 sec^{-1}. Since many materials used in such applications have strain-rate sensitive properties, we extend herein the previous work to viscoplastic materials. Also, the penetrator nose is taken to be ellipsoidal. As in the previous work [4], the objective here is to study the idealized penetration problem in detail and possibly shed some light on the aforementioned factors. The problem studied herein simulates approximately the following situation: the penetrator is in the intermediate stages of penetration so that the active target–penetrator interface is at least one or two penetrator diameters away from either target face, and the remaining penetrator is still much longer than several diameters and is still traveling at a speed close to its striking velocity. For this case the first two assumptions stated in the second paragraph above are quite reasonable and are also made in this work. It should be emphasized that we have not incorporated any fracture or failure criterion in our work. Thus the material is presumed to undergo unlimited plastic deformations.

FORMULATION OF THE PROBLEM

We presume that the deformations of the target appear to be independent of time to an observer situated on the penetrator nose and moving with it at a uniform velocity $v_0\mathbf{e}$, $\mathbf{e}$ being a unit vector along the direction of motion of the rigid penetrator. We use a cylindrical co-ordinate system attached to the center of the penetrator nose, with z-axis pointing into the target.

Equations governing the target deformations are:

$$\operatorname{div}\mathbf{v} = 0, \tag{1}$$

$$\rho(\mathbf{v}\cdot\operatorname{grad})\mathbf{v} = \operatorname{div}\boldsymbol{\sigma}. \tag{2}$$

Here $\mathbf{v}$ is the velocity of a target particle as seen by an observer situated on the penetrator, ρ is the mass density and $\boldsymbol{\sigma}$ is the Cauchy stress tensor. Equation (1) implies that the deformations of the target are isochoric, and eqn (2) expresses the balance of linear momentum. We neglect the elastic deformations of the target and assume that its material obeys the following constitutive relation for $\boldsymbol{\sigma}$:

$$\boldsymbol{\sigma} = -p\mathbf{1} + 2\mu(I)\mathbf{D}, \qquad I \neq 0, \tag{3}$$

$$2\mu(I) = \sigma_0(1 + bI)^m \sqrt{3}I, \tag{4}$$

$$\mathbf{D} = [\operatorname{grad}\mathbf{v} + (\operatorname{grad}\mathbf{v})^T]/2, \tag{5}$$

$$I^2 = \tfrac{1}{2}\operatorname{tr}\mathbf{D}^2. \tag{6}$$

In these equations, p is the hydrostatic pressure that is not determined by the deformation history of the target, $\mathbf{D}$ is the stretching tensor, σ_0 is the yield stress in simple tension or compression, parameters b and m describe the strain-rate hardening of the material, and $\operatorname{tr}(\mathbf{D}^2)$ equals the sum of the diagonal terms of the square matrix $\mathbf{D}^2$. Equation (3) can also be viewed as a constitutive relation for an incompressible viscous fluid with viscosity coefficient equal to $\sigma_0(1 + bI)^m/(2\sqrt{3}I)$. Implicit in eqn (3) is the assumption that the Von Mises yield surface is given by

$$\operatorname{tr}(\mathbf{s}^2) = \tfrac{2}{3}\sigma_0^2(1 + bI)^{2m}, \tag{7}$$

$$\mathbf{s} = \boldsymbol{\sigma} + p\mathbf{1}. \tag{8}$$

The tensor $\mathbf{s}$ is the deviatoric stress tensor.

Ravid and Bodner [3] have used a constitutive relation similar to eqn (3) and assumed that

$$2\mu(I) = \sigma_0(1 + C\log_{10}(2I\sqrt{3}))/\sqrt{3}I, \tag{9}$$

where C is a material constant and is taken to be zero for strain rates lower than unity. The constitutive relation for a Bingham solid [5] results by taking $m = 1$ and interpreting b properly. Zienkiewicz *et al.* [6] took

$$2\mu(I) = [\sigma_0 + (2I\gamma\sqrt{3})^{1/n}]/\sqrt{3}I \tag{10}$$

and asserted that it corresponds to Perzyna's viscoplastic model. In eqn (10) γ and n are temperature-dependent material constants. Our choice [eqns (3, 4)] was motivated by the desire to generalize the power law model used by Burns [7] and Shawki *et al.* [8] so that it is also valid for quasistatic tests. This generalized constitutive model that also includes thermal softening and strain-hardening has been used by Wright and Batra [9], and Batra

[10] to study adiabatic shear bands. For the simple shearing stress state, a curve fit to Costin *et al.*'s [11] experimental data gives $b = 10^4$ and $m = 0.025$ for a hard steel.

Equation (1) and equations obtained by substitution of eqns (3)–(5) into eqn (2) are the field equations which together with suitable boundary conditions are to be solved for p and $\mathbf{v}$. Before stating the boundary conditions, we non-dimensionalize the variables as follows:

$$\bar{\boldsymbol{\sigma}} = \boldsymbol{\sigma}/\sigma_0, \qquad \bar{\mathbf{s}} = \mathbf{s}/\sigma_0, \qquad \bar{p} = p/\sigma_0,$$

$$\bar{r} = r/r_0, \qquad \bar{z} = z/r_0, \qquad \bar{\mathbf{v}} = \mathbf{v}/v_0, \qquad \bar{b} = bv_0/r_0. \tag{11}$$

Here (r, z) denote the co-ordinates of a point with respect to the cylindrical co-ordinate system chosen, and r_0 is the radius of the cylindrical body of the penetrator. The field equations written in terms of the non-dimensional variables are:

$$\operatorname{div} \mathbf{v} = 0 \tag{12}$$

$$-\operatorname{grad} p + \operatorname{div}\{\mu[(\operatorname{grad}\mathbf{v} + (\operatorname{grad}\mathbf{v})^T]\} = \alpha(\mathbf{v}\cdot\operatorname{grad})\mathbf{v}, \tag{13}$$

where

$$\mu(I) = (1 + bI)^m 2\sqrt{3}I, \tag{14}$$

and

$$\alpha = \rho v_0^2/\sigma_0 \tag{15}$$

is a non-dimensional number. In writing eqns (12)–(14), we have dropped the superimposed bars and have used grad and div to denote the gradient and divergence operators in non-dimensional co-ordinates.

For the boundary condition on the penetrator–target interface, we assume that

$$\mathbf{t}\cdot(\boldsymbol{\sigma}\mathbf{n}) = 0, \tag{16}$$

$$\mathbf{v}\cdot\mathbf{n} = 0, \tag{17}$$

where $\mathbf{n}$ and $\mathbf{t}$ are, respectively, a unit normal and a unit tangent vector on the interface. The boundary condition (16) represents smooth contact between the penetrator and target. This appears reaonable since a thin layer of material at the interface either melts or is severely degraded by adiabatic shear. The boundary condition (17) represents no interpenetration of the target material into the penetrator and vice versa. At points far away from the penetrator we require that

$$|\mathbf{v} + \mathbf{e}| \to 0 \quad \text{as} \quad (r^2 + z^2)^{1/2} \to \infty, \qquad z > -\infty, \tag{18}$$

$$|\boldsymbol{\sigma}\mathbf{n}| \to 0 \quad \text{as} \quad z \to -\infty, \qquad r \geq r_0, \tag{19}$$

where $\mathbf{e}$ is a unit vector along the positive z-axis, as before. That is, the target material ahead of the penetrator nose and far away from it appears to approach the penetrator with a uniform velocity and the one behind the nose but very far from it is virtually traction free.

Note that the field eqns (13) are nonlinear in $\mathbf{v}$. A solution of eqns (12) and (13) under the boundary conditions (16)–(19), if there exists one, will depend upon the rate at which quantities in (18) and (19) decay to zero. Even for the prescribed rate of decay, the solution

may not be unique. We will gloss over these rather difficult questions and seek an approximate solution of these equations numerically. The hope is that the numerical solution is meaningful for the physical problem at hand.

FINITE ELEMENT FORMULATION OF THE PROBLEM

We replace the infinite target region by the bounded region R shown in Fig. 1 and the boundary conditions (18) and (19) by

$$\begin{aligned} &\sigma_{zz} = 0, \quad v_r = 0 \qquad \text{on the surface AB,} \\ &\sigma_{rz} = 0, \quad v_r = 0 \qquad \text{on the axis of symmetry DE,} \\ &v_r = 0, \quad v_z = -1.0 \qquad \text{on the bounding surface EFA.} \end{aligned} \tag{20}$$

That the region considered is adequate is justified by the computed results presented below which show that noticeable deformations of the target occur only in the region surrounding the penetrator and at target particles whose distance form the penetrator is at most $2r_0$.

Referring the reader to [12] for details, we simply note that a weak formulation of the problem defined by eqns (12), (13), (16), (17) and (20) is that equations

$$\int_R \psi(\operatorname{div} \mathbf{v})\, dv = 0, \tag{21}$$

$$\int_R p(\operatorname{div} \boldsymbol{\phi})\, dv - \int_R \mu(I)\{\mathbf{D}:[\operatorname{grad}\boldsymbol{\phi} + \operatorname{grad}\boldsymbol{\phi})^T]\}\, dv = \alpha \int_R [(\mathbf{v}\cdot\operatorname{grad})\mathbf{v}]\cdot\boldsymbol{\phi}\, dv \tag{22}$$

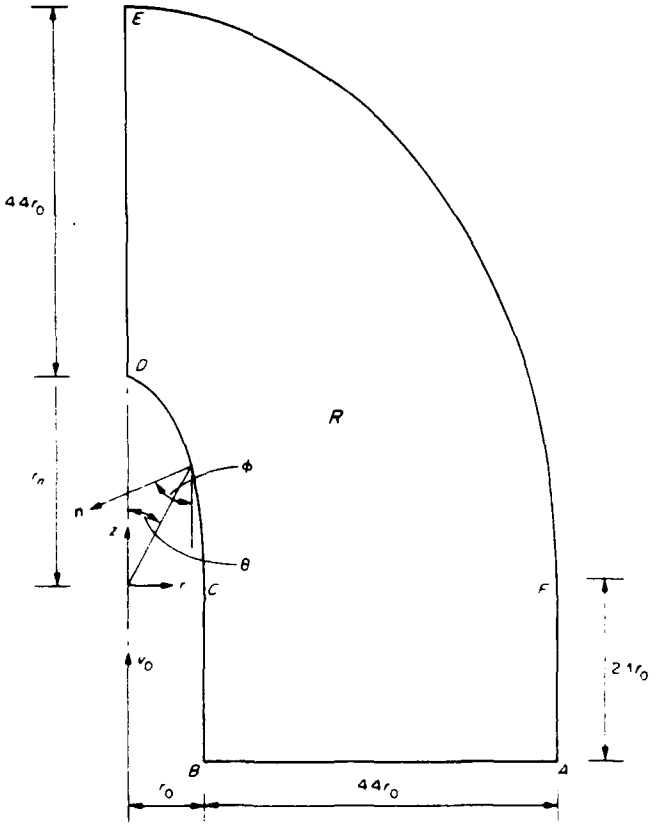

Fig. 1. The region modeled.

hold for every smooth functions ψ and $\boldsymbol{\phi}$ defined on R such that $\phi_r = 0$ on AB and DE; $\boldsymbol{\phi} = \mathbf{0}$ on EFA and $\boldsymbol{\phi} \cdot \mathbf{n} = 0$ on the target–penetrator interface BCD. Since eqns (21) and (22) are nonlinear in $\mathbf{v}$, the following iterative technique has been employed:

$$\int_R \psi(\operatorname{div} \mathbf{v}^i)\,dv = 0, \tag{23}$$

$$\int_R p^i(\operatorname{div} \boldsymbol{\phi})\,dv - \int_R \mu(I^{i-1})\{\mathbf{D}^i : [\operatorname{grad} \boldsymbol{\phi} + (\operatorname{grad} \boldsymbol{\phi})^T]\}\,dv = \alpha \int_R [(\mathbf{v}^{i-1} \cdot \operatorname{grad})\mathbf{v}^i] \cdot \boldsymbol{\phi}\,dv, \tag{24}$$

where i is the iteration number. The solution was taken to have converged, if at each nodal point,

$$|\mathbf{v}^i - \mathbf{v}^{i-1}| \leq 0.01\,|\mathbf{v}^{i-1}|,$$

where

$$|\mathbf{v}|^2 = v_r^2 + v_z^2.$$

COMPUTATION AND DISCUSSION OF RESULTS

The finite element code developed earlier [4] to solve the problem when the target material is modeled as rigid–perfectly plastic and the penetrator nose is hemispherical has been modified to solve the present problem. It employs six-noded isoparametric triangular elements with v_r and v_z approximated by quadratic functions over an element and p by a linear function defined in terms of its values at the vertices of the triangular element. The accuracy of the code was established by solving a simple problem for an incompressible Navier–Stokes fluid.

The computational procedure was started by taking $\mathbf{v}^0 = \mathbf{0}$, $\mu(I^0) = 10^4$. It took 19 iterations for the solution to converge when $\alpha = 2$ and the nose is hemispherical. The number of iterations required to obtain the solution decreased with an increase in the ratio r_n/r_0 when $\alpha = 2$. However, for $r_n/r_0 = 1$, the number of iterations increased with α, but for $r_n/r_0 = 2$ it decreased with an increase in α. Numerical experiments with different grids were conducted first by increasing the number of elements used and then by varying their size but keeping the number of elements used constant. The grid with 8 rows of elements in the axial direction, 8 uniformly spaced rows of elements in the circumferential direction and 8 rows behind the plane $z = 0$, was found to be optimum in the sense that the change in the normal stress at the penetrator nose tip was less than 0.1% with further refinements of the grid. The grid used had a pattern similar to that employed in [4]. The dividing surfaces between elements intersected the z-axis at points distant 0.475, 0.969, 1.483, 2.017, 2.573, 3.151, 3.752, 4.377 from the nose tip. The z-co-ordinate of the horizontal surfaces between rows of elements behind the $z = 0$ plane were -0.156, -0.335, -0.540, -0.773, -1.041, -1.347, -1.697, -2.09. For $\alpha = 2.0$, $r_n/r_0 = 2.0$, $m = 0.0$, and $h = 0.0$, the total axial force, defined below by eqn (29), obtained by using 4, 6, 7, 12 and 13 quadrature points was computed to be 2.6117, 2.6479, 2.6524, 2.6714 and 2.6720 respectively. The results presented below have been obtained by using 4 quadrature points.

Figure 2 depicts the velocity of the target particles for $\alpha = 4$ and $r_n/r_0 = 2.0$ as seen by an observer sitting on the penetrator nose. It is apparent that significant deformations of the target occur at points within $2r_0$ of the penetrator boundaries. The velocity fields for other cases studied have a similar pattern. At target points that lie to the rear of the center of the penetrator nose, the flow quickly becomes parallel to the axis of the penetrator. In Fig. 3 is shown the non-dimensional normal stress on the penetrator nose for different choices of various parameters. Values of parameters for various curves in this and subsequent figures, unless specified otherwise, are identified in Table 1. The change in nose shape from hemispherical to ellipsoidal reverses the curvature of the normal stress vs θ

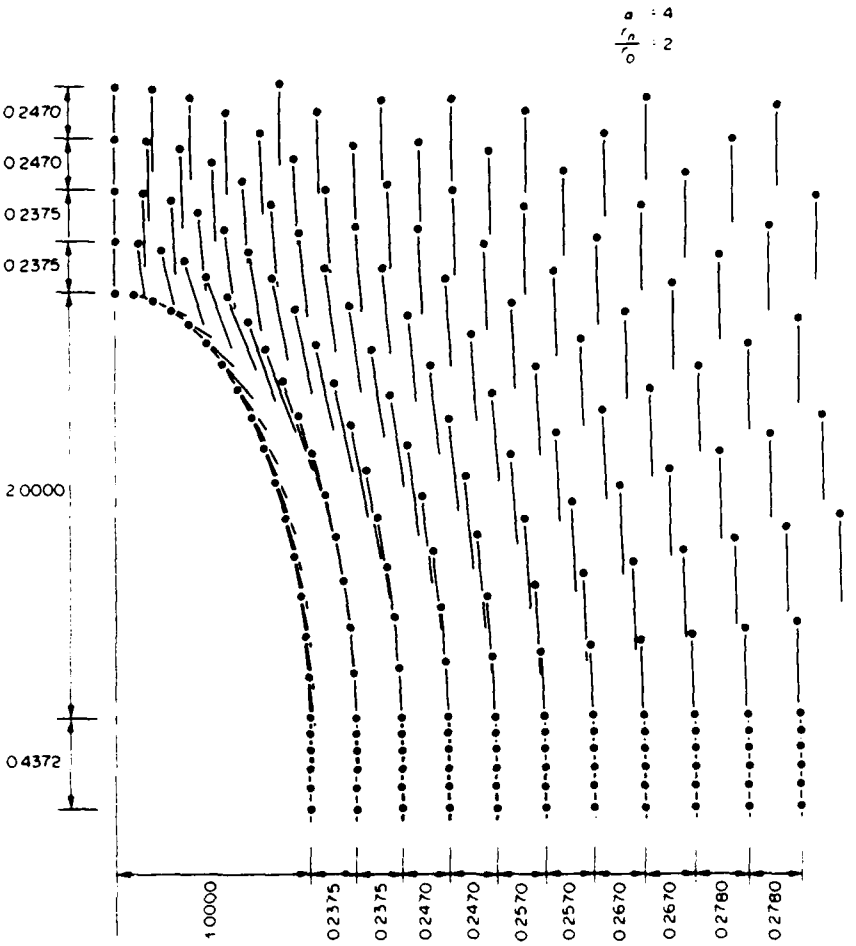

Fig. 2. Typical velocity field.

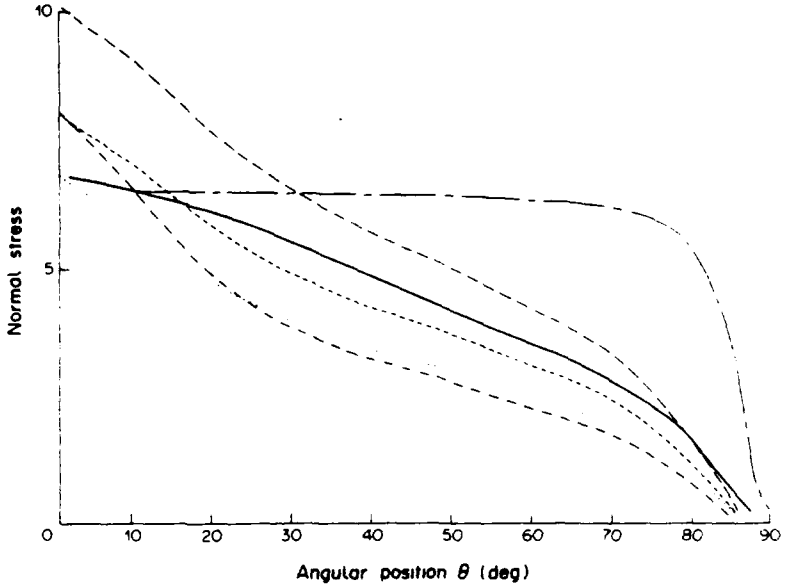

Fig. 3. Normal stress distribution on the penetrator nose

Table 1. Legend for figures

Curve type	Parameter values
– – – – – –	$\frac{r_n}{r_0} = 2.0,\ b = 10^6,\ m = 0.03,\ \alpha = 2.0$
- - - - - -	$\frac{r_n}{r_0} = 2.0,\ b = 10^4,\ m = 0.03,\ \alpha = 2.0$
.....	$\frac{r_n}{r_0} = 2.0,\ b = 0,\ m = 0,\ \alpha = 2.0$
– – –	$\frac{r_n}{r_0} = 2.0,\ b = 0,\ m = 0,\ \alpha = 4.0$
.....	$\frac{r_n}{r_0} = 1.0,\ b = 0,\ m = 0,\ \alpha = 2.0$
– · – ·	$\frac{r_n}{r_0} = 0.2,\ b = 0,\ m = 0,\ \alpha = 2.0$

curve from convex downwards to concave downwards. This change was observed even for $r_n/r_0 = 1.1$. For $\alpha = 2$, the normal stress at the nose tip was essentially unchanged for $0.2 \leqslant r_n/r_0 \leqslant 2.4$. For $r_n/r_0 = 0.2$, the nose shape is essentially flat and, as expected, the normal stress on it stays uniform and drops off rapidly near the periphery. The increase in α, m or b increases the normal stress on the penetrator nose.

The non-dimensional axial resisting force experienced by the penetrator as various

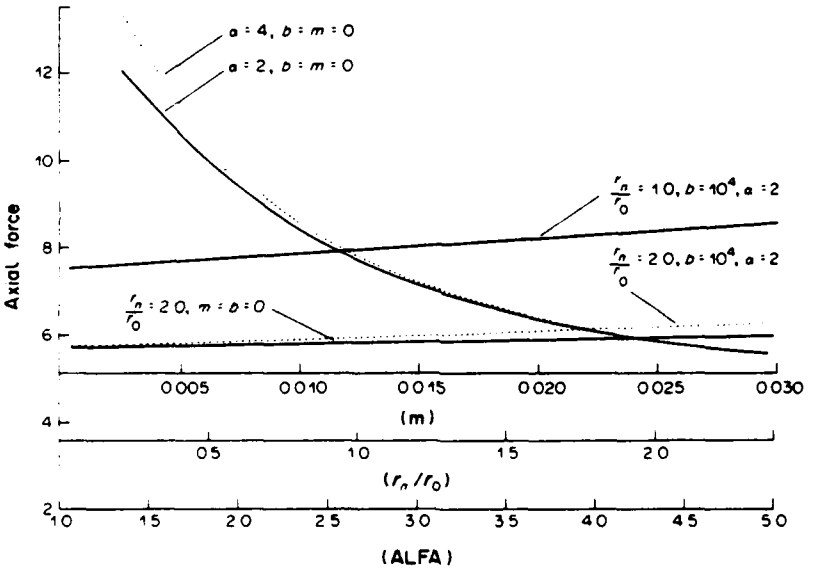

Fig. 4. Dependence of axial force on various factors.

parameters are changed is plotted in Fig. 4. Equations obtained by fitting curves to the computed data are:

$$F = 2.58(1 + 0.00738\alpha - 0.000569\alpha^2), \quad 1 \leqslant \alpha \leqslant 5, \quad \frac{r_n}{r_0} = 2.0, \quad b = m = 0, \tag{25}$$

$$F = 2.611(1 + 6.761m + 20.465m^2), \quad 0 \leqslant m \leqslant 0.03, \quad \frac{r_n}{r_0} = 2.0, \quad b = 10^4, \quad \alpha = 2.0, \tag{26}$$

$$F = 4.456(1 + 7.28m + 23.478m^2), \quad 0 \leqslant m \leqslant 0.03, \quad \frac{r_n}{r_0} = 1.0, \quad b = 10^4, \quad \alpha = 2.0, \tag{27}$$

$$F = 13.041\left[1.0 - 1.3086\frac{r_n}{r_0} + 0.9504\left(\frac{r_n}{r_0}\right)^2 - 0.3432\left(\frac{r_n}{r_0}\right)^3 + 0.0477\left(\frac{r_n}{r_0}\right)^4\right],$$

$$0.2 \leqslant \frac{r_n}{r_0} \leqslant 2.4, \quad b = m = 0, \quad \alpha = 4 \tag{28}$$

$$F = 10.857\left[1.0 - 1.0455\frac{r_n}{r_0} + 0.6294\left(\frac{r_n}{r_0}\right)^2 - 0.1975\left(\frac{r_n}{r_0}\right)^3 + 0.0246\left(\frac{r_n}{r_0}\right)^4\right].$$

$$0.2 \leqslant \frac{r_n}{r_0} \leqslant 2.4, \quad h = m = 0, \quad \alpha = 2,$$

where

$$F = 2\int_0^{\pi/2} (\mathbf{n}\cdot\boldsymbol{\sigma}\mathbf{n})\sin\theta\cos\phi\left[\sin^2\theta + \left(\frac{r_n}{r_0}\right)^2\cos^2\theta\right]^{1/2} d\theta, \tag{29}$$

ϕ is the angle which the unit normal to the nose makes with the penetrator axis as shown in Fig. 1. The corresponding axial force in physical units is given by $F(\pi r_0^2\sigma_0)$. It is clear from these results that changing the nose shape from hemispherical to ellipsoidal with $r_n/r_0 = 2.0$ reduces the axial resisting force to one-half of its value. For a fixed r_n/r_0 and m, the axial force depends rather weakly upon α. This weak dependence of F upon α is perhaps one reason why the choice of constant target resistance in simple theory of Tate [1] gives good qualitative results. Even though the coefficient of m^2 in eqns (25) and (26) is nearly 3 times that of m, the dependence of the axial force F upon the strain-rate hardening coefficient m is essentially linear. It is so because the values of m for typical steels are much smaller than one. This linear dependence of F upon m becomes transparent from the plots of Fig. 4.

Computed results indicate that for $1 \leqslant \alpha \leqslant 5$, $r_n/r_0 = 2.0$, $h = m = 0$, the hydrostatic pressure at the nose tip increases essentially linearly from 5.6 to 8.2 and the normal compressive stress from 6.22 to 8.84. It is apparent that the hydrostatic pressure contributes significantly to the values of σ_{rr} and σ_{zz}. Figure 5 shows that the principal stress component $-\sigma_{zz}$ along the axis in front of the penetrator falls off rapidly with the distance. The stresses at points situated more than $3r_0$ from the nose tip cannot be accurately determined since the velocity gradients there are extremely small. The values of σ_{zz} at points on the centerline which are at a distance of $3r_0$ and more from the nose tip equal essentially the hydrostatic pressure.

In Fig. 5 is also plotted the variation of the strain-rate measure I along the axial line. These nondimensional values need to be multiplied by v_0/r_0, which typically equals 10^5, to arrive at the corresponding dimensional effective strain-rate measure I. Thus strain-rates of the order of $2 \times 10^5\ \text{sec}^{-1}$ occur at points in the vicinity of the penetrator nose. On the axial line, peak values of I are higher near the nose tip for $r_n/r_0 = 2.0$ as compared with those for lower values of r_n/r_0. However, near the periphery of the penetrator nose and its cylindrical body, the strain-rate measure I for the blunt nose increases by an order of magnitude whereas that for the ellipsoidal and hemispherical nose, it drops by a factor of 10. This is shown in Fig. 6 wherein is also plotted the nondimensional velocity, tangential to the penetrator nose, for different values of various parameters. Again the nose shape is the major influencing factor. However, v_z at points on the centerline ahead of the penetrator nose is not affected that much by the nose shape except for $r_n/r_0 = 0.2$. The decay rate of $|v_z + \mathbf{e}|$ for $1 \leqslant \frac{r_n}{r_0} \leqslant 2.4$ is nearly constant but is appreciably less for $r_n/r_0 = 0.2$. The nose shape does change rather noticeably the relative z-velocity of points on the lines $z = 0$ and $z = 2.09$. This follows from the results depicted in Figs 7 and 8 which also show that more of the target material at the sides of the penetrator deforms for a penetrator with an ellipsoidal nose, even though it is not true ahead of the penetrator, as noted earlier. Two of the curves in these figures essentially overlap.

We note that the target material within some distance inside the boundary EFA does not deform at all and the deformations are essentially independent of z near the boundary

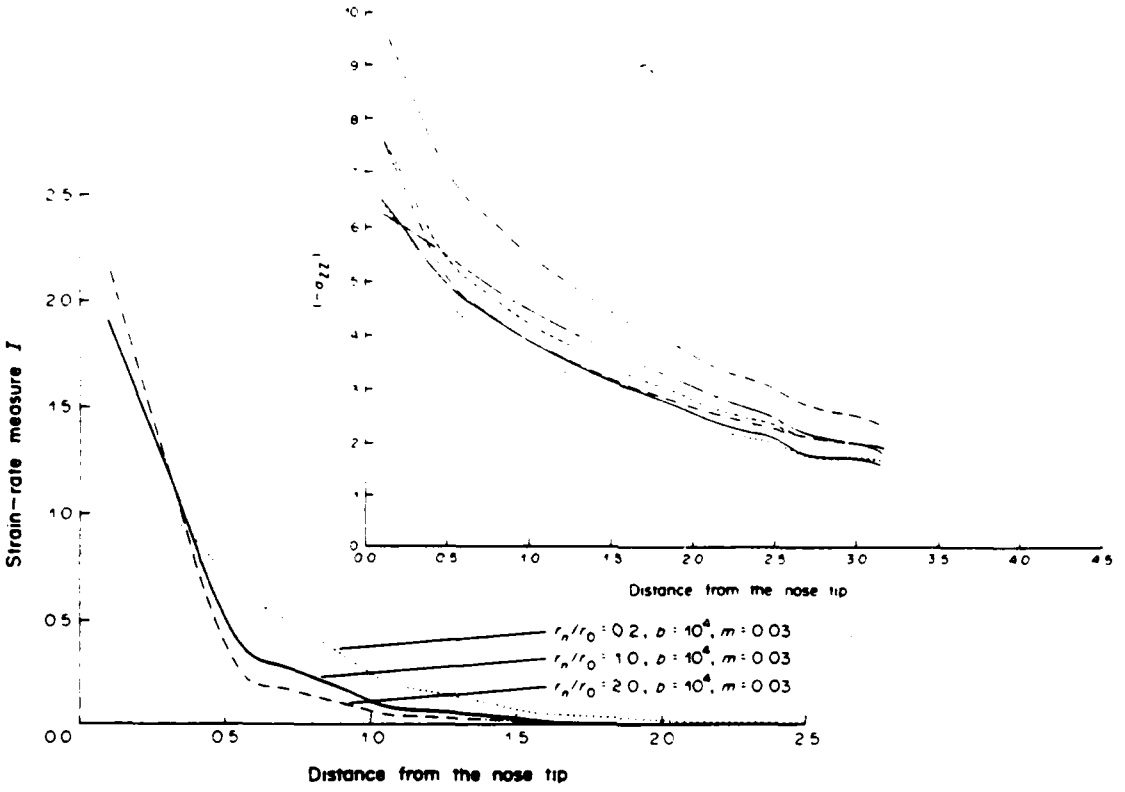

Fig. 5 Variation of $-\sigma_{zz}$ and strain-rate measure I on the centerline with distance from the nose tip

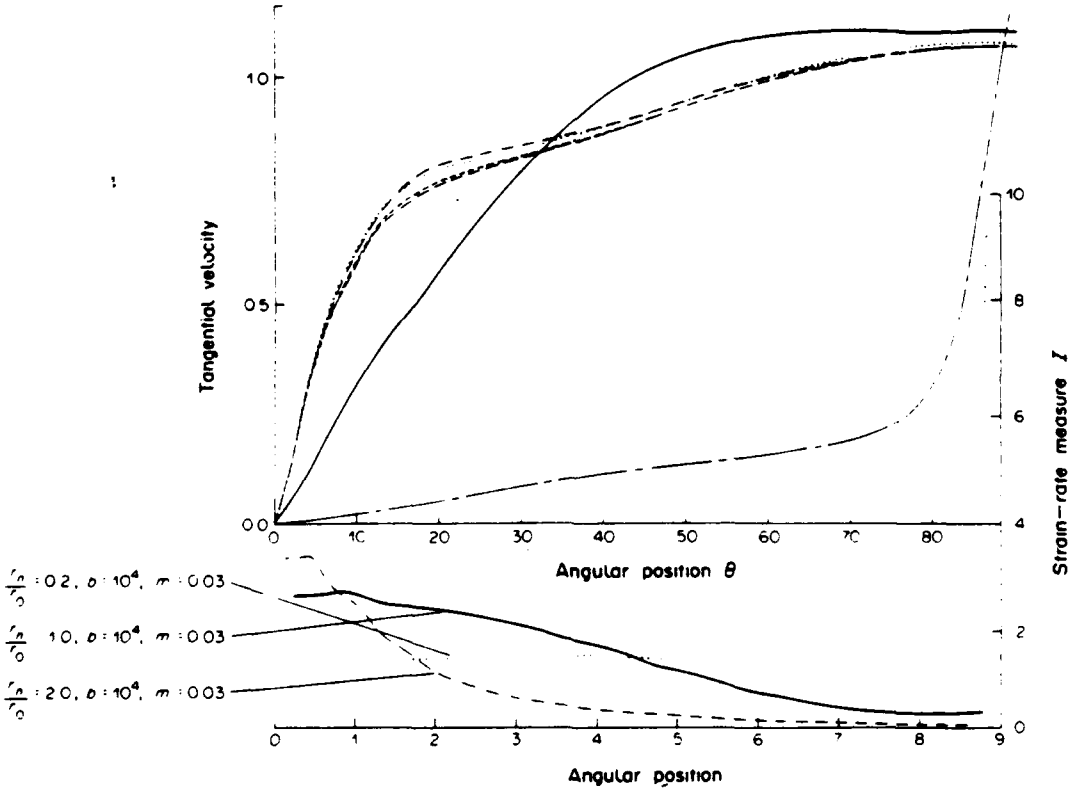

Fig. 6 Variation of tangential velocity and strain-rate measure on the penetrator nose

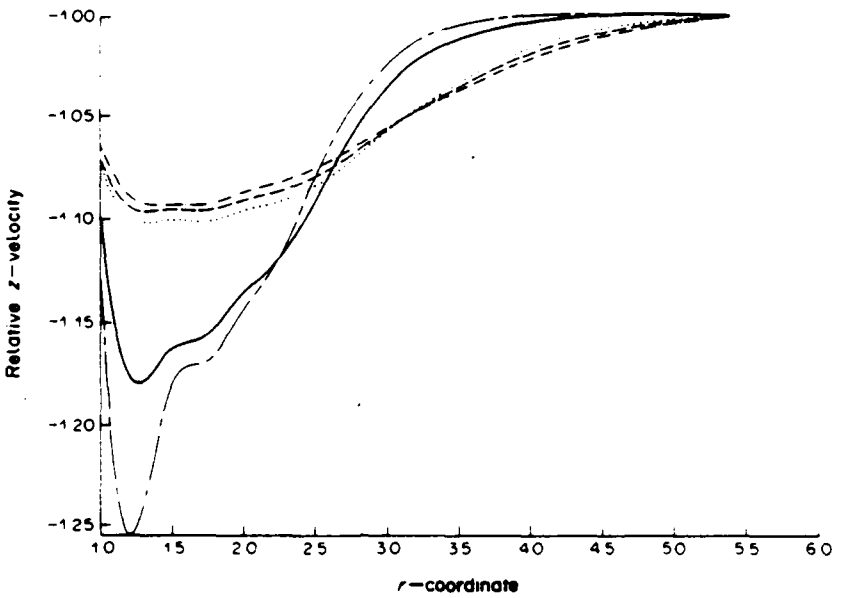

Fig. 7. Variation of relative z-velocity with radial co-ordinate r on the line $z = 0$

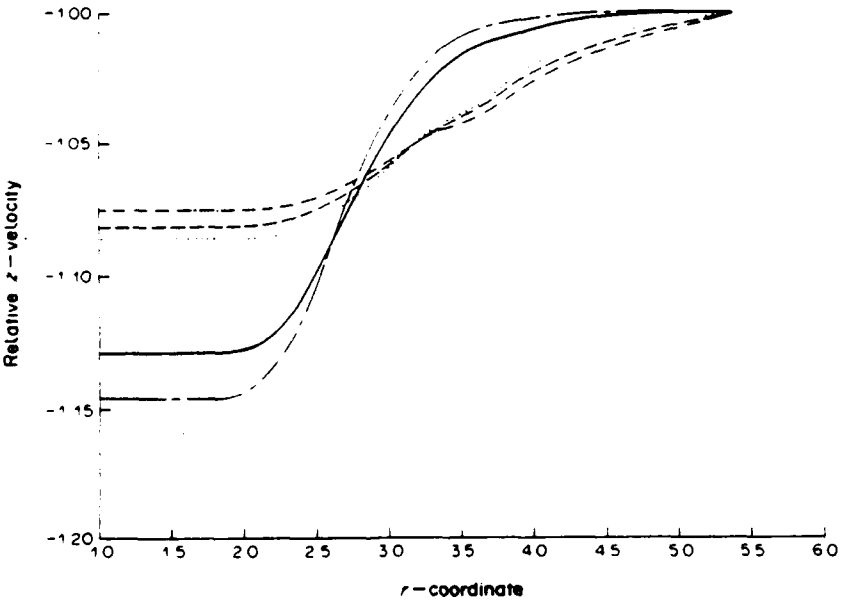

Fig. 8. Variation of relative z-velocity with radial co-ordinate r on the line $z = -2.09$

AB. It is therefore reasonable to conclude that the target region chosen for computation is sufficient to obtain a good description of the deformations in the vicinity of the penetrator nose.

CONCLUSIONS

For the range of values of r_n/r_0, α and m studied, the ratio r_n/r_0 of the radius of the nose to that of the cylindrical body of the penetrator has the most effect on the axial resisting force experienced by the penetrator. The retardation force depends rather weakly on α and m. In all cases, significant target deformations occur only within $2r_0$ of the penetrator. Whereas for $r_n/r_0 = 1.0$, the target material adjacent to the sides of the penetrator appears to extrude rearwards in a uniform block that is separated from the bulk of the target material by a narrow region with a sharp velocity gradient, such is not

the case for $r_n/r_0 = 2.0$. In the latter case there is no noticeable region of steep velocity gradients.

For $\alpha = 5$ and $r_n/r_0 = 2.0$ the target material seemed to separate from the sides of the penetrator nose. This provides a limiting value for the validity of our calculations since flow separation has not been built into our model. Maximum normal stress and the maximum hydrostatic pressure occur at the nose tip, and fall off rapidly away from that point. These peak values depend significantly upon α.

We hope that results presented here will prove useful in devising or checking the results from simpler engineering theories of penetration.

Acknowledgements This work was supported by the U.S. Army Research Office contract DAAG29-85-K-0238 to the University of Missouri-Rolla. I thank Pei-Rong Lin for his help in plotting Fig. 2.

REFERENCES

[1] A. TATE, *J. Mech. Phys. Solids* **15**, 387 (1967); *ibid.* **17**, 141 (1969).
[2] T. W. WRIGHT, A survey of penetration mechanics for long rods. *Lecture Notes in Engineering, Vol. 3, Computational Aspects of Penetration Mechanics* (Edited by J. Chandra and J. Flaherty). Springer-Verlag, New York (1983).
[3] M. RAVID and S. R. BODNER, *Int. J. Engng Sci.* **21**, 577 (1983).
[4] R. C. BATRA and T. W. WRIGHT, *Int. J. Engng Sci.* **24**, 41 (1986).
[5] N. CRISTESCU and I. SULICIU, *Viscoplasticity*. Martinus Nijhoff, The Hague (1982).
[6] O. C. ZIENKIEWICZ, E. ONATE and J. C. HEINRICH, *Int. J. numer. Meths Engng* **17**, 1497 (1981).
[7] T. J. BURNS, Sandia Rep. SAND83-1907, Sandia National Laboratories, Albuquerque, NM (1983).
[8] T. G. SHAWKI, R. J. CLIFTON and G. MAJDA, Brown University Rep. ARO DAAG 29-81-K-0121.3, Providence, RI (1983).
[9] T. W. WRIGHT and R. C. BATRA, *Proc. IUTAM Symp. Macro- and Micro-Mechanics of High Velocity Deformation and Fracture*. Springer-Verlag, New York-Berlin (1986).
[10] R. C. BATRA, *Int. J. Plast.* **3**, 75 (1987).
[11] L. S. COSTIN, E. E. CRISMAN, R. H. HAWLEY and J. DUFFY, *Inst. Phys. Conf. Ser. no.* **47**, 90 (1979).
[12] E. BECKER, G. CAREY and J. T. ODEN, *Finite Element: An Introduction*, Vol. 1, Prentice-Hall, Englewood Cliffs, NJ (1981).

(*Received* 23 *December* 1986)

Int. J. Engng Sci. Vol. 26, No. 2, pp. 183–192, 1988
Printed in Great Britain

0020–7225/88 $3.00 + 0.00
Pergamon Press plc

STEADY STATE DEFORMATIONS OF A RIGID PERFECTLY PLASTIC ROD STRIKING A RIGID CAVITY

R. C. BATRA and PEI-RONG LIN

Deparment of Engineering Mechanics, University of Missouri-Rolla, Rolla, MO 65401-0249, U.S.A.

Abstract—The axisymmetric steady state deformations of an infinite cylindrical rod made of a rigid/perfectly plastic material and striking a known cavity in a rigid target are analyzed by the finite element method. The contact between the deforming rod and the target surface is assumed to be smooth. It is found that the axial force experienced by the rod depends strongly upon the square of its speed. Results computed and presented graphically include the velocity field in the deforming region, the dependence of the shape of the upset head of the striker upon its speed, and the distribution of normal tractions upon the cavity wall.

INTRODUCTION

Penetration of metal targets by projectiles is influenced by such variables as material properties, impact velocity, projectile shape, target support position, and relative dimensions of the target and the projectile. Recently, emphasis has been placed on kinetic energy penetrators, which for terminal ballistic purposes may be considered as long metal rods traveling at high speeds. Wright [1], in his survey article on long rod penetrators, ellucidated vividly some of the problems with the existing penetration models. In another extensive review article, Backman and Goldsmith [2] discussed superbly the work done in penetration mechanics until 1977. Jonas and Zukas [3] reviewed various analytical methods for the study of kinetic energy projectile-armor interaction at ordance velocities and placed particular emphasis on three-dimensional numerical simulation of perforation. Anderson and Bodner [4] have recently reviewed the status of the ballistic impact modeling. A penetration model that is not too difficult to use has been proposed by Ravid and Bodner [5]. They studied the penetration problem by presuming a kinematically admissible flow field in the target and found the unknown parameters by utilizing an upper bound theorem of plasticity modified to include dynamics effects.

In an attempt to shed some light on questions raised by Wright [1], Batra and Wright [6] recently studied an idealized penetration problem that simulates the following situation. Suppose that the penetrator is in the intermediate stages of penetration so that the active target/penetrator interface is at least one or two penetrator diameters away from either target face, and the remaining penetrator is much longer than several diameters and is still traveling at a speed close to its striking velocity. This situation has been idealized as follows. It is assumed that the rod is semi-infinite in length, the target is infinite with a semi-infinite hole, the rate of penetration and all flow fields are steady as seen from the nose of the penetrator, and that no shear stress can be transmitted across the target/penetrator interface. This last assumption is justified on the grounds that a thin layer of material at the interface either melts or is severely degraded by adiabatic shear. These idealizations make it possible to decompose the penetration problem into two parts in which either a rigid rod penetrates a deformable target or a deformable rod is upset at the bottom of a hole in a rigid target. Of course, in the combined case the contour of the hole is unknown, but if it can be chosen so that normal tractions match in the two cases along the entire boundary between penetrator and target, then the complete solution is known irrespective of the relative motion at the boundary. Even without matching the normal tractions, it would seem that valuable qualitative information about the flow field and distribution of stresses can be gained if the chosen contour is reasonably close to those that are found in experiments.

Whereas Batra and Wright [6] studied the problem of the deforming target and a rigid penetrator, we analyze herein the companion problem of a deformable, semi-infinite and cylindrical penetrator striking a known semi-infinite cavity in an infinite and rigid target. Only the axisymmetric and steady state problem in which the penetrator material is rigid/perfectly

plastic has been studied. This problem is more challenging than the one studied earlier by Batra and Wright [6] because of the presence in it of free surfaces whose shapes are not known *a priori*. We hope that the kinematic and stress fields found in this study would help in devising and/or checking results from simpler engineering theories of penetration.

FORMULATION OF THE PROBLEM

We describe the deformations of the cylindrical rod upset at the bottom of a semi-infinite cavity in an infinite rigid target with respect to a cylindrical coordinate system with origin at the center of the hole and z-axis pointing into the rod. Equations governing the steady state axisymmetric deformations of the rod are

$$\operatorname{div}\mathbf{v} = 0, \tag{1}$$

$$\operatorname{div}\boldsymbol{\sigma} = \rho\dot{\mathbf{v}}, \tag{2.1}$$

$$= \rho(\mathbf{v}\cdot\operatorname{grad})\mathbf{v}. \tag{2.2}$$

Here $\mathbf{v}$ is the velocity of a rod particle, ρ is the mass density and $\boldsymbol{\sigma}$ is the Cauchy stress tensor. Equation (1) implies that the deformations of the rod are isochoric, and eqn (2) expresses the balance of linear momentum. The operators grad and div signify the gradient and divergence operators on fields defined in the present configuration. We neglect the elastic deformations of the rod and assume that it is made of a homogeneous and isotropic material that obeys the Von-Mises yield criterion and the associated flow rule. Thus we take the following constitutive relation for $\boldsymbol{\sigma}$, e.g. see Prager and Hodge [7].

$$\boldsymbol{\sigma} = -p\mathbf{1} + \frac{\sigma_0}{\sqrt{3}\,I}\mathbf{D}, \tag{3}$$

$$\mathbf{D} = (\operatorname{grad}\mathbf{v} + (\operatorname{grad}\mathbf{v})^T)/2, \tag{4}$$

$$I^2 = \frac{1}{2}\operatorname{tr}\mathbf{D}^2. \tag{5}$$

In eqn (3) p is the hydrostatic pressure which cannot be determined from a knowledge of the deformation because of the assumption of material incompressibility, $\mathbf{1}$ is the unit matrix, σ_0 is the flow stress of the material of the rod in simple compression or tension and I is the second invariant of the strain-rate tensor $\mathbf{D}$. Equation (1) and the equation obtained by substituting eqn (3) into (2) are the field equations to be solved for $\mathbf{v}$ and p subject to a suitable set of boundary conditions. In terms of the non-dimensional variables

$$\bar{\mathbf{v}} = \mathbf{v}/v_0, \qquad \bar{\boldsymbol{\sigma}} = \boldsymbol{\sigma}/\sigma_0, \qquad \bar{p} = p/\sigma_0, \qquad \bar{r} = r/r_0, \qquad \bar{z} = z/r_0, \tag{6}$$

these field equations are

$$\operatorname{div}\mathbf{v} = 0, \tag{7}$$

$$-\operatorname{grad}p + \operatorname{div}((\operatorname{grad}\mathbf{v} + (\operatorname{grad}\mathbf{v})^T)/2\sqrt{3}\,I) = \alpha(\mathbf{v}\cdot\operatorname{grad})\mathbf{v} \tag{8}$$

where

$$\alpha = \rho v_0^2/\sigma_0 \tag{9}$$

is a non-dimensional number. In eqn (6), v_0 is the speed of the rod and r_0 its radius. In eqns (7) and (8) and hereafter the superimposed bars over the non-dimensional variables have been dropped. The operators grad and div in eqn (8) imply the gradient and divergence operators in terms of the non-dimensional coordinates. We note that there is only one non-dimensional number α that governs the steady state deformations of the rod.

For the boundary conditions on the rod/cavity interface, we assume that

$$\mathbf{t}\cdot(\boldsymbol{\sigma}\mathbf{n}) = 0, \tag{10}$$

$$\mathbf{v}\cdot\mathbf{n} = 0, \tag{11}$$

where $\mathbf{n}$ and $\mathbf{t}$ are, respectively, a unit normal and unit tangent vector on the interface. The boundary condition (10) represents smooth contact between the rod and target. This appears

reasonable since a thin layer of material at the interface either melts or is severely degraded by adiabatic shear. The boundary conditon (11) represents no interpenetration of the rod material into the target and vice versa. On the free surface of the rod,

$$\boldsymbol{\sigma}\mathbf{n} = \mathbf{0}, \tag{12}$$

$$\mathbf{v} \cdot \mathbf{n} = 0, \tag{13}$$

where $\mathbf{n}$ is a unit outward normal to the surface. The boundary condition (13) implies that the velocity of particles on the surface is tangent to the surface. Out of the boundary conditions (12) and (13) only the former is needed to specify the boundary-value problem completely provided the shape of the free surface is known. Since such is not the case, we use eqn (13) to check whether the presumed free surface is correct or not. On the rod cross-section far from the cavity bottom

$$|\mathbf{v} + \mathbf{e}_z| \to 0 \quad \text{as} \quad z \to \infty, \tag{14}$$

and on the deformed rod material at the cavity outlet

$$|\boldsymbol{\sigma}\mathbf{n}| \to 0 \quad \text{as} \quad |r^2 + z^2|^{1/2} \to \infty. \tag{15}$$

Equation (14) implies that the end of the rod far from the bottom of the cavity is moving with a uniform velocity in the negative z-direction and eqn (15) is equivalent to the statement that the surface of the deformed rod near the cavity outlet is traction free. In order to state the problem more precisely one should specify the rates at which quantities indicated in eqns (14) and (15) decay. But at the present time there is little hope of establishing an existence and uniqueness theory for the problem and, therefore, specification of rates of decay in eqns (14) and (15) is not required. Here we seek an approximate solution of the problem numerically.

FINITE ELEMENT FORMULATION OF THE PROBLEM

To solve the problem numerically we usually consider a finite region. Thus the region of the deformable rod analyzed is shown in Fig. 1 wherein is also indicated its spatial discretization. We note that since the shape of the free surface is not known *a priori* we estimate one and will subsequently check whether or not it is an appropriate one. If not, we will modify the same and keep on iterating till a prespecified criterion is met. This is elaborated upon below. The boundary conditions (10)–(12), (14) and (15) are replaced by the following:

$$\sigma_{rz} = 0, \qquad v_r = 0 \text{ on the axis of symmetry AB}, \tag{16.1}$$

$$\mathbf{v} \cdot \mathbf{n} = 0 \text{ and } \mathbf{t} \cdot (\boldsymbol{\sigma}\mathbf{n}) = 0 \text{ on the cavity surface BC}, \tag{16.2}$$

$$\boldsymbol{\sigma}\mathbf{n} = \mathbf{0} \text{ on the free surface DEF}, \tag{16.3}$$

$$v_z = -1.0, \qquad v_r = 0 \text{ on AF}, \tag{16.4}$$

$$\mathbf{v} = v_e\mathbf{n} \text{ and } \mathbf{t} \cdot (\boldsymbol{\sigma}\mathbf{n}) = 0 \text{ on the outlet surface CD}. \tag{16.5}$$

As before $\mathbf{n}$ is a unit outward normal to a surface and $\mathbf{t}$ is a unit tangent to the surface. The boundary condition (16.5) implies that the rod particles at the exit surface CD are traveling normal to the surface with a uniform speed v_e and the tangential traction on it is zero. The value of v_e is computed by equating the amount of material flowing out through CD to that flowing in through AF. We now obtain a variational statement for the boundary value problem defined by eqns (7), (8) and (16).

Let $\boldsymbol{\phi}$ be a smooth vector valued function defined on the region R, shown enclosed by ABCDEF in Fig. 1, and $\phi_r = 0$ on AB, $\boldsymbol{\phi} \cdot \mathbf{n} = 0$ on BC, $\boldsymbol{\phi} = 0$ on AF and $\boldsymbol{\phi} \cdot \mathbf{n} = 0$ on CD. Also let ψ be a bounded scalar valued function defined on R. Multiplying both sides of eqn (7) with ψ, taking the scalar product of both sides of eqn (8) with $\boldsymbol{\phi}$, integrating the resulting equations on the domain R, using the divergence theorem, the traction boundary conditions in (16) and the above stated side conditions on $\boldsymbol{\phi}$ we arrive at the following.

$$\int_R \psi(\operatorname{div} \mathbf{v})\, dV = 0, \tag{17.1}$$

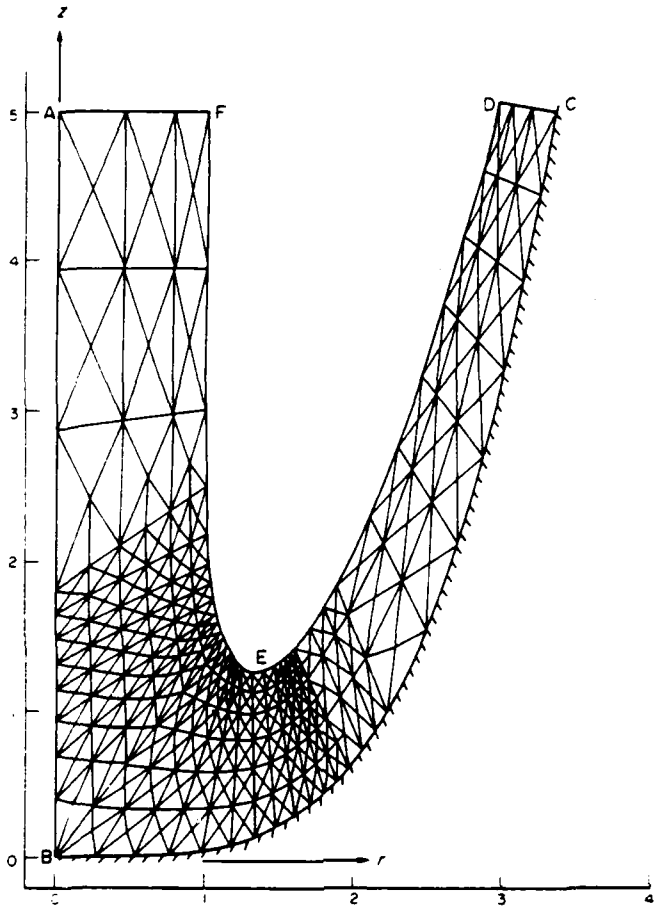

Fig. 1. The region studied and its finite element discretization.

$$\int_R p(\operatorname{div}\boldsymbol{\phi})\,dV - \int_R \frac{1}{2\sqrt{3}\,I}\mathbf{D} : (\operatorname{grad}\boldsymbol{\phi} + (\operatorname{grad}\boldsymbol{\phi})^T)\,dV = \alpha\int_R \{(\mathbf{v}\cdot\operatorname{grad})\mathbf{v}\}\cdot\boldsymbol{\phi}\,dV. \quad (17.2)$$

Here a single dot implies the scalar product between two vectors and the symbol : stands for the scalar product between two second order symmetric tensors. Thus a weak formulation of the boundary-value problem given by eqns (7), (8) and (16) is to find p and $\mathbf{v}$ defined on R such that eqns (17) holds for every ψ and $\boldsymbol{\phi}$, ψ and grad $\boldsymbol{\phi}$ are square integrable over R, $\boldsymbol{\phi}$ satisfies the homogeneous essential boundary conditions stated above and $\mathbf{v}$ satisfies the essential boundary conditions outlined in eqns (16).

We refer the reader to Becker *et al.* [8] for details of obtaining a finite element solution of eqns (17). Suffice it to say that eqns (17) are solved by using the following iterative scheme.

$$\int_R \psi(\operatorname{div}\mathbf{v}^m)\,dV = 0, \quad (18.1)$$

$$\int_R p^m(\operatorname{div}\boldsymbol{\phi})\,dV - \int_R \frac{1}{2\sqrt{3}\,I^{m-1}}\mathbf{D}^m : (\operatorname{grad}\boldsymbol{\phi} + (\operatorname{grad}\boldsymbol{\phi})^T)\,dV = \alpha\int_R \{(\mathbf{v}^{m-1}\cdot\operatorname{grad})\mathbf{v}^m\}\cdot\boldsymbol{\phi}\,dV \quad (18.2)$$

Here m is the interation number. Note that the hydrostatic pressure p appears linearly and its previous values are not needed. The initial velocity field is taken to be zero for small values of α. If the solution is known for some α, it is taken as the initial solution when solving the problem for the next higher value of α. The iteration process in (18) is stopped if, at each nodal point,

$$\|\mathbf{v}^m - \mathbf{v}^{m-1}\| \le 0.01\,\|\mathbf{v}^{m-1}\| \quad (19)$$

where $\|\mathbf{v}\|^2 = (v_r^2 + v_z^2)$. When the velocity field corresponding to $(\alpha - 1)$ was taken as the initial estimate for the solution to be computed for an assigned value of α, it took nearly 10 iterations for the convergence criterion (19) to be satisfied.

TREATMENT OF THE FREE SURFACE

In the preceding finite element formulation of the problem the shape of the free surface DEF was presumed to be given. Since it is not known *a priori* we presume one, solve the problem and then see if the condition (13) is satisfied on it or not. Improving upon the presumed shape of the free surface DEF if (13) is not satisfied required a considerable effort. We note that problems in which the shape of the free surface is to be determined as a part of the solution of the problem have been solved by Zienkiewicz *et al.*, [9], Oden and Lin [10], and Batra *et al.* [11]. For us the following technique proved quite effective.

Starting from the point F we found the parabolic curve passing through F and the next two nodes downstream from it. We then found the tangent to the curve and a unit normal $\mathbf{n}$ at the middle node. We evaluated the magnitude of the error

$$e \equiv \mathbf{v} \cdot \mathbf{n} / \|\mathbf{v}\| \tag{20}$$

at the middle node and repeated this procedure for all of the nodes. Note that the node F is fixed and the last node D on the free surface was assumed to be on the straight line passing through the two nodes immediately preceding to it on the free surface DEF. That is, the curvature of DE near the point D was presumed to be zero. Points where the magnitude of the error e was not smaller than a preassigned small number were moved along $\mathbf{n}$ or $-\mathbf{n}$ according as e was positive or negative and the distance moved was proportional to the magnitude of e. A check was made to ensure that two different nodes on the presumed free surface are not mapped into the same location when modifying the shape of the free surface. The procedure was repeated until the error e at each node on the free surface DEF was less than 0.1. It was found computationally very efficient to switch to the following method for adjusting the free surface subsequently. Let H and K be two successive nodes on the free surface downstream from G, $\mathbf{N}$ be the normal vector to the previously assumed free surface at K, $\mathbf{T}$ be a vector parallel to $\mathbf{v}$ computed at K and we wish to find the new location K′ of K. It is at the point of intersection K′ of $\mathbf{N}$ with the circular arc that passes through G and H, and has a tangent vector at K′ parallel to $\mathbf{T}$. This eliminates the likelihood of two nodes ending up at the same location during a refinement of the shape of the free surface. With this technique the magnitude of e at each node point on the surface DEF could be reduced to less than 5% and the average of $|e|$ for all nodes on DEF to less than 1.5% in at most six iterations.

COMPUTATION AND DISCUSSION OF RESULTS

The finite element program developed earlier [6] to solve the companion problem of a rigid rod penetrating into a deformable target was modified to study the present problem. It employs 6-noded triangular elements and within each element the velocity (pressure) field is approximated by a quadratic (linear) function defined in terms of its values at 6 (3 corner) nodes. Thus both the velocity and pressure fields are continuous across interelement boundaries. We note the element satisfies the Babuška–Brezzi [12] condition. The velocity boundary condition in (16.2) is accounted for by using the method of Lagrange multipliers. The sample problem used to establish the validity of the code has been discussed in [6].

In Fig. 2 is plotted the computed velocity field for $\alpha = 5.1$. The details of the velocity field within the vicinity of the point where the curvature of the free surface changes sharply are also shown. As is rather obvious from the plotted results the Lagrange multipler method is quite effective in satisfying the essential boundary condition (16.2) on the cavity surface. We note that on the computed free surface the velocity of points is along the tangent to the surface. All of the results presented herein are for a fixed shape of the cavity given by

$$z = 0.04r^4.$$

This shape of the cavity was chosen after several trials; the selection criterion being that the

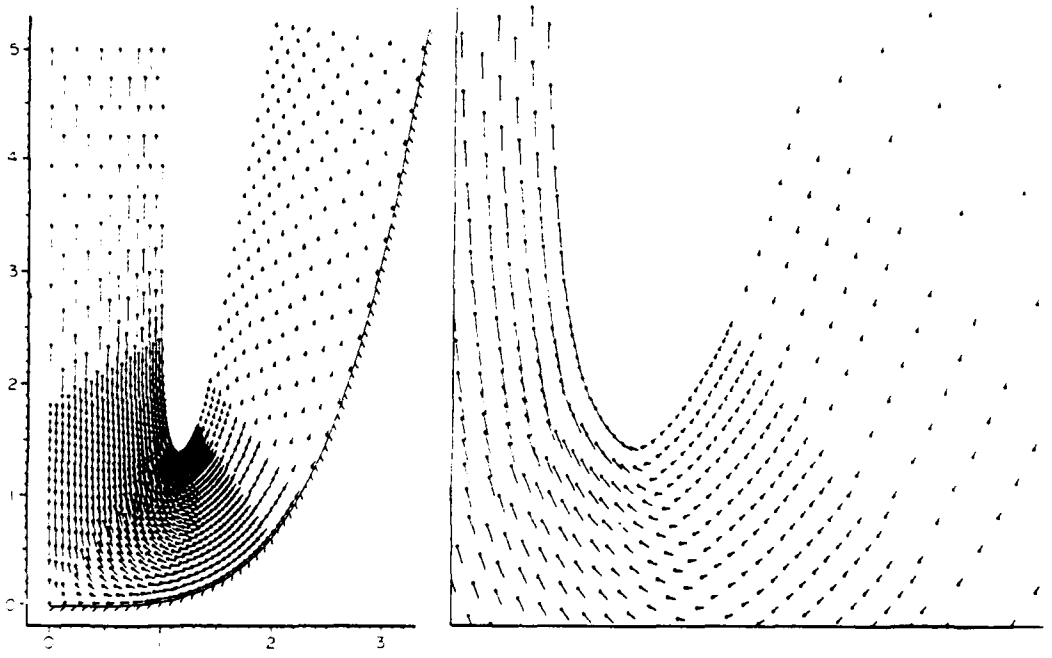

Fig. 2. The computed velocity field for $\alpha = 5.1$.

part of the surface over which the deformed rod particles exhibit a tendency to separate away from the surface BC is as small as possible. Ideally the contact should be maintained over all of BC but such a goal proved essentially impossible to attain especially for different striking speeds of the rod.

The velocity field for other values of α was quite similar to that shown in Fig. 2. As the speed of the rod increased the free surface moved away from the fixed cavity so that the thickness of the region at the outlet increased. The shapes of the free surface for different values of α are shown in Fig. 3. The radius of curvature near the bottom of the surface decreases sharply as the speed of the rod is increased. The plot of the thickness at the outlet versus α in Fig. 3 shows

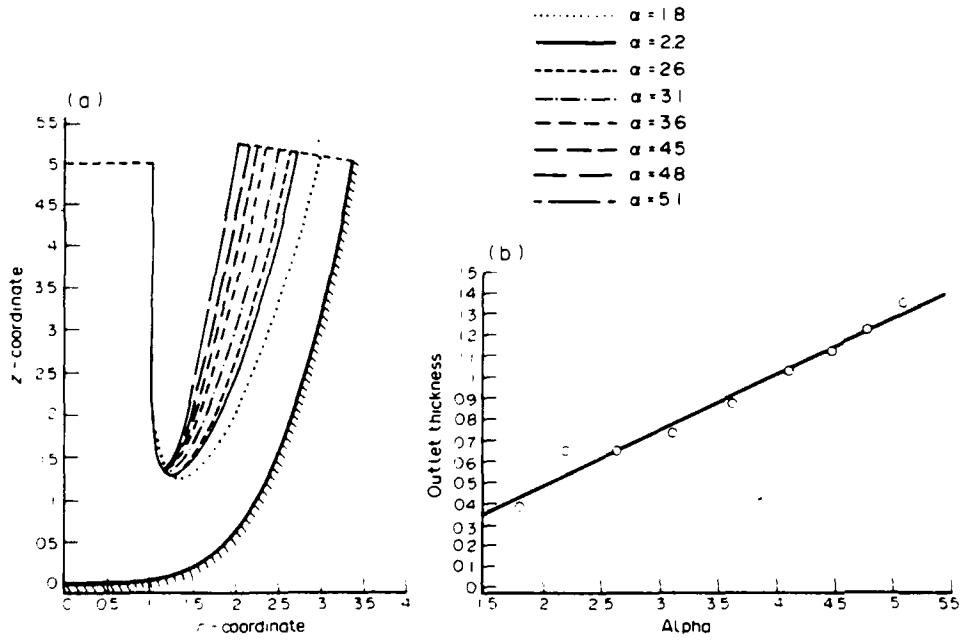

Fig. 3. a. Shapes of the free surface for different values of α. b. Thickness of the outlet region versus α.

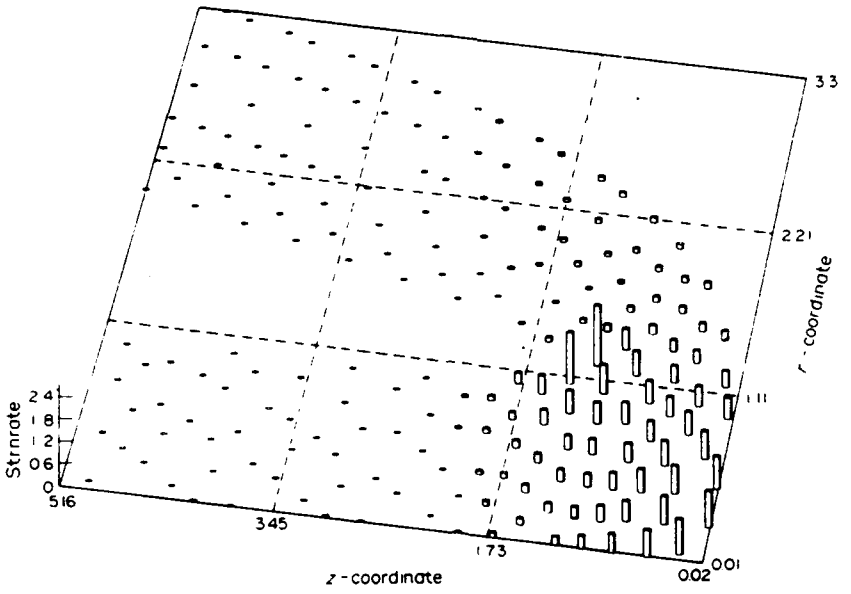

Fig. 4. Variation of the second invariant I of the stretching tensor $\mathbf{D}$ in the deforming region.

that the thickness increases linearly with α. Since the speed of the rod at the inlet is always taken to be 1.0, the speed of the particles at the outlet decreases so as to satisfy the balance of mass.

Figure 4 depicts the variation of the second invariant I of the strain-rate tensor $\mathbf{D}$ in the deforming region. As one would expect severe deformations take place in the region near the bottom of the cavity. Larger values of I occur near the bottom of the free surface where the flow reverses. For typical values of the radius of the penetrator these non-dimensional values of I are to be multiplied by 10^5 indicating thereby that peak strain-rates of the order of 10^5–$10^6\ s^{-1}$ occur in the vicinity of the point on the free surface where the flow reverses. We note that the

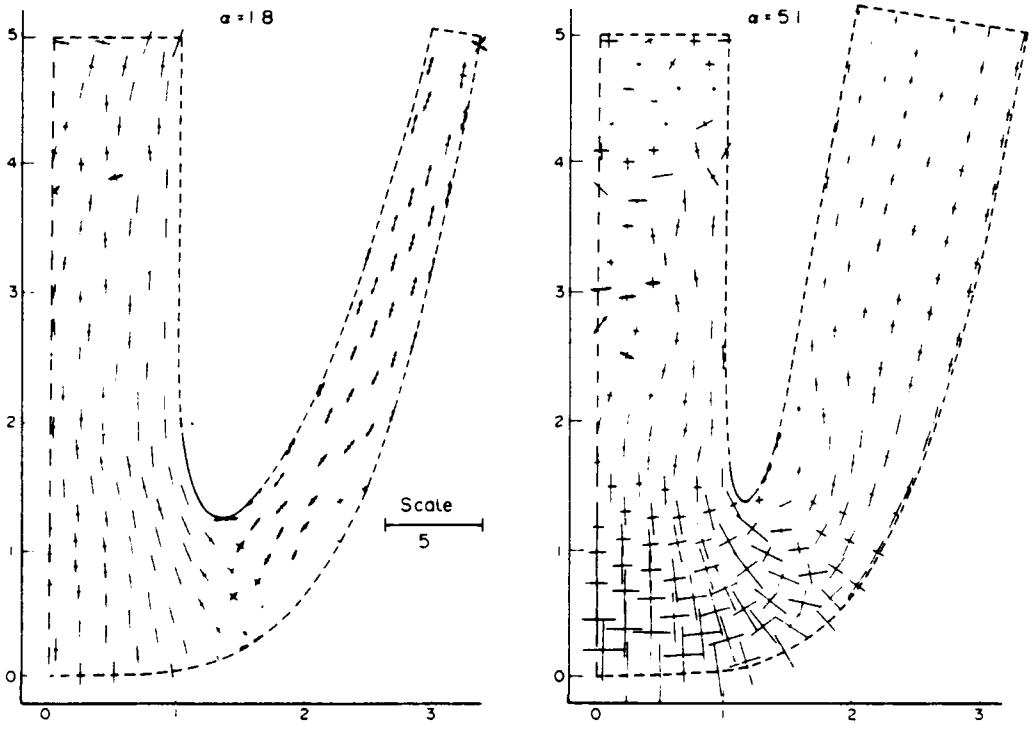

Fig. 5. Principal stresses in the deforming region.

non-dimensional values of I and their locations in the deforming region did not vary much with α. In Figs 5 and 6 are plotted, respectively, the principal stresses and the hydrostatic pressure in the deforming region for two different values of α. The lines are oriented along the axes of principal stresses and their lengths are proportional to the magnitudes of principal stresses at that point. The arrows at the ends of a line indicate that the corresponding principal stress is tensile otherwise it is compressive. Whereas for $\alpha = 1.8$ the material particles whose velocity in the z-direction is opposite to that of the incoming rod experience tensile stresses such is not the case at the higher value of α. This transition seems to take place around $\alpha = 3.6$. For $\alpha = 1.8$ one of the principal stresses at points in the region between the free surface and the bottom of the cavity is compressive; the other one is essentially zero. At the higher value of α both principal stresses are compressive. This is possibly due to the increase in the hydrostatic pressure (cf. Fig. 6) with the speed of the rod. Since the strain rates at points near the inlet and the outlet surface are negligibly small, and the values of stresses at these points, as given by

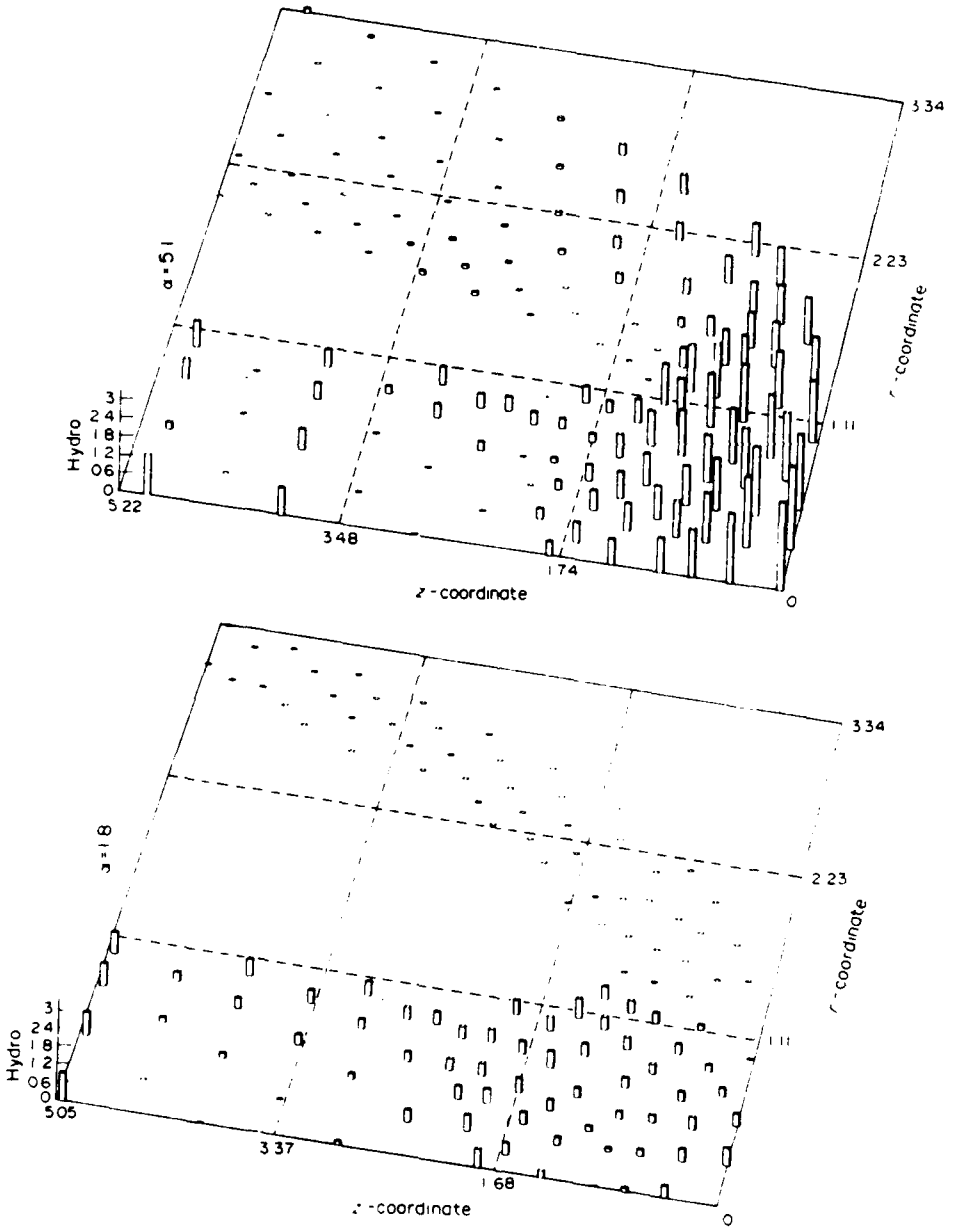

Fig. 6. Distribution of the hydrostatic pressure p in the deforming region.

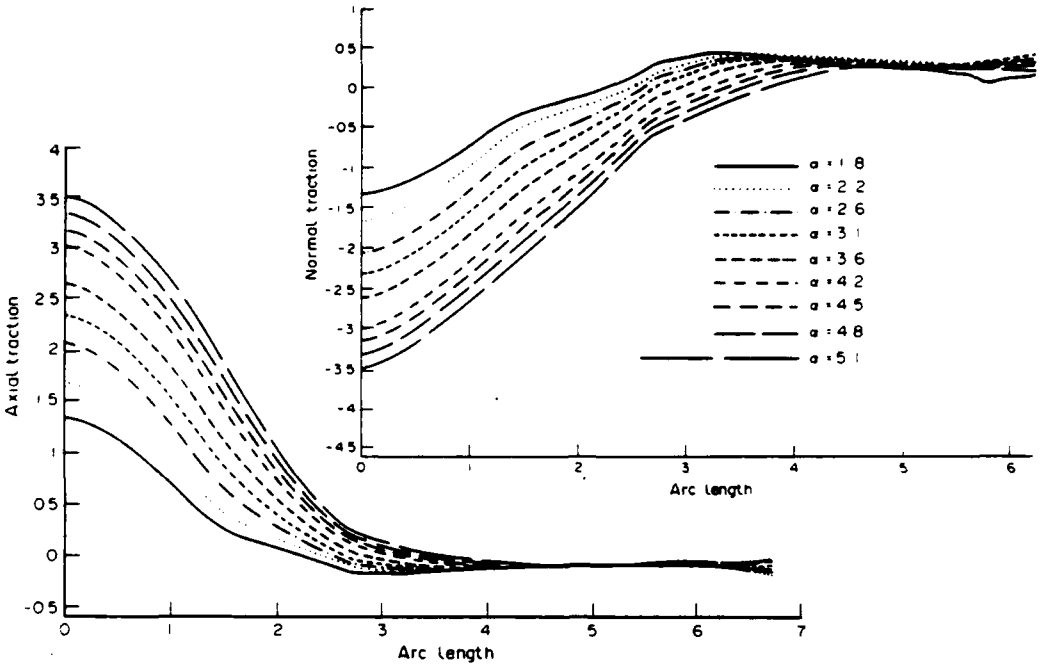

Fig. 7. Variation of the normal and axial tractions on the cavity wall.

eqn (3), are computed by taking the ratio of two small numbers, the magnitudes of stresses at these points may not be very accurate. This is one possible explanation for the small tensile stresses at points near the inlet and outlet surfaces. At a few isolated points in the vicinity of the bounding surfaces near the inlet and outlet regions the computed values of the hydrostatic pressure were relatively small negative numbers.

There is a tendency for the material particles to leave the cavity wall near the outlet region. This is indicated by the negative values of the computed normal traction at these points. The normal tractions and the axial tractions at different points on the cavity wall are plotted in Fig. 7. The arc length along the cavity surface is measured from the point of intersection of the cavity and the axis of the rod. For the same cavity surface the point where separation tends to occur moves away from the centroidal axis of the rod as the speed of the rod is increased. We note that in our computations material particles were not allowed to leave the cavity surface. Since the magnitude of the normal tractions at these points is rather small and the distance of these points from the center of the rod is of the order of $2r_0$, the computed results especially in the severely deformed region near the bottom of the cavity are quite meaningful. It is now obvious that to keep, say, the horizontal distance of the point on the cavity wall where separation tends to occur from the centroidal axis of the rod constant, the shape of the cavity should be adjusted as the rod speed is varied. The axial traction plotted in Fig. 7 indicates that the contribution to the total axial force from points where flow separation would have occurred is very small. This is due to the fact that the angle between the cavity surface at these points and the axis of the rod is very small so that the normal to the cavity surface at these points is essentially perpendicular to the rod axis.

How the total axial force acting on the cavity surface and experienced by the rod depends upon α is shown in Fig. 8. Unlike the case of a rigid rod penetrating into a rigid/perfectly plastic target where the axial force acting on the penetrator depended weakly on the penetrator speed, here the dependence of the axial force upon α is rather strong. We note that whereas herein the calculations have been performed with one cavity surface, in the actual penetration problem the surface separating the deforming penetrator and target regions will alter with the speed of the penetrator when all other parameters are kept fixed. In the approximate theory of Tate [13] the axial force acting at the penetrator/target interface is presumed to be constant. We have not investigated the dependence of the axial force upon the shape of the assumed cavity. Since there is very little experimental data available in the open literature it is hard to

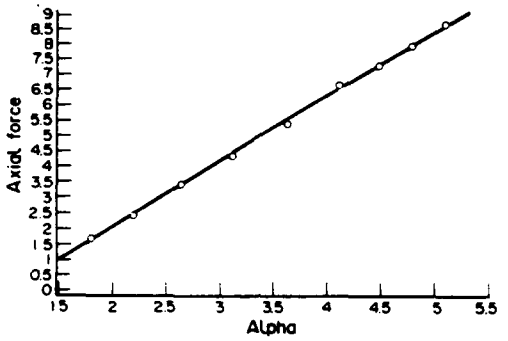

Fig. 8. Dependence of the total axial force acting on the cavity wall upon α.

judge whether or not the cavity surface envisaged here is close to those observed experimentally.

We note that strain-rates and therefore the rod deformations are negligibly small near the inlet and outlet regions. This ensures that the assumed finite region considered for solving the problem numerically is sufficient. The computed solution seemed to be stable in the sense that either superimposed small perturbations died out to zero or following slightly different paths gave the same solution.

CONCLUSIONS

For the fixed cavity the thickness at the outlet increases linearly with α, and the total axial force acting on the cavity wall depends strongly upon α. Most severe deformations occur in the region near the cavity bottom and the point where the curvature of the free surface changes. Peak strain-rates in the range 10^5–$10^6\ s^{-1}$ invariably occurred at or near the bottom E (Fig. 1) of the free surface. The hydrostatic pressure increases considerably with α. Whereas at lower speeds of the rod tensile stresses developed at points on the exist side of the flow these were overcome by the increase in the value of the hydrostatic pressure at higher speeds of the rod. The point on the cavity wall where the flow had a tendency to separate from the wall moved away from the axis of the rod as the striking speed increased.

Acknowledgement—This work was supported by the U.S. Army Research Office Contract DAAG 29-85-K-0238 to the University of Missouri-Rolla.

REFERENCES

[1] T. W. WRIGHT, A survey of penetration mechanics for long rods. In *Lecture Notes in Engineering*, Vol. 3, Computational Aspects of Penetration Mechanics (Edited by J. Chandra and J. Flaherty). Springer-Verlag, New York (1983).
[2] M. E. BACKMAN and W. GOLDSMITH, *Int. J. Engng Sci.* **16**, 1 (1978).
[3] G. H. JONAS, and J. A. ZUKAS, *Int. J. Engng Sci.* **16**, 879 (1978).
[4] C. E. ANDERSON JR and S. R. BODNER, *Third TACOM Armor Coordinating Conference*, Monterey, Calif. (1987).
[5] M. RAVID and S. R. BODNER, *Int. J. Engng Sci.* **21**, 577 (1983).
[6] R. C. BATRA and T. W. WRIGHT, *Int. J. Engng. Sci.* **24**, 41 (1986).
[7] W. PRAGER and P. HODGE, *Theory of Perfectly Plastic Solids*. Dover, New York (1968).
[8] E. BECKER, G. CAREY and J. T. ODEN, *Finite Elements—An Introduction*, Vol. 1. Prentice-Hall, Englewood Cliffs, N.J. (1981).
[9] O. C. ZIENKIEWICZ, E. ONATE and J. C. HEINRICH, *Int. J. Numer. Meths Engng* **17**, 1497 (1981).
[10] J. T. ODEN and T. L. LIN, *Comp. Meth. Appl. Mechs. Engng* **57**, 297 (1986).
[11] R. C. BATRA, M. LEVINSON and E. BETZ, *Int. J. Numer. Meths Engng* **10**, 767 (1976).
[12] G. J. CAREY and J. T. ODEN, *Finite Elements—A Second Course*, Vol. 2. Prentice Hall, Englewood Cliffs, N.J. (1983).
[13] A. TATE, *J. Mechs. Phys. Solids* **15**, 387 (1967); *ibid*, **17**, 141 (1969).

(*Received* 30 *June* 1987)

Int. J. Engng Sci. Vol. 26, No. 7, pp. 741–751, 1988
Printed in Great Britain. All rights reserved

0020–7225/88 $3.00 + 0.00
Copyright © 1988 Pergamon Press plc

STEADY STATE PENETRATION OF COMPRESSIBLE RIGID PERFECTLY PLASTIC TARGETS

R. C. BATRA and T. GOBINATH
Department of Engineering Mechanics, University of Missouri-Rolla, Rolla, MO 65401-0249, U.S.A.

Abstract—Steady state axisymmetric deformations of a homogeneous, isotropic, compressible and rigid perfectly plastic target being penetrated by a rigid cylindrical penetrator with a hemispherical nose are studied by the finite element method. The steady state is reached with respect to an observer situated on the penetrator nose and moving with it. Tillotson's equation, restricted to mechanical deformations, is used to express the pressure as a function of the mass density. Contact between the penetrator and the target is assumed to be smooth. The effect of compressibility of the material is delineated by comparing results for compressible and incompressible materials. Also studied is the effect of the penetrator speed on target deformations.

INTRODUCTION

In an attempt to shed some light on the validity of the approximations made in simple theories of penetration due to Alekseevskii [1] and Tate [2], and to understand better the significance of various kinematic variables, Batra and Wright [3] studied in detail a steady state penetration problem that simulates the following situation. Suppose that the penetrator is in the intermediate stages of penetration so that the active target/penetrator interface is at least one or two penetrator diameters away from either target face, and the remaining penetrator is much longer than several diameters and is still travelling at a uniform speed. This stage of penetration can be idealized as one in which deformations of the target appear to be steady to an observer situated on the penetrator nose. Wright and Batra [3] presumed that the target is made of a rigid/perfectly plastic material, and is being penetrated by a long cylindrical rigid rod with a hemispherical nose. Subsequently Batra [4] showed that the axial resisting force experienced by the rigid penetrator is considerably reduced if its nose shape is ellipsoidal rather than hemispherical and also investigated the effect of the dependence of the flow stress upon the strain-rate. He [5] has extended this work to the case when the target material is thermally softening but strain and strain-rate hardening.

Pidsley [6] recently studied a complete penetration problem in which both target and penetrator materials were assumed to be compressible rigid/perfectly plastic. Whereas he gave a detailed numerical solution for one set of material and geometric parameters, we study the steady state penetration problem similar to the one analyzed by Batra and Wright [3] and investigate the effect of the speed of the penetrator and the compressibility of the target material. We hope that the kinematic and stress fields found in this study will be useful in identifying key variables to be included in simpler engineering theories of target penetration. Since the continuity equation has no diffusive term, it is more challenging to solve the problem numerically for compressible materials. Pidsley used the finite difference code HELP developed by Hageman and Walsh [7] to solve the problem. However, we use the finite element method and have developed the requisite code.

We note that no failure or fracture criterion is included in our study. Thus the target material is assumed to undergo unlimited amount of deformations.

FORMULATION OF THE PROBLEM

We describe the axisymmetric deformations of the target with respect to a set of cylindrical coordinate axes with origin at the center of the hemispherical nose of the rigid penetrator and z-axis pointing into the target. Equations governing the steady-state deformations of the target

are

$$\operatorname{div}(\rho \mathbf{v}) = 0, \tag{1.1}$$

$$\operatorname{div} \boldsymbol{\sigma} = \rho(\mathbf{v} \cdot \operatorname{grad})\mathbf{v}. \tag{1.2}$$

Here ρ is the current mass density of a target material particle, $\mathbf{v}$ is the velocity relative to an observer situated on the penetrator nose tip and moving with it, $\boldsymbol{\sigma}$ is the Cauchy stress tensor, and the operators grad and div signify the gradient and divergence operators on fields defined in the present configuration. Equations (1.1) and (1.2) express, respectively, the balance of mass and the balance of linear momentum with zero body forces.

We presume that the target material is compressible and obeys the Von-Mises yield criterion and the associated flow rule. That is†

$$\boldsymbol{\sigma} = -p(\rho)\mathbf{1} + \frac{\sigma_0}{\sqrt{3}I}\bar{\mathbf{D}}, \tag{2.1}$$

$$\bar{\mathbf{D}} = \mathbf{D} - \frac{1}{3}(\operatorname{tr}\mathbf{D})\mathbf{1}, \tag{2.2}$$

$$\mathbf{D} = (\operatorname{grad}\mathbf{v} + (\operatorname{grad}\mathbf{v})^T)/2, \tag{2.3}$$

$$I^2 = \frac{1}{2}\operatorname{tr}(\bar{\mathbf{D}}^2), \tag{2.4}$$

$$p(\rho) = A\left(\frac{\rho}{\rho_0} - 1\right) + B\left(\frac{\rho}{\rho_0} - 1\right)^2. \tag{2.5}$$

In these equations σ_0 is the flow stress of the target material in simple compression, ρ_0 is the mass density of the undeformed target material, A and B are material constants, $\mathbf{D}$ is the strain-rate tensor and $\bar{\mathbf{D}}$ its deviatoric part. Equation (2.5) is obtained from the Tillotson equation by neglecting the parts that apply to hot expanded metal states and the change in temperature of a material point. The constant A is related to the bulk modulus of the material. Equation (2.1) may be regarded as a constitutive relation of a compressible Non-Newtonian fluid with shear viscosity given by $\sigma_0/2\sqrt{3}I$. Equation (2) when substituted into (1.2) gives

$$-\operatorname{grad} p + \frac{\sigma_0}{\sqrt{3}}(\operatorname{div}((\operatorname{grad}\mathbf{v} + (\operatorname{grad}\mathbf{v})^T)/2I) - \operatorname{grad}((\operatorname{div}\mathbf{v})/3I)) = \rho(\mathbf{v} \cdot \operatorname{grad})\mathbf{v} \tag{3}$$

which along with (1.1) are the field equations for ρ and $\mathbf{v}$.

We now non-dimensionalize the variables as follows:

$$\bar{r} = r/r_0, \quad \bar{z} = z/r_0, \quad \bar{\mathbf{v}} = \mathbf{v}/v_0, \quad \bar{\boldsymbol{\sigma}} = \boldsymbol{\sigma}/\sigma_0, \quad \bar{p} = p/\sigma_0, \quad \bar{\rho} = \rho/\rho_0,$$
$$\bar{A} = A/\sigma_0, \quad \bar{B} = B/\sigma_0. \tag{4}$$

Here r_0 is the radius of the cylindrical part of the penetrator, v_0 its speed in the z-direction and the pair (r, z) denotes the cylindrical co-ordinates of a target particle. Hereafter we use only the non-dimensional variables and drop the superimposed bars. Equations (1.1) and (3) in terms of the non-dimensional variables are

$$(\operatorname{grad}\rho) \cdot \mathbf{v} + \rho(\operatorname{div}\mathbf{v}) = 0, \tag{5.1}$$

$$-\operatorname{grad} p + \frac{1}{\sqrt{3}}(\operatorname{div}((\operatorname{grad}\mathbf{v} + (\operatorname{grad}\mathbf{v})^T)/2I) - \operatorname{grad}((\operatorname{div}\mathbf{v})/3I)) = \alpha(\mathbf{v} \cdot \operatorname{grad})\mathbf{v}, \tag{5.2}$$

where

$$\alpha = \rho_0 v_0^2/\sigma_0 \tag{6}$$

is a non-dimensional number.

† This constitutive relation is discussed briefly in the note at the end of the paper

For the boundary conditions on the target/penetrator interface we take

$$\mathbf{v}\cdot\mathbf{n}=0, \tag{7.1}$$

$$\mathbf{t}\cdot(\boldsymbol{\sigma}\mathbf{n})=0, \tag{7.2}$$

where $\mathbf{n}$ and $\mathbf{t}$ are, respectively, unit normal and tangent vectors at a point on the interface. The boundary conditions (7) ensure that target particles do not penetrate into the rigid penetrator and the contact surface is frictionless. At points far away from the penetrator nose, we assume that

$$|\mathbf{v}+\mathbf{e}|\to 0 \quad \text{as} \quad (r^2+z^2)^{1/2}\to\infty, \qquad z>-\infty, \tag{8.1}$$

$$|\boldsymbol{\sigma}\mathbf{n}|\to 0 \quad \text{as} \quad z\to-\infty, \qquad r\geq 1. \tag{8.2}$$

In eqn (8.1) $\mathbf{e}$ is a unit vector along the z-axis. This boundary condition states that target particles far from the penetrator but not on the back surface appear to move as a rigid body and those on the back surface are traction free. In order to state the problem precisely one needs to specify the rates at which quantities in eqn (8) decay to zero. We now assume that the nonlinear and coupled equations (5) under the boundary conditions (7) and (8) have a solution and find an approximation to that solution by the finite element method.

FINITE ELEMENT FORMULATION OF THE PROBLEM

For a numerical solution of the problem we first recall that the target deformations are assumed to be axisymmetric and therefore consider the finite region shown in Fig. 1 and

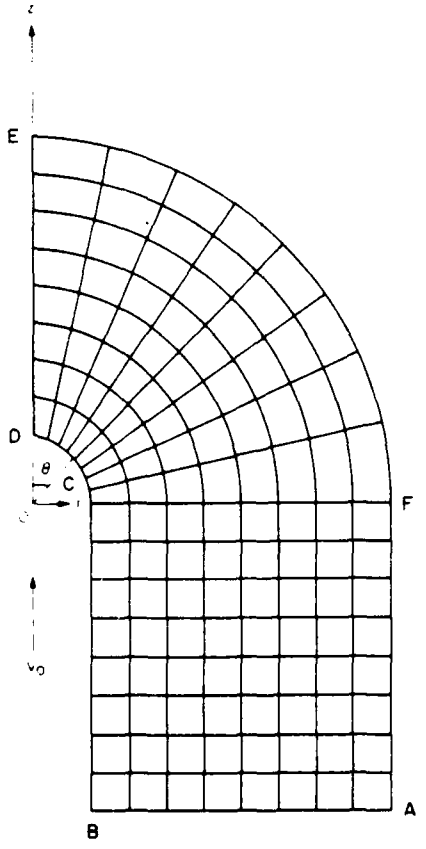

Fig. 1. The finite region studied and its discretization.

impose the following boundary conditions:

$$\sigma_{zz} = 0, \qquad v_r = 0 \text{ on the bottom surface AB,} \tag{9.1}$$

$$t \cdot \sigma n = 0, \qquad \mathbf{v} \cdot \mathbf{n} = 0 \text{ on the target/penetrator interface BCD,} \tag{9.2}$$

$$\sigma_{rz} = 0, \qquad v_r = 0 \text{ on the axis of symmetry DE,} \tag{9.3}$$

$$v_r = 0, \qquad v_z = -1.0 \text{ on the boundary surface EFA.} \tag{9.4}$$

The adequacy of the studied region is verified by ensuring that the computed results especially in the vicinity of the target/penetrator interface are unaffected by the location of the boundary EFA.

Referring the reader to Becker *et al.* [8] for details, we note that a weak formulation of the problem defined on the region R (shown enclosed by ABCDEFA in Fig. 1) by eqns (5) and boundary conditions (9) is that equations

$$\int_R \psi((\operatorname{grad}\rho)\cdot\mathbf{v} + \rho(\operatorname{div}\mathbf{v}))\,dv = 0, \tag{10.1}$$

$$\int_R p(\operatorname{div}\boldsymbol{\phi})\,dv - \frac{1}{2\sqrt{3}}\int \frac{1}{I}\tilde{\mathbf{D}}:(\operatorname{grad}\boldsymbol{\phi} + (\operatorname{grad}\boldsymbol{\phi})^T)\,dv = \alpha\int_R ((\mathbf{v}\cdot\operatorname{grad})\mathbf{v})\cdot\boldsymbol{\phi}\,dv, \tag{10.2}$$

hold for arbitrary smooth functions ψ and $\boldsymbol{\phi}$ defined on R such that $\phi_r = 0$ on AB, $\boldsymbol{\phi} = 0$ on EFA and $\boldsymbol{\phi}\cdot\mathbf{n} = 0$ on the target/penetrator interface BCD. In these equations $\mathbf{A}:\mathbf{B} = \operatorname{tr}(\mathbf{A}\mathbf{B}^T)$ for linear transformations $\mathbf{A}$ and $\mathbf{B}$. Since these equations are nonlinear in $\mathbf{v}$ and ρ, the following iterative technique has been employed. At the ith iteration, equations

$$\int_R \psi((\operatorname{grad}\rho^i)\cdot\mathbf{v}^{i-1} + \rho^{i-1}(\operatorname{div}\mathbf{v}^i))\,dv = 0, \tag{10.3}$$

$$\frac{1}{2\sqrt{3}}\int_R \frac{1}{I^{i-1}}\mathbf{D}^i:(\operatorname{grad}\boldsymbol{\phi} + (\operatorname{grad}\boldsymbol{\phi})^T)\,dv + \alpha\int_R ((\mathbf{v}^{i-1}\cdot\operatorname{grad})\mathbf{v}^i)\cdot\boldsymbol{\phi}\,dv$$
$$= \left[\int p(\rho^{i-1})(\operatorname{div}\boldsymbol{\phi})\,dv + \frac{1}{3\sqrt{3}}\int_R \frac{1}{I^{i-1}}[(\operatorname{tr}\mathbf{D}^{i-1})\operatorname{div}\boldsymbol{\phi}]\,dv\right] \tag{10.4}$$

are solved for v^i and ρ^i. The iterative process is stopped when at each nodal point

$$\|v^i - v^{i-1}\| + |\rho^i - \rho^{i-1}| \le \varepsilon[\|v^{i-1}\| + |\rho^{i-1}|] \tag{10.5}$$

where $\|\mathbf{v}\|^2 = v_r^2 + v_z^2$, and ε is a preassigned small number.

The lack of a diffusive term in the balance of mass eqn (5.1) necessitates that the test functions ψ and the trial solutions ρ be chosen from different functional spaces. This is usually referred to as Petrov–Galerkin formulation [9]. We use 9-noded rectangular elements for $\mathbf{v}$ and the four-noded rectangular elements for ρ and employ the basis functions given by Heinrich *et al.* [10] to generate the test functions ψ. These basis functions involve four constants and the rate of convergence of the solution depends rather strongly upon the values of these constants. The test functions $\boldsymbol{\phi}$ and the trial solutions $\mathbf{v}$ are taken from the same space of functions. Thus we have used the Petrov–Galerkin formulation for the continuity equation and the Galerkin formulation for the balance of linear momentum.

COMPUTATION AND DISCUSSION OF RESULTS

A computer code based on eqns (10.3) and (10.4), and employing 9-noded rectangular elements has been developed. The two components of the velocity are taken as unknowns at each node and the mass density is assumed to be unknown only at the four corner nodes. The accuracy of the computer code was established by solving a hypothetical problem involving the flow of a compressible Navier–Stokes fluid in a circular pipe and achieving a favorable comparison between the computed and analytical results. The sample problem studied and the

comparison between the computed and analytical results is given in the Appendix. Even though the formulation of the problem does not require that the mass density be prescribed on any part of the boundary, the numerical solution of the problem necessitated that it be assigned values on a part of the boundary. In the results presented below the non-dimensional mass density was set equal to 1.0 on the part EFA of the boundary. Also the boundary condition $\mathbf{v} \cdot \mathbf{n} = 0$ on the target/penetrator interface BCD was satisfied by using the method of Lagrange multipliers. The finite element discretization of the region studied is depicted in Fig. 1. Note that only one non-dimensional number α governs the deformations of the target material. Thus all of the results below are expressed in terms of α. However the compressibility of the material is governed by the values of A and B in eqn (2.5) which we took as $A = 144.231$, $B = 125.0$. These values, taken from Pidsley's [6] paper, are for aluminum. For a prescribed value of α, the problem was first solved by presuming that the target material is incompressible. This solution for v_r and v_z and $\rho = 1.0$ everywhere was taken as the initial estimate of the solution for the compressible target material. We recall that the basis functions for ψ involve four constants. The number of iterations required to obtain the converged solution depended rather strongly upon the values selected for these constants. In general, however, the number of iterations needed for the solution to converge increased with the increase in the value of α. The parameter ε in the convergence criterion (10.5) was assigned the value 0.04.

In Fig. 2 are plotted the variation of the normal stress, tangential velocity and the second invariant I of the strain-rate tensor on the penetrator nose for $\alpha = 5.36$ and for compressible and incompressible target materials. The compressibility of the target material affects most the values of I near the penetrator nose-tip. Over most of the nose surface the values of I and the normal stress are lower for the compressible target material as compared to that when the

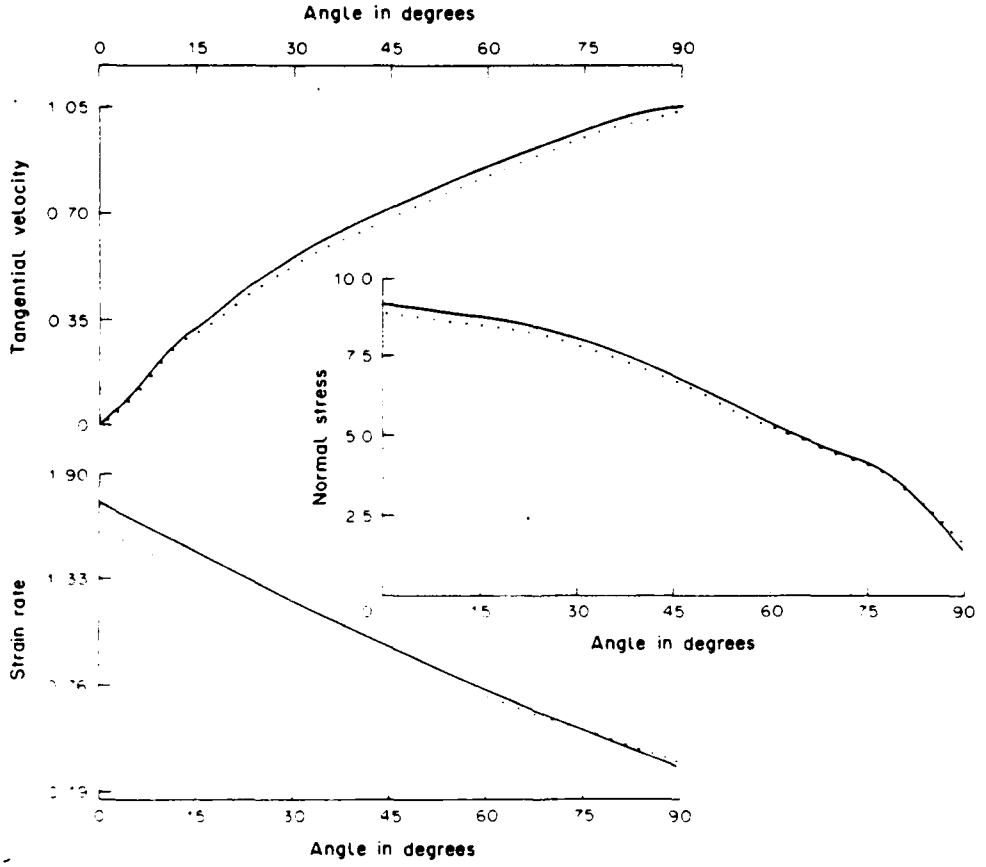

Fig. 2. The variation of the normal stress, tangential velocity and the second strain-rate invariant I on the penetrator nose for $\alpha = 5.36$. —— incompressible material, · · · · · compressible material.

target material is modelled as incompressible. Whereas the peak value of I at the penetrator nose-tip drops by 8.78% when the target material is presumed to be compressible, that of the normal stress decreases by only 3.19%. In the immediate vicinity of the nose tip the tangential velocities for compressible and incompressible targets essentially coincide with each other. However for the angular position θ greater than 12°, the tangential velocity for the compressible target is lower than that for the incompressible target.

Figure 3 depicts the effect of the compressibility of the target material on the variation of the normal stress, strain-rate invariant I and the relative z-velocity along the axial line. As evidenced by the values of I, most of the target deformations occur within a distance of 1.5 times the radius of the penetrator for both compressible and incompressible target materials. In each case the values of I drop off to zero at points on the axial line whose distance from the nose surface is greater than twice the radius of the penetrator. Typically these non-dimensional values of I need to be multiplied by 10^5 to get their dimensional counterparts. Thus peak strain-rates of the order of $10^5\,s^{-1}$ occur for both compressible and incompressible target materials. The values of absolute z-velocity decay to zero a little bit slowly for compressible targets as compared to that for incompressible targets. The rate of decay of the absolute values of σ_{zz} along the axial line in the two cases is nearly the same. The values of $|\sigma_{zz}|$ are less when the target material is modeled as compressible as compared to that when it is taken to be incompressible. The difference between the two values is primarily due to the difference in the values of the hydrostatic pressure in the two cases. For $0 \le z \le 2$, this difference in the values of p stayed nearly constant and equalled 0.48.

Figure 4 shows the variation of v_z with r at $z = 0$ and $z = -5.0$ and also the dependence of the axial resisting force F experienced by the penetrator upon α. For both compressible and incompressible target materials the axial resisting force F depends linearly upon α and the two lines are nearly parallel to each other. In each case the dependence of F upon α is rather weak

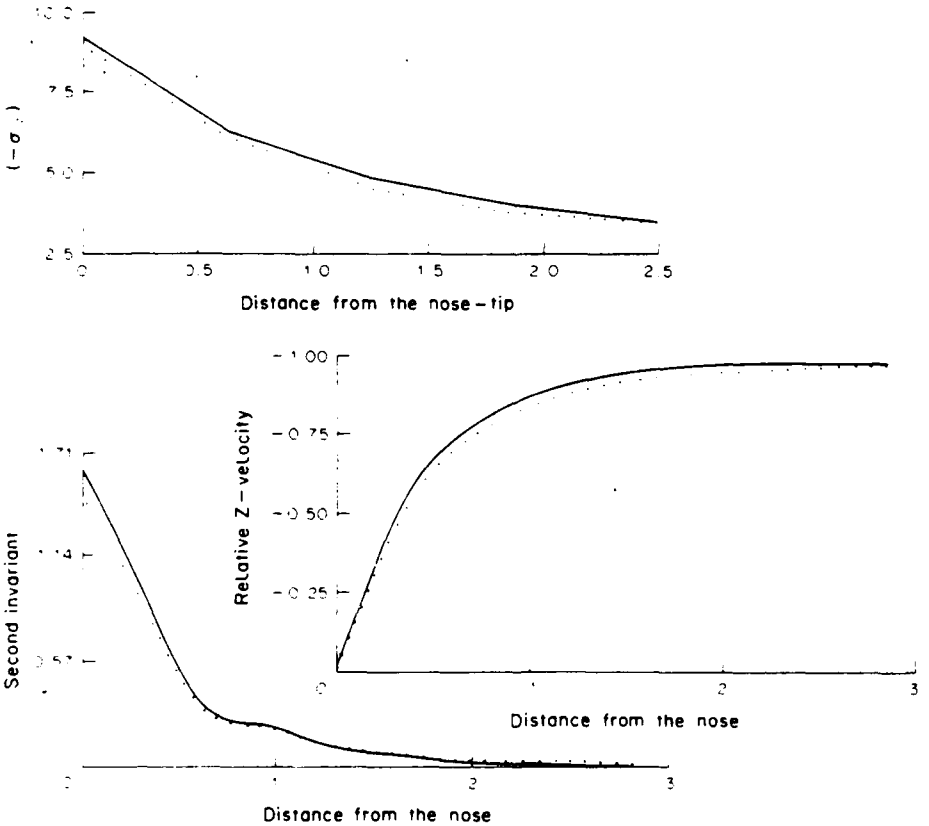

Fig. 3. Variations of $(-\sigma_{zz})$, z-velocity and the second strain-rate invariant I on the axial line for $\alpha = 5.36$. —— incompressible material, · · · · · compressible material.

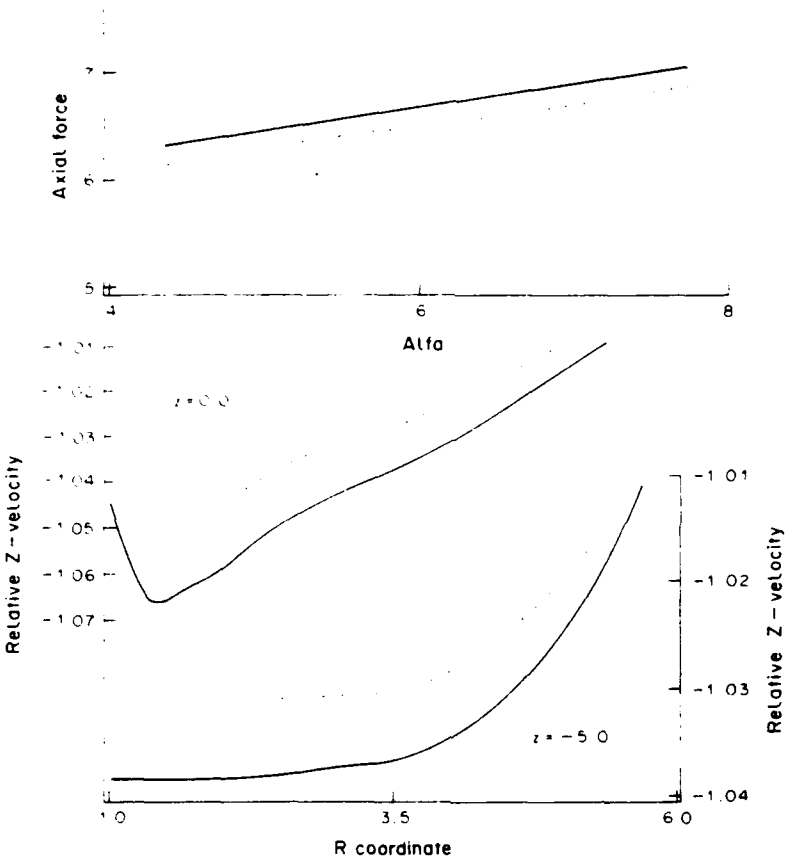

Fig. 4. Dependence of the axial force upon α; Variations of v_z with r on planes $z = 0$ and $z = -5.0$. $\alpha = 5.36$. —— incompressible material, · · · · · compressible material.

and explains why the choice of constant target resistance in the simple theory of Tate [2] gives good qualitative results. Note that the dimensional values of F equal $(\pi r_0^2 \sigma_0)$ times its non-dimensional values. The plots of v_z versus r indicate the deformations of the target spread farther to the side of the penetrator than ahead of it. This is true both for compressible and incompressible target materials. Whereas target points on the axial line and ahead of the penetrator situated at a distance of three times the penetrator radius have zero absolute z-velocity, that on the sides of the penetrator and situated at the same distance from the penetrator surface have non-zero z-velocity. The variation of v_z with r on the surface $z = -5.0$ indicates that the material in the region $1 \le r \le 3.5$ extrudes as a rigid block.

The value of the compression c, defined as $(1 - \rho^{-1})$, at the nose tip was found to depend linearly upon α, and for $4 \le \alpha \le 8$ the two are related by

$$c = (4.75 + 0.575\alpha)/100.$$

After having delineated the difference in the solutions for compressible and incompressible target materials we next studied the effect of the penetrator speed upon the deformations of the compressible target. We recall that the corresponding results for the incompressible target material have been given by Batra and Wright [3]. Results presented in Fig. 5 indicate that the speed of the penetrator has virtually no effect on the tangential velocity of the target particles abutting the penetrator hemispherical nose. However, the normal stress does increase with α on most of the nose surface except near its periphery where the normal stress decreases with α. The normal stress at $\theta = 65°$ seems to be affected little by the values of α. Such a behavior was also observed at $\theta = 45°$ for incompressible target materials [3]. The peak value of the normal stress, which occurs at the penetrator nose tip, increases from 7.25 to 9.5 when α is increased from 2.35 to 6.12. Whereas in the previous work [3], for $\alpha = 6.13$ the target particles seemed to

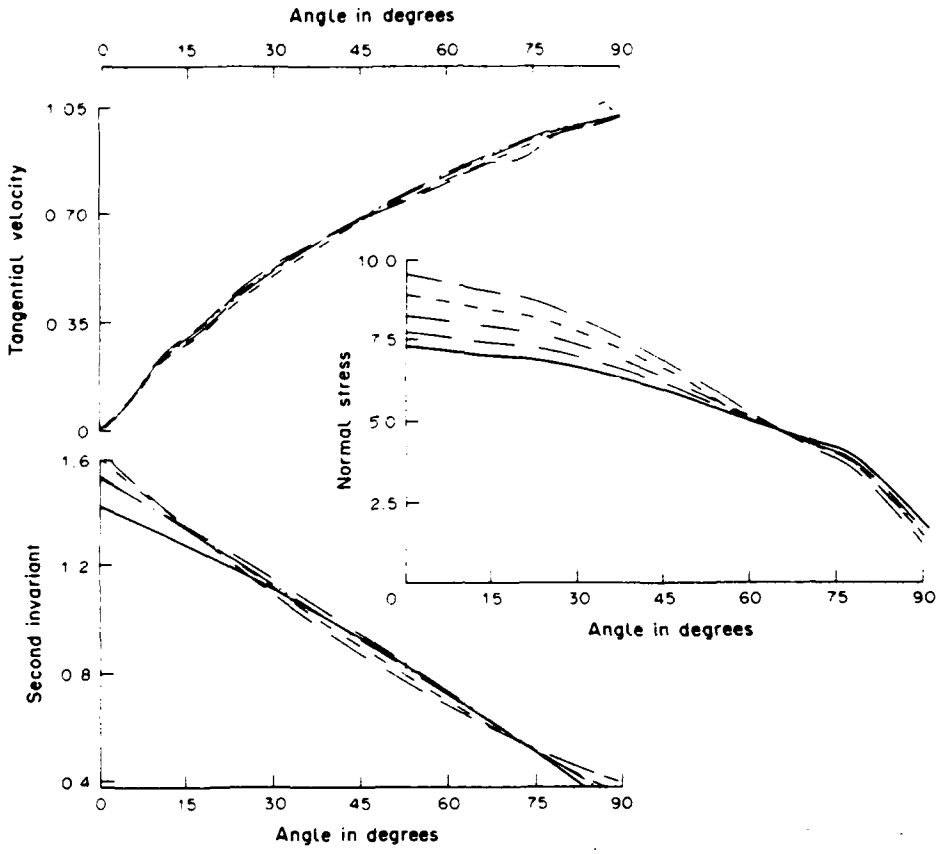

Fig. 5. Distribution of the tangential velocity, normal stress and the second strain-rate invariant on the hemispherical nose of the penetrator for different values of α and compressible target material. —— $\alpha = 2.63$; —·—·— $\alpha = 3.44$; ——··——·· $\alpha = 4.35$; - - - - $\alpha = 5.36$; ———— $\alpha = 6.49$.

separate away from the penetrator nose surface near its periphery, no such behavior was observed in the present case. The finite element mesh used herein is finer than the one employed earlier. Also the mass density is taken as the independent variable here whereas in [3] the hydrostatic pressure p was taken as an independent variable because of the assumption of incompressibility. The values of the second strain-rate invariant in the vicinity of the penetrator nose tip are affected most by α but those at points for which $20° \le \theta \le 70°$ seem to be affected less. The increase in the value of the normal stress on the penetrator nose with α occurs primarily because the hydrostatic pressure p increases with α.

In Fig. 6 is plotted the effect of α upon the variation of v_z, $(-\sigma_{zz})$ and I at target particles on the axial line ahead of the penetrator. The penetrator speed does not affect to any noticeable degree the values of I and v_z. However, the values of $(-\sigma_{zz})$ at points on the axial line increase with α; this increase is mainly due to the higher values of p. For all values of α considered here the target particles within a distance of almost three times the penetrator radius undergo deformations; those outside this region hardly deform.

On the axial line nearly uniaxial strain conditions prevail. Thus the magnitude of the deviatoric stress s_{zz}, defined as $p + \sigma_{zz}$, should equal 2/3 the flow stress. For points on the axial line for which $0.0 \le z \le 1.5$, and for $\alpha = 5.36$, s_{zz} was computed to be 0.771 and 0.741 for compressible and incompressible materials, respectively.

We note that the region studied is adequate since the target particles within a distance of one penetrator radius of the boundary EFA hardly deform and the deformation of particles situated within one penetrator radius of the boundary surface AB are independent of z.

We are not aware of any experimental work available in the open literature with which we could compare our computations. Nevertheless, the kinematic and stress fields found in this

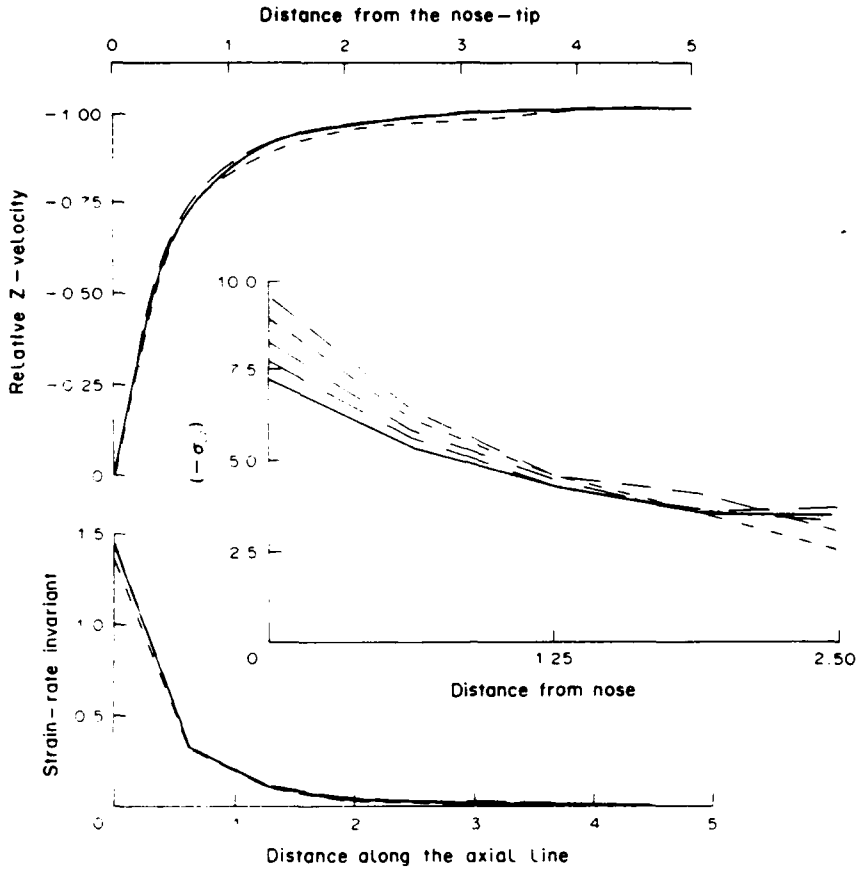

Fig. 6. Variation of the z-velocity, $(-\sigma_{zz})$ and the second strain-rate invariant I along the axis ahead of the penetrator for different values of α and compressible target material. See Fig. 5 for explanation.

study should help in devising or checking the results from simpler theories of target deformations.

CONCLUSIONS

For the same speed of the rigid cylindrical penetrator with a hemispherical nose, the peak values of the strain-rate invariant and the normal stress, both of which occur at the target particle situated at the penetrator nose-tip, are lowered by 8.78 and 3.19%, respectively, for compressible target materials as compared to that for incompressible materials. The axial resisting force experienced by the penetrator is nearly 10% less when the target material is compressible as compared to that when it is incompressible.

Both for compressible and incompressible target materials, significant deformations occur only at points that are less than three penetrator radii from the penetrator, and the target seems to deform farther to the side than ahead of the penetrator. In each case the target material adjacent to the sides of the penetrator appears to extrude rearwards as a uniform block that is separated from the stationary target by a deforming region.

Note added in proof

Recent unpublished work by Batra and Liu involving dynamic plane strain simple compression of viscoplastic solids defined by the constitutive relation (2.1) has shown that, for short times after the application of the load, material lines in a direction perpendicular to the axis of the compressive load are also shortened. The constitutive relation

$$\mathbf{\sigma} = -p(\rho)\mathbf{1} + \frac{\sigma_0}{\sqrt{3I}}\mathbf{D} \tag{N1}$$

with I defined by eqn (2.4) rules out this anomalous behavior. The constitutive relation (N1) can be rewritten as

$$\boldsymbol{\sigma} = -\left(p(\rho) - \frac{\sigma_0}{\sqrt{3I}}\,\mathrm{tr}\,\mathbf{D}\right)\mathbf{1} + \frac{\sigma_0}{\sqrt{3I}}\,\hat{\mathbf{D}}. \tag{N2}$$

Thus, for a given $\mathbf{D}$, eqns (2.1) and (N1) give identical values of the deviatoric stress.

For the steady state problem studied herein, constitutive relations (2.1) and (N1) give essentially the same results.

Acknowledgement—This work was supported by the U.S. Army Research Office contract DAAG29-85-K-0238 to the University of Missouri-Rolla.

REFERENCES

[1] V. P. ALEKSEEVSKII, *Combust. Expls Shock Waves* **2**, 63 (1966).
[2] A. TATE, *J. Mech. Phys. Solids* **15**, 387 (1967).
[3] R. C. BATRA and T. W. WRIGHT, *Int. J. Engng Sci.* **24**, 41 (1986).
[4] R. C. BATRA, *Int. J. Engng Sci.* **25**, 1131 (1987).
[5] R. C. BATRA, *Comput. Mech.* **3**, 1 (1988).
[6] P. H. PIDSLEY, *J. Mech. Phys. Solids* **32**, 315 (1984).
[7] L. J. HAGEMAN and J. M. WALSH, *HELP, A Multi-Material Eulerian Program for Compressible Fluid and Elastic-Plastic Flows in Two Space Dimensions and Time*. Systems Science and Software Report 3SR-350 (1971).
[8] E. BECKER, G. CAREY and J. T. ODEN, *Finite Elements—An Introduction*. Vol. 1. Prentice-Hall, Englewood Cliffs, N.J. (1981).
[9] T. J. R. HUGHES, *The Finite Element Method. Linear Static and Dynamic Finite Element Analysis*. Prentice-Hall, Englewood Cliffs, N.J. (1987).
[10] J. C. HEINRICH, P. S. HUYAKORN and O. C. ZIENKIEWICZ, *Int. J. Num. Meth. Engng* **11**, 131 (1977).

(*Received* 29 *October* 1987)

APPENDIX

In order to assess the validity of the developed finite element code and establish the reliability of the computed results we solved the following problem for compressible Navier–Stokes fluids. We replaced eqn (2.1) by

$$\boldsymbol{\sigma} = -p(\rho)\mathbf{1} + \hat{\mathbf{D}}, \qquad p(\rho) = \rho/100 \tag{A1}$$

and the balance of linear momentum (1.2) by

$$\mathrm{div}\,\boldsymbol{\sigma} = \boldsymbol{\rho}(\mathbf{v}\cdot\mathrm{grad}\,\mathbf{v}) + \mathbf{b} \tag{A2}$$

where b is the body force per unit mass. The fields

$$v_r = r^2/2, \qquad v_z = -rz/2, \qquad \rho = (z^2 - 1/r^2)/4, \tag{A3}$$

with

$$b_r = \frac{r^3}{200} + \frac{r^2z^2}{8} - \frac{r}{8} - \frac{11}{12}, \qquad b_z = \frac{z}{200} + z/4r \tag{A4}$$

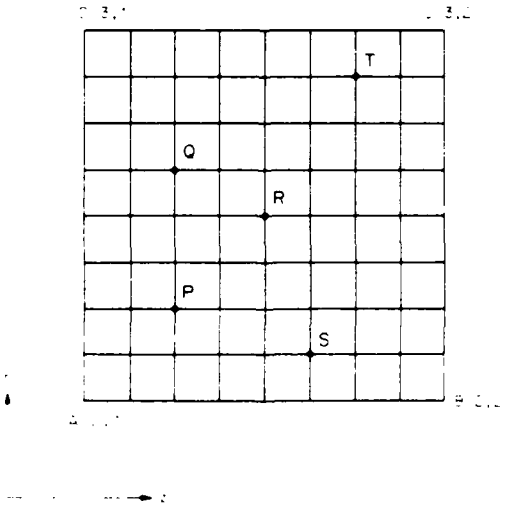

Fig. A1. The finite element grid for the sample problem.

Table A1 Comparison of analytical and numerical solution

Point	Analytical values			Computed values			% Difference		
	v_r	$-v_z$	ρ	v_r	$-v_z$	ρ	v_r	v_z	ρ
P	2.53125	1.40625	0.34124	2.53077	1.43358	0.342852	0.019	1.944	0.472
Q	3.44531	1.64063	0.35435	3.4588	1.68613	0.359417	0.391	2.774	1.432
R	3.125	1.8750	0.52250	3.11498	1.91764	0.52810	0.321	2.274	1.072
S	2.53125	1.82813	0.61077	2.50815	1.85314	0.618034	0.913	1.368	1.189
T	3.78125	2.57813	0.84585	3.76938	2.59881	0.838507	0.314	0.803	0.868

satisfy the balance of mass and the balance of linear momentum. Values of v_r and v_z as given by the presumed fields were assigned on the boundary faces BC, CD and DA of the domain shown in Fig. A1; those of v_r and σ_{zz} were prescribed on AB and values of ρ were prescribed on AD and DC. Note that b_r and b_z would appear on the right-hand side of eqn (10.4) and their values, as given by eqn (A4), were input into the computer code. In Table A1 are compared the values of v_r, v_z and ρ as computed from expressions (A3) and the computer code with ε in eqn (10.5) set equal to 0.005. It took 10 iterations for the solution to converge. The maximum error in v_r, v_z or ρ at any of the node points was found to be less than 3.25%.

Offprint from
Computational Plasticity, Models, Software and Applications
Edited by D.R.J. Owen, E. Hinton and E. Oñate
Pineridge Press Ltd, Swansea, U.K. 1987.

EFFECT OF NOSE SHAPE AND STRAIN-HARDENING ON STEADY STATE PENETRATION OF VISCOPLASTIC TARGETS *

R. C. Batra
Department of Engineering Mechanics
University of Missouri-Rolla
Rolla, MO 65401-0249 U.S.A.

SUMMARY

Steady state penetration of viscoplastic targets by rigid cylindrical penetrators with an ellipsoidal nose has been studied by the finite element method. The target material is assumed to obey a generalized form of Von-Mises yield criterion to account for strain-rate and strain hardening dependence. The ratio of the major to minor axes of the ellipsoidal nose is varied so that the nose shape corresponds to essentially a flat surface, a hemisphere or an ellipsoid. Frictional forces at the contact surface are assumed to be negligible. Computed results show that the nose shape effects significantly the deformations of the target material in the vicinity of the penetrator/target interface, and the axial resisting force experienced by the penetrator is considerably higher for the blunt nose as compared to that for the ellipsoidal nose. The axial force depends rather weakly upon the speed of the penetrator for every nose shape.

INTRODUCTION

In an attempt to shed some light on the approximations made in simpler theories of Tat [1] and Alekseevski [2], Batra and Wright [3] gave a detailed numerical solution, obtained by the finite element method, to the following idealized axisymmetric penetration problem. They assumed that the penetrator is semi-infinite in length, the target is infinite with a semi-infinite hole, the rate of penetration and all flow fields are steady as seen by an observer situated on the penetrator nose, no shear stress can be transmitted across the target/penetrator interface, the penetrator nose is hemispherical, and the target material is rigid/perfectly plastic. This problem simulates the intermediate stages of the penetration process wherein the active target/penetrator interface is at least one or two penetrator diameters away from either tar-

*Work supported by ARO Contract DAAG 29-85-K-0238

Errata "Effect of Nose Shape and Strain-Hardening on Steady State Penetration of Viscoplastic Targets" by R.C. Batra

Page No.	Location	Printed	Should read
1	-1 13	Tat[1]	Tate [1]
4	-1 2	...in find a numerical...	...in finding a...
	-1 9	...the solutions may be..	...the solution may not be...
6	1 14	...the governing...	...The governing...
	-1 2	...r_n/r_o<1.0...of between...	...r_n/r_o>1.0...of θ between
7	-1 13	values of I...	value of I...
8	1 7	...r_{b/r_o}...	...r_n/r_o...
9	1 3	...various for a ...	...various quantities for a...
10	1 5-6	...rather than hemispherical...	...rather than blunt. As for a hemispherical...
	-1 10	...with that...	...with α that...

get face, the remaining penetrator is still much longer than several diameters and is traveling at a speed close to its striking velocity, and the target material is much softer than the material of the penetrator. Subsequently, Batra [4] studied the problem when the penetrator nose can be ellipsoidal and the target material viscoplastic. Herein we extend this work further and investigate also the influence of strain-hardening of the target material.

FORMULATION OF THE PROBLEM

We use cylindrical coordinate axes attached to the penetrator nose with the positive z-axis pointing into the target. Equations governing the steady state deformations of the target are

$$\text{div } \underline{v} = 0, \tag{1}$$

$$\text{div } \underline{\sigma} = \rho(\underline{v}\cdot\text{grad})\ \underline{v}\ . \tag{2}$$

Here $\underline{v}$ is the velocity of a target particle as seen by an observer situated on the penetrator nose and moving with it, ρ is the current mass density, $\underline{\sigma}$ is the Cauchy stress tensor, and div and grad denote, respectively, the divergence and gradient operators. Equation (1) expresses the balance of mass and equation (2) the balance of linear momentum in the absence of body forces. In equation (1) it has been assumed that the deformations of the target are isochoric.

We neglect the elastic deformations of the target and assume the following constitutive relations for its material.

$$\underline{\sigma} = -p\ \underline{1} + 2\mu(I,\psi)\ \underline{D},\ \text{if } \underline{D} \neq \underline{0}\ , \tag{3}$$

$$\text{tr}(\underline{s}^2) \leq \frac{2}{3}\ \sigma_o^2\ (1 + \frac{\psi}{\psi_o})^{2n}\ ,\ \text{if } \underline{D} = \underline{0}\ , \tag{4}$$

$$\underline{s} = \underline{\sigma} + p\ \underline{1}\ , \tag{5}$$

$$2\mu\ (I,\psi) = \frac{\sigma_o}{\sqrt{3}\ I}\ (1 + b\ I)^m\ (1 + \frac{\psi}{\psi_o})^n\ , \tag{6}$$

$$\frac{\dot{\psi}}{(1 + \psi/\psi_o)^n} = \text{tr}\ (\underline{\sigma}\underline{D})\ , \tag{7}$$

$$2I^2 = \text{tr}(\underline{D}^2) \tag{8}$$

$$2\underline{D} = \text{grad } \underline{v} + (\text{grad } \underline{v})^T\ . \tag{9}$$

Here p is the hydrostatic pressure that is not determined by the deformation history, $\underline{D}$ is the stretching tensor, σ_o is the yield stress in simple tension or compression, parameters b and m describe the strain-rate hardening of the material, a superimposed dot stands for material time derivative, and

parameters ψ_o and n characterize the strain hardening of the material. Equations (3), (5) and (6) imply that

$$(\tfrac{1}{2}\mathrm{tr}\ \underset{\sim}{s}^2)^{\frac{1}{2}} = \frac{1}{\sqrt{3}}\,\sigma_o\,(1 + bI)^m\,(1 + \psi/\psi_o)^n \qquad (10)$$

which may be viewed as generalized Von-Mises yield criterion when the flow stress (given by the right-hand side of (10)) at a material particle depends upon its strain-rate and work-hardening parameter ψ. Equation (7) describes the evolution of the work-hardening parameter ψ.

A constitutive relation similar to equation (3) has been used by Zienkiewicz et al. [5] who took

$$2\mu = [\sigma_o + (2I/\sqrt{3}\gamma)^{1/n}]/\sqrt{3}\ I\ , \qquad (11)$$

where γ and n are functions of the temperature. In their study of the penetration and perforation problem, Ravid and Bodner [6] postulated that

$$2\mu(I) = \sigma_o\,(1 + c\ \log_{10}\,(2I/\sqrt{3}))/\sqrt{3}\ I \qquad (12)$$

where c is a material constant and is set equal to zero for strain rates lower than unity. We note that where as the effect of work hardening is included in equation (6), it was not considered by Zienkiewicz et al. and Ravid and Bodner.

Equation (1) and equations obtained by substituting from equations (3), (6), (9) and (10) into (2) are the field equations which together with appropriate boundary conditions are to be solved for p and $\underset{\sim}{v}$. Before stating the boundary conditions, we introduce non-dimensional variables as follows:

$$\bar{\underset{\sim}{\sigma}} = \underset{\sim}{\sigma}/\sigma_o\ ,\ \bar{p} = p/\sigma_o\ ,\ \bar{\underset{\sim}{s}} = \underset{\sim}{s}/\sigma_o\ ,\ \bar{\underset{\sim}{v}} = \underset{\sim}{v}/v_o\ ,\ \bar{r} = r/r_o\ ,$$

$$\bar{z} = z/r_o\ ,\ \bar{b} = b\ v_o/r_o\ ,\ \alpha = \rho\ v^2/\sigma_o\ ,\ \bar{\psi} = \psi\ . \qquad (13)$$

Here v_o is the speed of the penetrator and r_o the radius of its cylindrical body.

The governing equations in terms of non-dimensional variables are

$$\mathrm{div}\ \underset{\sim}{v} = 0\ , \qquad (14)$$

$$\mathrm{div}\ \underset{\sim}{\sigma} = \alpha(\underset{\sim}{v}\cdot\mathrm{grad})\underset{\sim}{v}\ , \qquad (15)$$

$$\frac{\mathrm{tr}(\underset{\sim}{\sigma}\underset{\sim}{D})}{(1 + \psi/\psi_o)^n} = (\underset{\sim}{v}\cdot\mathrm{grad})\ \psi, \qquad (16)$$

where

$$\underset{\sim}{\sigma} = -p\ \underset{\sim}{1} + \frac{1}{\sqrt{3}\ I}\ (1 + bI)^m\,(1 + \psi/\psi_o)^n\ \underset{\sim}{D}\ , \qquad (17)$$

grad and div now stand for the gradient and divergence operators in non-dimensional variables and we have dropped the superimposed bars. Henceforth, unless stated otherwise, we will use non-dimensional variables only. We note that besides the ratio of the major to minor axes of the ellipsoidal nose of the penetrator, there are five non-dimensional numbers α, b, m, ψ_o and n. All of these characterize the target material and α is also proportional to the square of the penetrator speed.

For the boundary conditions we take

$$\underset{\sim}{t}\cdot(\underset{\approx}{\sigma}\underset{\sim}{n}) = 0 \ , \tag{18}$$

$$\underset{\sim}{v}\cdot\underset{\sim}{n} = 0 \ , \tag{19}$$

on the target/penetrator interface, and

$$|\underset{\sim}{v} + \underset{\sim}{e}| \to 0 \text{ as } (r^2 + z^2)^{\frac{1}{2}} \to \infty \ , \ z > -\infty \ , \tag{20}$$

$$|\underset{\approx}{\sigma}\underset{\sim}{n}| \to 0 \text{ as } z \to -\infty, \ r \geq r_o \ , \tag{21}$$

at points far away from the penetrator. In equations (18) - (21), $\underset{\sim}{n}$ and $\underset{\sim}{t}$ are, respectively, a unit normal and a unit tangent vector on the bounding surface, and $\underset{\sim}{e}$ is a unit vector along the positive z-axis. The boundary condition (18) asserts that the tangential traction on the target/penetrator interface is zero. This is justified since a thin layer of material at the interface either melts or is severely degraded by adiabatic shear. Equation (19) implies no interpenetration of the target material into the penetrator and vice versa and equation (20) states that the target material ahead of the penetrator back surface and far away from the penetrator appears to be moving with a uniform velocity. That target particles behind the nose and on the bounding face perpendicular to the axis of the penetrator are traction free is embodied in equation (21).

Note that the governing equations (14) - (17) are coupled and nonlinear in $\underset{\sim}{v}$ and ψ. Their solution, if there is one, under the boundary conditions (18) - (21) will depend, in general, upon the rate at which quantities in (20) and (21) decay to zero. For a prescribed rate of decay of quantities in equations (20) and (21), the solutions may be unique. Also equation (16) giving the evolution of the strain-hardening parameter ψ does not have any diffusive term in it. We will gloss over the rather difficult questions of existence and uniqueness and seek an approximate solution by the finite element method. We hope that this solution is meaningful for the physical problem at hand.

The first step in find a numerical solution of the problem is to approximate the infinite target region by a

finite region R shown in Fig. 1. Whether this region is sufficient or not can be determined by solving the problem for

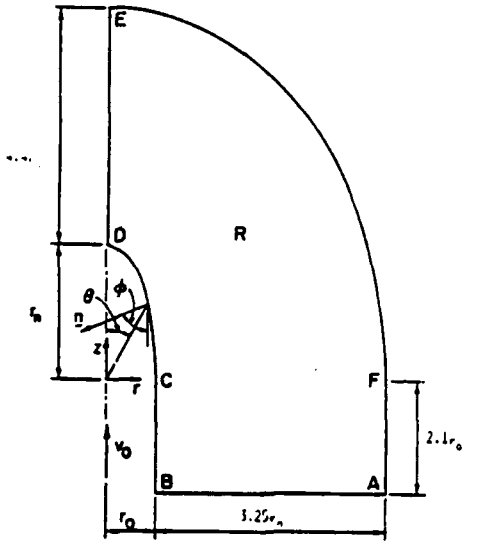

Fig. 1. The region to be studied.

two domains, one larger and containing the other, and ascertaining that the two sets of solutions essentially agree with each other at target points in the vicinity of the penetrator. The region shown in Fig. 1 was found to be adequate and has been used in results presented below. The boundary conditions (18) and (19) are taken to hold on the target/penetrator interface BCD. On other bounding surfaces following boundary conditions instead of equations (20) and (21) are applied

$$v_r = 0 \ , \ \sigma_{rz} = 0 \ , \text{ on the axis of symmetry DE} \ ,$$

$$v_z = -1.0 \ , \ v_r = 0 \ , \text{ on the bounding surface EFA} \ , \qquad (22)$$

$$v_r = 0 \ , \ \sigma_{zz} = 0 \ , \text{ on the bounding surface BA} \ .$$

COMPUTATION AND DISCUSSION OF RESULTS

In order to obtain an approximate solution of the problem, we first cast equations (14) - (17), (18), (19) and (22) into an equivalent weak form by using the Galerkin method. The reader is referred to the book by Becker et al. [7] and the paper by Zienkiewicz et al. [5] for details and to references [3,4] for a weak form of somewhat similar equations. The absence of a diffusive term in equation (16) necessitates the use of either a superfine mesh or a reasonable fine mesh with an artificial diffusive term added to the equation. Brooks and Hughes [8] have discussed in detail the justification for including such a term and have given equivalent ways of achieving the same objective. We added a diffusive term and

conducted numerical experiments with its coefficient δ. The two sets of values of p, v_r and v_z obtained with $\delta = 10^{-6}$ and 10^{-7} at nodes near the penetrator/target interface differed by less than one percent at each node. The results presented below are for $\delta = 10^{-6}$.

A finite element code employing six noded isoparametric triangular elements has been developed. The incompressibility constraint (14) and the boundary condition (19) on the target/penetrator interface are satisfied by using the method of Lagrange multipliers. On an element, a quadratic variation of the velocity field and a linear variation of the pressure field defined in terms of its values at the vertices are employed. Six quadrature points are used to evaluate various integrals numerically. the governing nonlinear equations are solved iteratively. The iterative process is stopped when, at each nodal point,

$$\|\underset{\sim}{v}^i - \underset{\sim}{v}^{i-1}\| + |\psi^i - \psi^{i-1}| \leq \epsilon(\|\underset{\sim}{v}^{i-1}\| + |\psi^{i-1}|) \ , \qquad (23)$$

where $\|\underset{\sim}{v}\|^2 = v_r^2 + v_z^2$, and ϵ is a preassigned small number. Values of p^i are not included in equation (23) since p appears linearly in the governing equations. The validity of the computer code has been established by solving a hypothetical problem that simulates the flow of an incompressible Navier-Stokes fluid in a circular pipe. The results for this sample problem are given in reference 3.

Values of various material parameters b, m, ψ_o, n and σ_o found from the experimental data in torsion of Costin et al. [9] are assumed to be valid under a more general state of stress studied herein. These and other parameters have been assigned the following values in the numerical results presented below.

$$n = .09 \ , \quad \psi_o = .017 \ , \quad b = 10^4 \ \text{sec}^{-1} \ , \quad m = .025$$
$$\rho = 7800 \ \text{kg/m}^3 \ , \quad \sigma_o = 180 \times 10^6 \ \text{Pa} \ , \quad \epsilon = 0.02 \ . \qquad (24)$$

All of the results stated below are in terms of non-dimensional variables.

Figure 2 depicts the effect of the nose shape on some of the variables. For a relatively blunt nose for which the ratio of the radius of the nose tip to that of the cylindrical portion of the penetrator is taken as 0.2, the normal pressure on the nose surface stays essentially constant and drops off sharply to zero near its periphery. The abcissa is the angular position θ in degrees. For $r_n/r_o \leq 1.0$, the normal pressure versus θ curve is concave downwards, it is concave upwards for $r_n/r_o < 1.0$ and for values of between 0 and 70 degrees. In every case the peak values of the normal pressure occurs for $\theta = 0°$ and the least value at $\theta = 90°$ where the

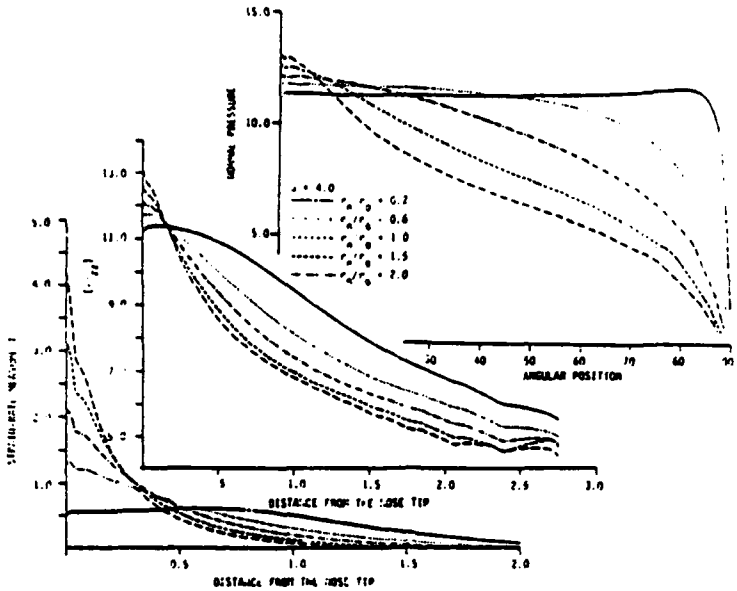

Figure 2. Effect of the ratio of the nose radius to the radius of the penetrator on the normal stress distribution at the penetrator nose and on the variation of $-\sigma_{zz}$ and I at points of the target along the axis ahead of the penetrator.

penetrator nose meets its cylindrical part. On the axial line ($r = 0$), the magnitude of the principal stress σ_{zz} decreases slowly with the distance from the nose tip for the blunt nose as compared to that for other values of r_n/r_o. The rate of decay of $(-\sigma_{zz})$ with the distance from the nose tip increases noticeably with the increase in the ratio r_n/r_o. Said differently, the deformations spread to a larger distance for a blunt nosed penetrator as compared to those for a penetrator with a sharp nose. This is also confirmed by the plot of the strain-rate measure I on the axial line. Note that the peak values of I increases markedly with the increase in the ratio r_n/r_o. However, with an increase in the ratio r_n/r_o, I drops off sharply with the distance from the nose tip. In all five cases studied, I essentially becomes zero at points distance $2r_o$ from the nose tip. Thus at these points nonzero values of σ_{zz} are due to the contribution from the hydrostatic pressure p. The dimensional values of I typically equal 10^5 times their non-dimensional values. Thus strain-rates of the order of $10^5 - 10^6$ sec^{-1} occur at points near the target/penetrator interface.

The non-dimensional axial resisting force F experienced by the rigid penetrator is given by

$$F = 2 \int_0^{\pi/2} (\underset{\sim}{n} \cdot \underset{\sim}{\sigma} \underset{\sim}{n}) \sin\theta \cos\phi \left[\sin^2\theta + \left(\frac{r_n}{r_o}\right)^2 \cos\theta\right]^{\frac{1}{2}} d\theta ,$$

where angles θ and ϕ are defined in Fig. 1. The corresponding axial force in physical units is given by $F(\pi r_o^2 \sigma_o)$. A curve fit by the method of least squares to the calculated values of F for different values of r_n/r_o gives

$$F = 19.536 \left(1 - .647 \frac{r_n}{r_o} + .1409 \left(\frac{r_n}{r_o}\right)^2\right) ,$$

$$\alpha = 4.0 , \quad b = 10^4 \text{ sec}^{-1} , \quad m = .025 , \quad n = .09 .$$

We note that an increase in the values of r_b/r_o from 0.2 to 2.0 results in more than three-fold decrease in the value of F.

The influence of the values of strain-hardening exponent n upon various quantities is shown in Fig. 3 for an ellipsoidal

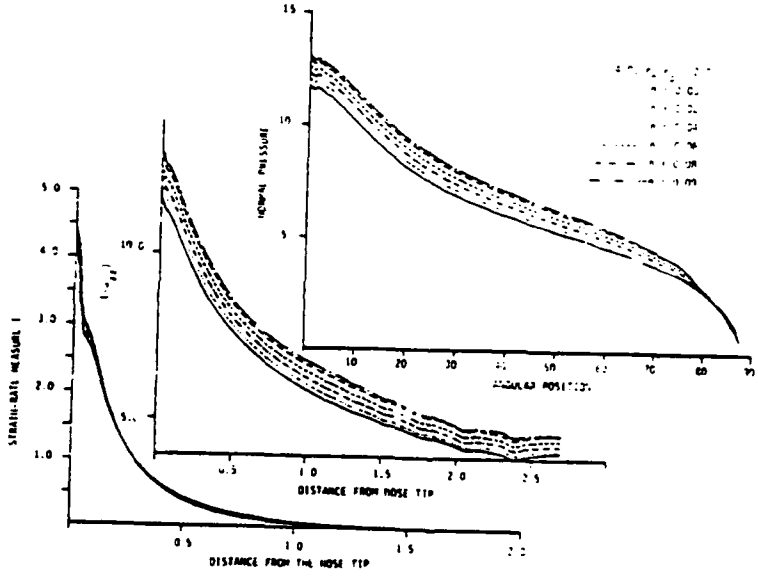

Figure 3. Effect of strain-hardening parameter on the normal stress distribution at the penetrator nose and on the variation of $-\sigma_{zz}$ and I at points of the target along the axis ahead of the penetrator.

nosed penetrator. The normal pressure on the penetrator nose increases with n and so does the magnitude of the principal stress σ_{zz} on the axial line. However, the values of strain-rate measure I at points on the axial line seem to be affected a little by the value of n. A curve fit to the computed values of the axial resisting force F gives

$$F = 4.525(1 + 1.793n) ,$$

$$\alpha = 4 , \quad r_n/r_o = 2 , \quad b = 10^4 \text{ sec}^{-1} , \quad m = 0.25 ,$$

implying thereby that F depends linearly upon n.

Results plotted in Fig. 4 illustrate the effect of the speed upon various for a blunt nose penetrator. Recall that

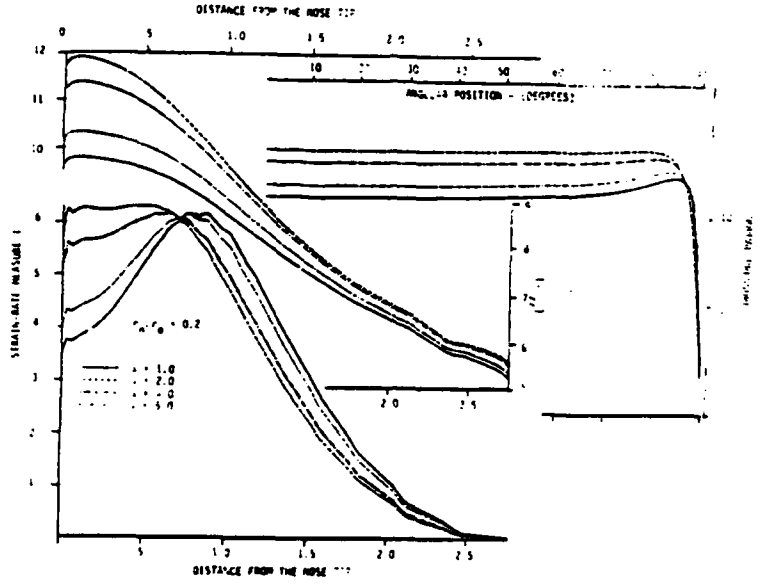

Figure 4. Effect of speed of the penetrator on the normal stress distribution at the penetrator nose and on the variation of $-\sigma_{zz}$ and I at points of the target along the axis ahead of the penetrator.

the non-dimensional number α is proportional to the square of the speed. The normal pressure on the penetrator nose increases with α. Note that for lower speeds, the normal pressure near the extremity of the penetrator nose increases before dropping off sharply to zero. For higher speeds this phenomenon is absent and the normal pressure is uniformly distributed on most of the nose surface and drops off rapidly near the edges. At a point on the axial line, the magnitude of the principal stress σ_{zz} increases with the speed. At lower speeds, the peak value of I at points on the axial line does not occur at the nose tip but at a point whose distance from the nose tip is nearly equal to the radius of the penetrator. At higher speeds, the strain-rate I becomes essentially constant over a distance equal to half the radius of the penetrator and then gradually drops off to zero. In either case I approaches zero at points on the axial line whose distance from the nose tip is 2.5 r_o or more. The dependence of the axial resisting force F upon α is given by

$$F = 14.641(1 + .04211\alpha) \ , \ r_n/r_o = .2 \ , \ b = 10^4 \ \text{sec}^{-1},$$

$$m = .025 \ , \ n = .09.$$

Thus F depends upon α rather weakly. This provides a justification for the assumption of the constant target resistance in the simple theory of Tate [1].

In Fig. 5 is plotted the effect of speed on target deformations when the penetrator nose is ellipsoidal rather than

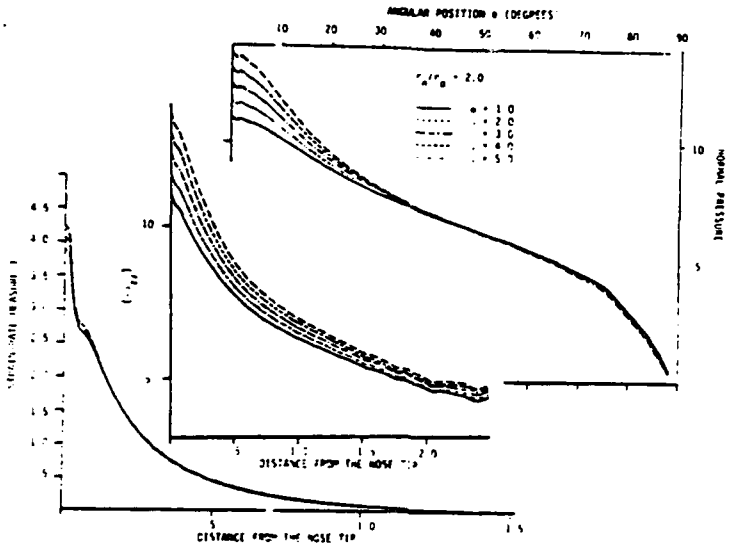

Figure 5. Effect of the penetrator speed on the normal stress distribution at the penetrator nose and on the variation of $-\sigma_{zz}$ and I at points of the target along the axis ahead of the penetrator.

hemispherical nosed penetrator in Ref. 3, the value of the normal pressure on the penetrator nose at θ equal to approximately forty-five degrees is unaffected by the penetrator speed. At points on the penetrator nose for which θ is less than 45°, the normal pressure increases with α and on the remainder of the surface, it decreases with α. However, the relative decrease is smaller than the percentage increase at points situated equal angular distance from the θ = 45° line. At a point on the axial line ahead of the penetrator, whereas the magnitude of σ_{zz} increases with that of I essentially remains unchanged except at a point on the nose tip where it increases slightly with α. The rate of decay of $(-\sigma_{zz})$ and I with the distance from the nose tip is essentially unchanged as the penetrator speed increases. Values of I essentially approach zero at points on the axial line whose distance from the penetrator nose tip is at least 1.5 r_o.

A curve fit to the computed values of the axial resistance force F at various values of α gives

$$F = 4.955(1 + .0151\alpha) ,$$

implying, as before, that F depends weakly upon α.

Figures 6 and 7 compare, respectively, the variation of I and ψ in the target region considered for two different nose shapes of the penetrator. When the penetrator nose is ellipsoidal, peak values of I occur at the nose tip and I decreases as one moves away from it in any direction. However, for a blunt nosed penetrator peak values of I occur at points on the target/penetrator interface where the nose meets the cylindrical portion of the penetrator. The peak value of I at any

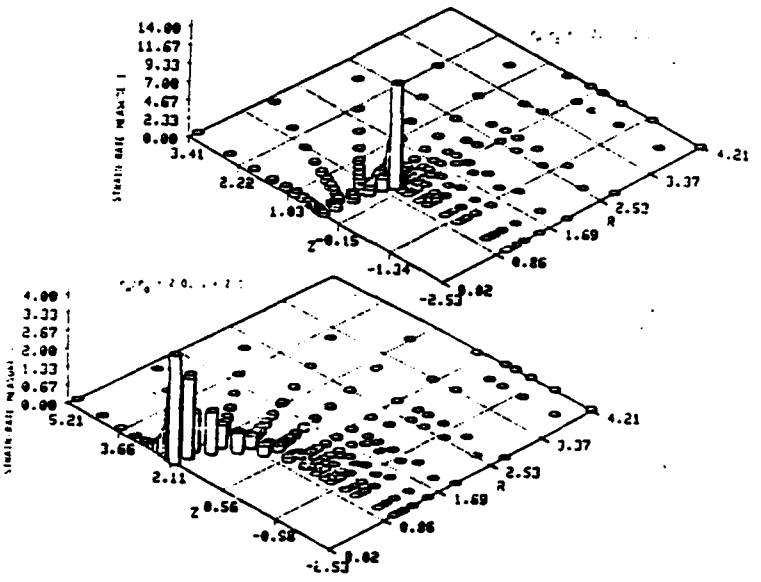

Figure 6. Comparison of the variation of the strain-rate measure I in the target region for an ellipsoidal nose and a blunt nose.

point in the target is nearly three times larger when the penetrator has a blunt nose as compared to that when it has a sharp ellipsoidal nose. The strain-hardening parameter exhibits a totally different behavior. For a blunt-nosed penetrator the peak value of ψ occurs at the nose tip and it drops off rather sharply as one moves away from it. It stays practically unchanged on most of the penetrator/target interface. For an ellipsoidal nosed penetrator the peak value of ψ does not occur at the nose tip but at a point on the penetrator/target interface which is on the penetrator nose and for which $\theta = 1°$. From this point on the value of ψ stays practically the same on the remainder of the target/penetrator interface. Again the peak value of ψ at any target point for a blunt nosed penetrator is roughly two and a half times as large as that for an ellipsoidal nosed penetrator. A possible

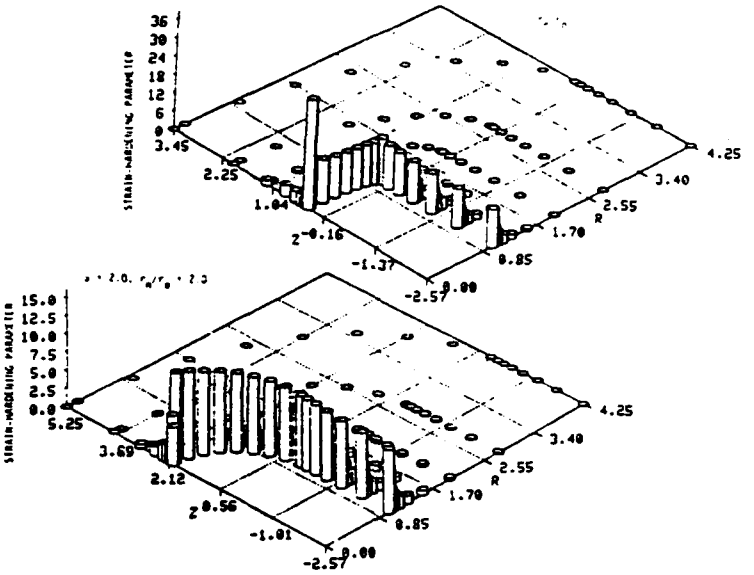

Figure 7. Comparison of the variation of the strain-hardening parameter ψ in the target region for an ellipsoidal nose and a blunt nose.

reason for the difference in the variations of ψ and I in the two cases is that the governing equation for ψ is convection dominated whereas that for I does have a natural diffusive term in it. As depicted in Fig. 6 of Ref. 3, the tangential velocity on the penetrator nose is quite different in the two cases. Whereas for a blunt nosed penetrator it increases from zero at first slowly and then quite rapidly when θ is close to 80°, for the ellipsoidal nosed penetrator it increases rapidly for $0 \leq \theta < 18°$ and gradually afterwards.

Finally we note that an extension of this work to the the thermo-mechanical problem when the target material can also thermally soften will appear in Ref. 10.

CONCLUSIONS

During the intermediate stages of penetration of a target all of whose dimensions are very large as compared to the penetrator radius and whose material is much softer as compared to that of the penetrator, the shape of the penetrator nose has most influence upon target deformations. For a blunt nosed penetrator the deformations spread to a larger distance away from the target/penetrator interface as compared to that for an ellipsoidal nosed penetrator. In every case the axial resisting force experienced by the penetrator depends weakly upon the penetrator speed. Also the deformation related field variables depend smoothly upon the strain hardening exponent. The peak values of strain-rate measure I and strain-hardening

parameter ψ are higher for a blunt nosed penetrator as compared to those for an ellipsoidal nosed penetrator. Points where these peak values occur are situated quite differently in the two cases.

ACKNOWLEDGEMENTS: The financial support of this work by the U.S. Army Research Office through Contract DAAG 29-85-K-0238 to the University of Missouri-Rolla is gratefully acknowledged. I thank Mr. Chang-Ho Kim for his help in plotting Figs. 6 and 7.

REFERENCES

1. TATE, A. - A Theory for the Deceleration of Long Rods after Impact. J. Mech. Phys. Solids, 15, p. 387, 1967.

2. ALEKSEEVSKI, V. P. - Penetration of a Rod into a Target at High Velocity. Combust. Expls. Shock Waves, 2, p. 63, 1966.

3. BATRA, R. C. and WRIGHT, T. W. - Steady State Penetration of Rigid Perfectly Plastic Targets. Int. J. Engng. Sci., 24, p. 41, 1986.

4. BATRA, R. C. - Steady State Penetration of Viscoplastic Targets. Int. J. Engng. Sci., 25, 1987 (to appear).

5. ZIENKIEWICZ, O. C., ONATE, E., and HEINRICH, J. C. - A General Formulation for Coupled Thermal Flow of Metals Using Finite Elements. Int. J. Num. Meth. Engng., 17, p. 1497, 1981.

6. RAVID, M. and BODNER, S. R - Dynamic Perforation of Viscoplastic Plates by Rigid Projectiles. Int. J. Engng. Sci., 21, p. 577, 1983.

7. BECKER, E., CAREY, G. and ODEN, J. T. - Finite Element-An Introduction, Prentice Hall, Englewood Ciffs, NJ, 1981.

8. BROOKS, A. N. and HUGHES, T. J. R. - Streamline Upwind/ Petrov-Gelerkin Formulations for Convection Dominated Flows with Particular Emphasis on the Incompressible Navier-Stokes Equations. Comp. Meth. Appl. Mechs. Engr., 32, p. 199, 1982.

9. COSTIN, L. S., CRISMAN, E. E., HAWLEY, R. H. and DUFFY, J. - On the Localization of Plastic Flow in Mild Steel Tubes under Dynamic Torsional Loading. Inst. Phys. Conf. Ser. No. 47, p. 90, 1979.

10. BATRA, R. C. - Steady State Penetration of Thermoviscoplastic Targets. Computational Mechanics - An Int. J., 2, 1987 (to appear).

Computational Mechanics (1988) 3, 1–12

Computational Mechanics

© Springer-Verlag 1988

Steady state penetration of thermoviscoplastic targets

R. C. Batra
Department of Engineering Mechanics, University of Missouri-Rolla, Rolla, MO 65401-0249, USA

Abstract. Steady state thermomechanical deformations of a target hit by a rigid cylindrical penetrator with an ellipsoidal nose are studied. The material of the target is assumed to be thermally softening but strain and strain-rate hardening. Results computed and presented graphically include the pressure distribution on the nose of the penetrator, dependence of the axial resisting force upon the speed of the penetrator, and the variation of field quantities such as the temperature and strain-rate in the target. Computed results show that the ratio of the major to minor axes of the ellipsoidal nose has a significant effect on the deformations of the target particles in the vicinity of the penetrator nose.

1 Introduction

In an attempt to shed some light on the validity of the approximations made in simple theories of penetration due to Alekseevskii (1966) and Tate (1967, 1969), Batra and Wright (1986) studied in detail the penetration problem that simulates the following situation. Suppose that the penetrator is in the intermediate stages of penetration so that the active target/penetrator interface is at least one or two penetrator diameters away from either target face, and the remaining penetrator is much longer than several diameters and is still traveling at a uniform speed. Thus steady state deformations of the target, presumed to be made of a rigid/perfectly plastic material, and being penetrated by a long cylindrical rigid rod with a hemispherical nose were analysed. Subsequently Batra (1987) showed that the axial resisting force experienced by the rigid penetrator is considerably reduced if its nose shape is ellipsoidal rather than hemispherical and also investigated the effect of the dependence of the flow stress upon the strain-rate. Herein we study the steady state penetration problem when the target material is thermally softening but strain and strain-rate hardening.

Pidsley (1984) has recently given a detailed numerical solution of the penetration problem in which both materials are considered to be deformable and rigid/perfectly plastic. We refer the reader to his paper for more references on this subject. Even though we study a somewhat simpler situation, our material model is more general in that we account for the effect of strain and strain-rate hardening and thermal softening. We note that the peak strains and strain-rates encountered during steady state deformations of the target are of the order of 10 and 10^5 sec^{-1} respectively. Also the temperature at target points may rise to as much as half of the melting point of the target material. We study the effect of these competing factors as well as of the penetrator speed and the shape of its nose on the deformations of the target.

2 Formulation of the problem

Since the axisymmetric deformations of the target appear to be independent of time to an observer situated on the penetrator nose and moving with it, we choose a cylindrical co-ordinate system attached to the nose tip with the positive z-axis pointing into the target material. With respect to these axes translating with a uniform velocity $v_0 e$, e being a unit vector along the penetrator axis

and in the direction of its motion, equations governing the thermomechanical deformations of the target are

$$\operatorname{div} \boldsymbol{v} = 0, \tag{1}$$

$$\operatorname{div} \boldsymbol{\sigma} = \varrho (\boldsymbol{v} \cdot \operatorname{grad}) \boldsymbol{v}, \tag{2}$$

$$-\operatorname{div} \boldsymbol{q} + \operatorname{tr}(\boldsymbol{\sigma} \mathbf{D}) = \varrho (\boldsymbol{v} \cdot \operatorname{grad}) U, \tag{3}$$

$$\operatorname{tr}(\boldsymbol{\sigma} \mathbf{D}) = (\boldsymbol{v} \cdot \operatorname{grad}) \varkappa, \tag{4}$$

$$\mathbf{D} = (\operatorname{grad} \boldsymbol{v} + (\operatorname{grad} \boldsymbol{v})^{T})/2 . \tag{5}$$

Equations (1) through (4) written in Eulerian description of motion express respectively the balance of mass, linear momentum, internal energy and the evolution of the work hardening parameter $\varkappa$. In Eq. (4) we have neglected the elastic deformations of the target and in Eq. (3) assumed that all of the plastic working, rather than a part of it (e.g. Farren and Taylor 1925) is dissipated in the form of heat. The operators grad and div signify the gradient and divergence operators on fields defined in the present configuration. Furthermore, $\boldsymbol{\sigma}$ is the Cauchy stress tensor, ϱ is the mass density of the target material, $\boldsymbol{v}$ is the velocity of the target particle relative to the penetrator, $\boldsymbol{q}$ is the heat flux per unit present area, $\mathbf{D}$ is the strain-rate tensor, and U the specific internal energy. Equations (1) through (4) are to be supplemented by constitutive relations and boundary conditions.

We assume the following constitutive relations for the target material.

$$\boldsymbol{q} = -k \operatorname{grad} \theta , \tag{6}$$

$$U = c\theta , \tag{7}$$

$$\boldsymbol{\sigma} = -p\mathbf{1} + 2\mu(I, \theta, \psi)\mathbf{D}, \quad \text{if } \mathbf{D} \neq \mathbf{0}, \tag{8}$$

$$\operatorname{tr}(\mathbf{s}^2) \leq \frac{2}{3}\sigma_0^2 (1 - a\theta)^2 \left(1 + \frac{\psi}{\psi_0}\right)^{2n}, \quad \text{if } \mathbf{D} = \mathbf{0}, \tag{9}$$

$$\mathbf{s} = \boldsymbol{\sigma} + p\mathbf{1}, \tag{10}$$

$$2\mu(I, \theta, \psi) = \frac{\sigma_0}{\sqrt{3}I}(1 + bI)^m (1 - a\theta)\left(1 + \frac{\psi}{\psi_0}\right)^n, \tag{11}$$

$$\dot{\varkappa}(\psi) = \sigma_0 \dot{\psi} (1 + \psi/\psi_0)^n, \tag{12}$$

$$I^2 = \tfrac{1}{2} \operatorname{tr}(\mathbf{D}^2) . \tag{13}$$

Equation (6) is Fourier's law of heat conduction, k is the thermal conductivity, θ is the change in the temperature of a material particle from that in the underformed configuration, c is the specific heat which is assumed to be constant, p is the hydrostatic pressure not determined by the deformation history, and σ_0 is the yield stress in a simple tension or compression test. The material parameters b and m describe the strain-rate sensitivity of the material, the material parameter a describes its thermal softening, and ψ_0 and n characterize the strain hardening of the material. An integral form of Eq. (12) with $\varkappa$ interpreted as the true stress and ψ the plastic strain represents the stress-strain curve in a quasistatic reference test. Equation (8) may be interpreted as a constitutive relation for a Non-Newtonian fluid whose viscosity μ depends upon the strain-rate, temperature and a material parameter ψ. Equation (8) implies that

$$\left(\frac{1}{2}\operatorname{tr}\mathbf{s}^2\right)^{\frac{1}{2}} = \frac{1}{\sqrt{3}}\sigma_0 (1 + bI)^m (1 - a\theta)\left(1 + \frac{\psi}{\psi_0}\right)^n \tag{14}$$

which can be viewed as a generalized Von-Mises yield criterion when the flow stress (given by the right-and side of (14)) at a material particle depends upon its strain-rate, strain and temperature. A constitutive relation similar to Eq. (8) has been used by Zienkiewicz et al. (1981) who took

$$2\mu = [\sigma_0 + (2I/\sqrt{3}\gamma)^{1/n}]/\sqrt{3}I, \tag{15}$$

where γ and n are functions of θ. They asserted that it represents Perzyna's viscoplastic model. For a simple shearing deformation, Litonski (1959) proposed that

$$\tau = c(1 - a\theta)(1 + b\gamma)^m \dot{\gamma}^n \tag{16}$$

where τ and γ equal the shear stress and shear strain, and c is a material constant. Note that this relation implies that τ is zero whenever $\dot{\gamma} = 0$. Another stress-strain law proposed by Lindholm and Johnson (1984), based on fitting curves to experimental data obtained from torsion tests, is

$$\tau = (A + B\gamma^n)(1 + C \ln(\dot{\gamma}/\dot{\gamma}_0)) \frac{\theta_m - \theta}{\theta_m - \theta_0} \tag{17}$$

where θ_m is the melting point of the material, θ_0 is a reference temperature, and A, B and C are material constants. Lin and Wagoner (1986) recently reported that the following curve

$$\sigma = 556\,(\varepsilon - 0.014)^{0.219}(\dot{\varepsilon}/0.02)^{0.018}(1 - 0.0012\,(\theta - 298))\,\text{MPa}\,, \tag{18}$$

fitted well their experimental data derived from a uniaxial tension test on Armco I.F. steel. In Eq. (18), σ and ε are the axial stress and the axial strain respectively and θ is in °K. The linear dependence of the flow stress upon temperature has also been observed by Bell (1968).

The constitutive relation (8) with μ given by Eq. (11) is an attempt to generalize the one used by Wright and Batra (1986) for simple shearing deformations of nonpolar and dipolar materials. They used it to study shear strain localization phenomenon in metals and derived it by using arguments similar to those employed by Green, McInnis and Naghdi (1968). A curve fit to the torsion test data of Costin et al. (1979) for a 1018 cold rolled steel gives $n = 0.09$, $\varphi_0 = 0.017$, $b = 10^4\ \text{sec}^{-1}$ and $m = 0.025$.

Before stating the boundary conditions we non-dimensionalize the variables as follows.

$$\bar{\boldsymbol{\sigma}} = \boldsymbol{\sigma}/\sigma_0, \quad \bar{p} = p/\sigma_0, \quad \bar{\mathbf{s}} = \mathbf{s}/\sigma_0, \quad \bar{v} = v/v_0, \quad \bar{r} = r/r_0, \quad \bar{z} = z/r_0, \quad \bar{\theta} = \theta/\theta_0\,,$$
$$\bar{b} = b\frac{v_0}{r_0}, \quad \bar{a} = a\theta_0, \quad \alpha = \varrho v_0^2/\sigma_0, \quad \beta = k/(\varrho c v_0 r_0), \quad \theta_0 = \sigma_0/(\varrho c)\,. \tag{19}$$

Substituting from Eqs. (6) through (12) into the balance laws (1) through (4), rewriting these in terms of non-dimensional variables, and denoting the gradient and ~~and~~ divergence operators in non-dimensional coordinates by grad and div, we arrive at the following set of equations.

$$\operatorname{div} \boldsymbol{v} = 0, \tag{20}$$

$$\operatorname{div} \boldsymbol{\sigma} = \alpha(\boldsymbol{v} \cdot \operatorname{grad})\boldsymbol{v}, \tag{21}$$

$$\operatorname{tr}(\boldsymbol{\sigma}\mathbf{D}) + \beta \operatorname{div}(\operatorname{grad}\theta) = (\boldsymbol{v} \cdot \operatorname{grad})\theta\,, \tag{22}$$

$$\frac{\operatorname{tr}(\boldsymbol{\sigma}\mathbf{D})}{(1 + \varphi/\varphi_0)^n} = (\boldsymbol{v} \cdot \operatorname{grad})\varphi, \tag{23}$$

where

$$\boldsymbol{\sigma} = -p\mathbf{1} + \frac{1}{\sqrt{3I}}(1 + bI)^m(1 - a\theta)\left(1 + \frac{\varphi}{\varphi_0}\right)^n \mathbf{D}, \tag{24}$$

and we have dropped the superimposed bars.

We assume smooth contact at the target/penetrator interface. Thus the boundary conditions on this surface are

$$\boldsymbol{t} \cdot (\boldsymbol{\sigma}\boldsymbol{n}) = 0\,, \tag{25.1}$$

$$\boldsymbol{v} \cdot \boldsymbol{n} = 0\,, \tag{25.2}$$

$$\boldsymbol{q} \cdot \boldsymbol{n} = h(\theta - \theta_a)\,, \tag{25.3}$$

where h is the heat transfer coefficient between the penetrator and the target, θ_a is an average

temperature of the penetrator, and n and t are, respectively, a unit normal and a unit tangent vector to the surface. At points far away from the penetrator

$$|v + e| \to 0, \quad \theta \to 0, \quad \psi \to 0 \quad \text{as} \quad (r^2 + z^2)^{\frac{1}{2}} \to \infty, \quad z > -\infty, \tag{26.1}$$

$$|\sigma n| \to 0, \quad |q \cdot n| \to 0, \quad \psi \to 0 \quad \text{as} \quad z \to -\infty, \quad r \geq r_0. \tag{26.2}$$

The boundary condition (26.1) states that target particles at a large distance from the penetrator appear to be moving at a uniform velocity with respect to it and experience no change in their temperature. Equation (26.2) implies that far to the rear the traction and heat flux fields vanish.

Note that the governing Eqs. (20)–(23) are coupled and are nonlinear in v, θ and ψ. Their solution, if there is one, may not be unique and will depend, in general, upon the rates at which quantities in (26) decay to zero. Since we are unable to solve these equations analytically and prove any uniqueness theorem, we will seek a numerical solution of these equations which we hope will be physically meaningful.

3 Finite element formulation of the problem

The numerical solution of the problem necessitates the consideration of a finite region. Since the target deformations are axisymmetric, only the target region R shown in Fig. 1 is studied. The adequacy of the finite domain considered will be verified by solving the problem for two separate regions, one larger and containing the other, and ensuring that the two sets of computed values of various field quantities are close to each other. The boundary conditions (26) are replaced by the following.

$$\sigma_{zz} = 0, \quad v_r = 0, \quad \frac{\partial \theta}{\partial z} = 0 \quad \text{on the surface } AB, \tag{27.1}$$

$$\sigma_{rz} = 0, \quad v_r = 0, \quad \frac{\partial \theta}{\partial r} = 0 \quad \text{on the axis of symmetry } DE, \tag{27.2}$$

$$v_r = 0, \quad v_z = -1.0, \quad \theta = 0, \quad \psi = 0 \quad \text{on the boundary surface } EFA. \tag{27.3}$$

Referring the reader to Becker et al. (1981) and Zienkiewicz et al. (1981) for details, we simply note that a weak formulation of the problem defined on the region R by Eqs. (20)–(24) and boundary conditions (25) and (27) is that equations

$$\int_R \lambda (\operatorname{div} v)\, dv = 0, \tag{28.1}$$

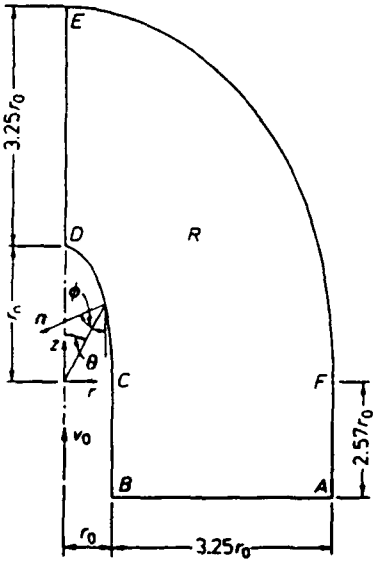

Fig. 1. The finite region studied

$$\int_R p(\operatorname{div}\boldsymbol{\varphi})\,dv - \int_R \mu(I,\theta,\psi)(\mathbf{D}:(\operatorname{grad}\boldsymbol{\varphi} + (\operatorname{grad}\boldsymbol{\varphi})^T))\,dv = \alpha\int_R ((\boldsymbol{v}\cdot\operatorname{grad})\boldsymbol{v})\cdot\boldsymbol{\varphi}\,dv, \tag{28.2}$$

$$\int_R ((\boldsymbol{v}\cdot\operatorname{grad})\theta)\eta\,dv + \beta\int_R \operatorname{grad}\theta\cdot\operatorname{grad}\eta\,dv + h\int_{\partial_1 R}\theta\eta\,dA = \int_R \eta(\boldsymbol{\sigma}:\mathbf{D})\,dv - \int_{\partial_1 R} h\theta_a\eta\,dA, \tag{28.3}$$

$$\int_R ((\boldsymbol{v}\cdot\operatorname{grad})\psi)\xi\,dv = \int_R \frac{(\boldsymbol{\sigma}:\mathbf{D})}{\left(1+\dfrac{\psi}{\psi_0}\right)^n}\,\xi\,dv, \tag{28.4}$$

hold for arbitrary smooth functions λ, φ, η and ξ defined on R such that $\varphi_r = 0$ on AB, $\varphi = 0$ on EFA, $\boldsymbol{\varphi}\cdot\boldsymbol{n} = 0$ on the target/penetrator interface BCD, and $\eta = \xi = 0$ on EFA. In these equations, $\mathbf{A}:\mathbf{B} = \operatorname{tr}(\mathbf{A}\mathbf{B}^T)$ for linear transformations $\mathbf{A}$ and $\mathbf{B}$, and $\partial_1 R$ denotes the target/penetrator interface BCD. Since these equations are nonlinear in $\boldsymbol{v}$, θ and ψ, the following iterative technique has been employed. At the i^{th} iteration, equations

$$\int_R \lambda\operatorname{div}\boldsymbol{v}^i\,dv = 0, \tag{29.1}$$

$$\int_R p^i(\operatorname{div}\boldsymbol{\varphi})\,dv = \int_R \mu(I^{i-1},\theta^{i-1},\psi^{i-1})(\mathbf{D}^i:(\operatorname{grad}\boldsymbol{\varphi} + (\operatorname{grad}\boldsymbol{\varphi})^T))\,dv = \alpha\int_R ((\boldsymbol{v}^{i-1}\cdot\operatorname{grad})\boldsymbol{v}^i)\cdot\boldsymbol{\varphi}\,dv, \tag{29.2}$$

$$\int_R ((\boldsymbol{v}^{i-1}\cdot\operatorname{grad})\theta^i)\eta\,dv + \beta\int_R \operatorname{grad}\theta^i\cdot\operatorname{grad}\eta\,dv + h\int_{\partial_1 R}\theta^i\eta\,dA = \int_R \eta(\boldsymbol{\sigma}^{i-1}:\mathbf{D}^{i-1})\,dv - \int_{\partial_1 R} h\theta_a\eta\,dA, \tag{29.3}$$

$$\int_R ((\boldsymbol{v}^{i-1}\cdot\operatorname{grad})\psi^i)\xi\,dv = \int_R \frac{\boldsymbol{\sigma}^{i-1}:\mathbf{D}^{i-1}}{\left(1+\dfrac{\psi^{i-1}}{\psi_0}\right)^n}\,\xi\,dv, \tag{29.4}$$

are solved for $\boldsymbol{v}^i$, θ^i, ψ^i and p^i. The iterative process is stopped when, at each nodal point,

$$\|\boldsymbol{v}^i - \boldsymbol{v}^{i-1}\| + |\theta^i - \theta^{i-1}| + |\psi^i - \psi^{i-1}| \le \varepsilon[\|\boldsymbol{v}^{i-1}\| + |\theta^{i-1}| + |\psi^{i-1}|] \tag{30}$$

where $\|\boldsymbol{v}\|^2 = v_r^2 + v_z^2$, and ε is a preassigned small number. Values of p^i are not included in Eq. (30) since p appears linearly in Eq. (29.2).

4 Computation and discussion of results

The finite element code developed earlier [Batra and Wright (1986)] to solve the problem when the target material is modeled as rigid/perfectly plastic and the penetrator nose is hemispherical has been modified to solve the present problem. It employes six-noded triangular elements with v_r, v_z, ψ and θ approximated by quadratic functions over an element and p by a linear function defined in terms of its values at the vertices of the triangular element. The validity of the code was established by first modifying Eqs. (29) to include arbitrary source terms on their right-hand sides, and then solving simple problems for incompressible Navier-Stokes-Fourier fluids. The source terms were adjusted so that the governing equations were satisfied by the presumed analytic expressions for v_r, v_θ, p, θ and ψ. Results for a sample problem that does not include thermal effects are given in Batra and Wright (1986).

A major difference between the problem studied herein and those studied earlier by Batra and Wright (1986) and Batra (1987) is that Eq. (28.4) does not have any diffusive term in it. This necessitates the use of either an ultrafine mesh or a fine mesh with an artificial diffusive term included in Eq. (28.4). Brooks and Hughes (1982) have discussed in detail the justification for including such a term and have given equivalent ways of achieving the same objective. We added a term $\delta\int_R \operatorname{grad}\psi\cdot\operatorname{grad}\xi\,dv$ to the left-hand side of Eq. (28.4) and computed results for $\delta = 10^{-6}$ and 10^{-7}. The two sets of values of θ, p, v_r and v_z differed by less than one percent at each node. The results presented below are for $\delta = 10^{-6}$. We next ascertained the adequacy of the region considered by increasing DE in Fig. 1 from $3.25r_0$ to $4.5r_0$. Again the difference in the values of θ, p, v_r, v_z and ψ at points in the vicinity of the penetrator nose was negligible.

We note that experimental data for the range of deformations expected to occur in the penetration problem under study is not available in the open literature. Therefore, values of material parameters b, m, a, φ_0 and n in Eq. (14) found by fitting a curve to the experimental data in torsion of Costin et al. (1979) were assumed to be valid under the more general state of stress studied here. This should enable us to undertake the parametric study for a reasonable range of values of various material parameters. The values of various parameters used to compute numerical results are:

$n = 0.09$, $\varphi_0 = 0.017$, $b = 10^4$ sec, $m = 0.025$, $a = 0.000555/°C$, $k = 48$ W/m °C, $c = 473$ J/kg °C, $\varrho = 7800$ kg/m^3, $\sigma_0 = 180 \times 10^6$ Pa, $h = 20$ W/m^2 °C, $r_0 = 2.54$ mm, $\varepsilon = 0.02$, $\theta_a = 0$.

However, the results presented below are in terms of non-dimensional quantities and the variables that are assigned values different from those given above are so indicated in the figures along with their new values.

In Fig. 2 is plotted the pressure distribution on the penetrator nose for a relatively blunt nose ($r_n/r_0 = 0.2$), a hemispherical nose ($r_n/r_0 = 1$) and an ellipsoidal nose ($r_n/r_0 = 2.0$). As expected the normal pressure on the blunt nose stays essentially uniform over most of its surface and drops off sharply near its extremities. Note the change in the curvature of the pressure curve in going from hemispherical to an ellipsoidal nose. The non-dimensional axial resisting force decreased from 17.091 for the blunt nose to 8.902 for the hemispherical nose and further to 5.085 for the ellipsoidal nose. The axial resisting force F is given by

$$F = 2\int_0^{\pi/2} (\boldsymbol{n}\cdot\boldsymbol{\sigma}\boldsymbol{n}) \sin\theta\cos\varphi \left[\sin^2\theta + \left(\frac{r_n}{r_0}\right)^2 \cos^2\theta\right]^{\frac{1}{2}} d\theta,$$

where angles θ and φ are defined in Fig. 1. The corresponding axial force in physical units is given by $F(\pi r_0^2 \sigma_0)$. The normal pressure on the hemispherical and the ellipsoidal nose surface for the

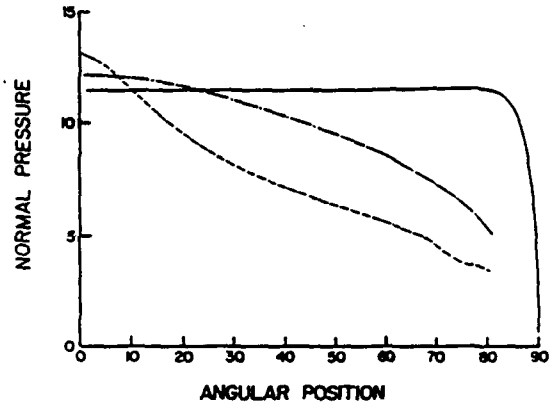

Fig. 2. Distribution of the normal pressure on the penetrator nose for three different nose shapes. —— Blunt nose ($r_n/r_0 = 0.2$); –·–·– hemispherical nose ($r_n/r_0 = 1.0$); ----- ellipsoidal nose ($r_n/r_0 = 2.0$)

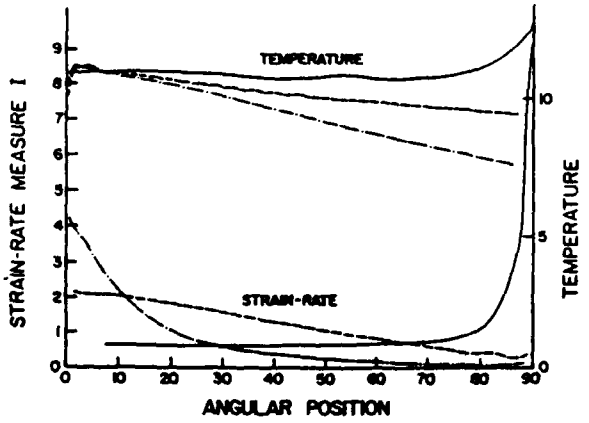

Fig. 3. Variation of the strain-rate measure I and the temperature change θ on the penetrator nose for three different nose shapes. —— Blunt nose ($r_n/r_0 = 0.2$); ----- hemispherical nose ($r_n/r_0 = 1.0$); –·–·– ellipsoidal nose ($r_n/r_0 = 2.0$); $\alpha = 4.0$

angle θ greater than nearly 75° is not plotted because of the difficulties encountered in computing it accurately. The mesh in this region was not fine enough to yield reliable values. Figure 3 depicts the variation of the strain-rate invariant I and temperature change θ on the nose surface. Whereas the maximum value 4.21 of I occurs at the penetrator nose tip for the ellipsoidal nose, it assumed very high values at the extremities for the blunt nose. For these two nose shapes significant values of I occur near the nose tip and the nose periphery respectively. For the hemispherical nose shape I decreases almost linearly from its maximum value of 2.16 at the nose tip to 0.4 at its periphery ($\theta = 90°$). The dimensional values of I equal 1.1 (10^5) times the non-dimensional values. The values of temperature at the nose tip do not depend that much on the nose shape. However the temperature decreases with θ for the ellipsoidal and the hemispherical nose, it increases with θ for the blunt nose. Because of the high-strain rates near the vicinity of the periphery of the blunt nose, there is a lot of heat generated in this narrow region. Since material particles near the periphery of the nose are moving relatively slowly, not much of the heat produced is convected or transported away. In Fig. 4 is plotted the variation of the strain rate I and temperature change θ on the axial line. For the blunt nose, the deformation has spread to a larger distance as compared to that for the ellipsoidal nose. Accordingly the temperature drops off slowly for the blunt nose than it does for the other two cases. The actual temperatures in °C are obtained by multiplying their non-dimensional values by 48.9. Thus temperatures as high as 605°C occur at and near the nose tip. The maximum value of strain-rate I on the axial line appears to occur at a point slightly away from the nose tip. This initial rise is probably only an artifact and the curves should be extended smoothly to the nose-tip.

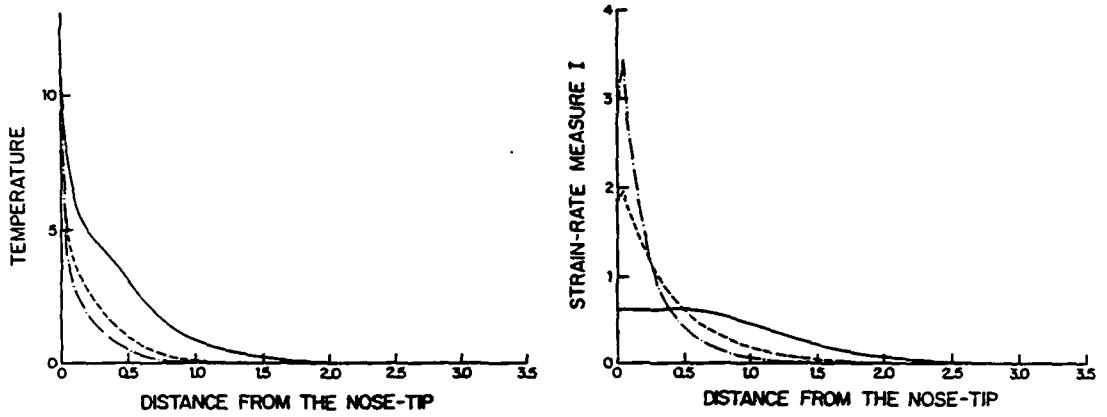

Fig. 4. Variation of the temperature change and strain-rate measure I on the axial line for three different nose shapes. —— Blunt nose ($r_n/r_0 = 0.2$); - - - - - hemispherical nose ($r_n/r_0 = 1.0$); —·—·— ellipsoidal nose ($r_n/r_0 = 2.0$); $\alpha = 4.0$

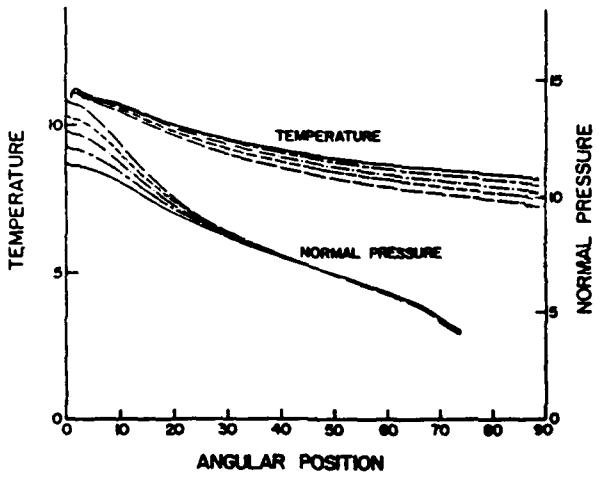

Fig. 5. Pressure and temperature distribution on the ellipsoidal penetrator nose for different values of α. —— $\alpha = 1.0$; - - - - - $\alpha = 2.0$; —·—·— $\alpha = 3.0$; - - - - - $\alpha = 4.0$; — — — $\alpha = 5.0$

Figures 5 and 6 illustrate the effect of speed of the penetrator on various solution parameters at or in the vicinity of its ellipsoidal nose with $r_n/r_0 = 2.0$. As shown in Fig. 5, the normal pressure near the penetrator nose tip increases with the speed but decreases near its periphery. Near $\vartheta = 45°$, the speed has no effect on the normal pressure. Such a behavior was also observed for a hemispherical nose and a rigid/perfectly plastic target material by Batra and Wright (1986). The dependence of the non-dimensional axial force F upon the speed (through non-dimensional variable α) is given by

$F = 5.021 + 0.0732\alpha$, ellipsoidal nose ($r_n/r_0 = 2.0$)

$F = 8.71 + 0.2145\alpha$, hemispherical nose.

For rigid/perfectly plastic materials, Batra and Wright (1986) obtained $F = 3.903 + 0.0773\alpha$ for a hemispherical nosed penetrator, and Batra (1987) computed $F = 2.58 + 0.019\alpha$ for a penetrator with an ellipsoidal nose having $r_n/r_0 = 2.0$. Thus the consideration of strain and strain-rate hardening and thermal softening effects more than doubles the axial resisting force. In every case studied so far, F depends upon α weakly. This weak dependence of F upon α seems to explain why the choice of constant target resistance in the simple theory of Tate (1967, 69) gives such good qualitative results. On most of the nose surface, the temperature decreases with α. This is shown in Fig. 5. Figure 6 depicts that most of the target deformations are concentrated near the penetrator nose. The peak value of I on the axial line appears to occur not at the nose tip but slightly away from it. The plots of strain-rate invariant I and the temperature change in the target region, shown in Fig. 7, confirm that significant target deformations occur in the vicinity of the target/penetrator interface.

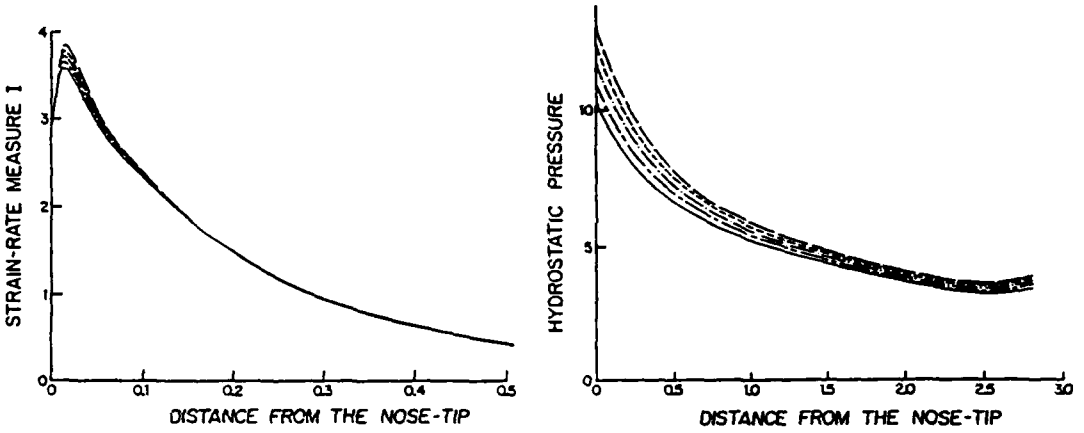

Fig. 6. Variation of the hydrostatic pressure and the strain-rate mesure I on the axial line for different values of α. Explanations see Fig. 5

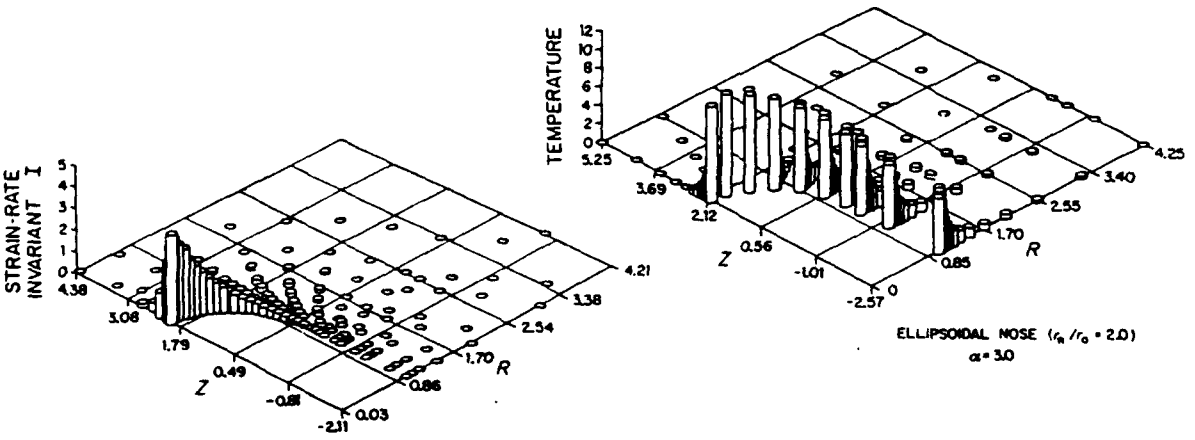

Fig. 7. Temperature and strain-rate distribution in the target region for $\alpha = 3.0$.

How different material parameters influence the deformations of the target is demonstrated by results presented in Figs. 8 through 11. Figure 8 shows that strain-rate hardening increases the normal pressure more than the work-hardening does. The inclusion of thermal softening affects little, if any, the normal pressure distribution on the penetrator nose. Near the nose tip (Fig. 9) the inclusion of work-hardening and strain-rate hardening decreases the value of the strain-rate invariant I but increases the temperature. This is due to the fact that these hardening effects increase the material's flow stress and cause more plastic working which is converted into heat. The thermal softening has a noticeable effect on the temperature distribution at the penetrator nose. From the plot of the strain-hardening parameter ψ on the penetrator nose and on the axial line in Fig. 10,

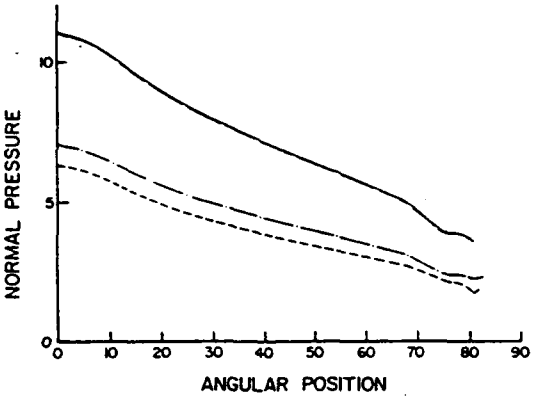

Fig. 8. Effect of different material parameters on the pressure distribution at the penetrator nose ($r_a/r_0 = 2.0$; $\alpha = 1.0$; —— full model; - - - no thermal softening; -·-·- strain hardening only; ····· rigid perfectly plastic)

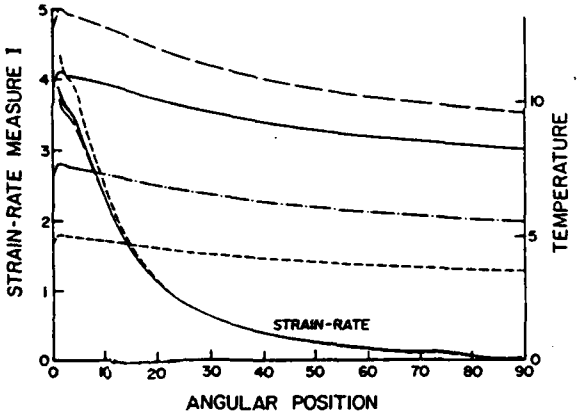

Fig. 9. Effect of different material parameters on the temperature and strain-rate distribution at the penetrator nose ($r_a/r_0 = 2.0$). Explanations see Fig. 8

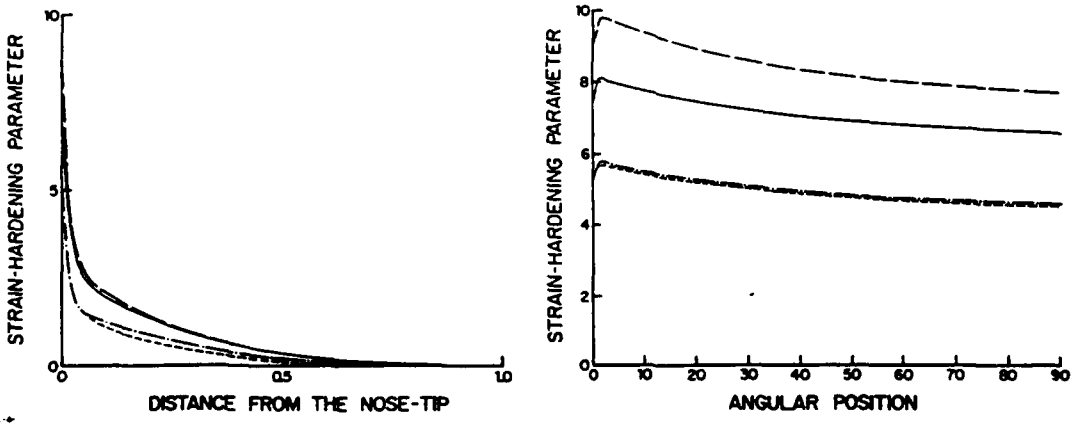

Fig. 10. Effect of different material parameters on the strain-hardening parameter ψ. Explanations see Fig. 8

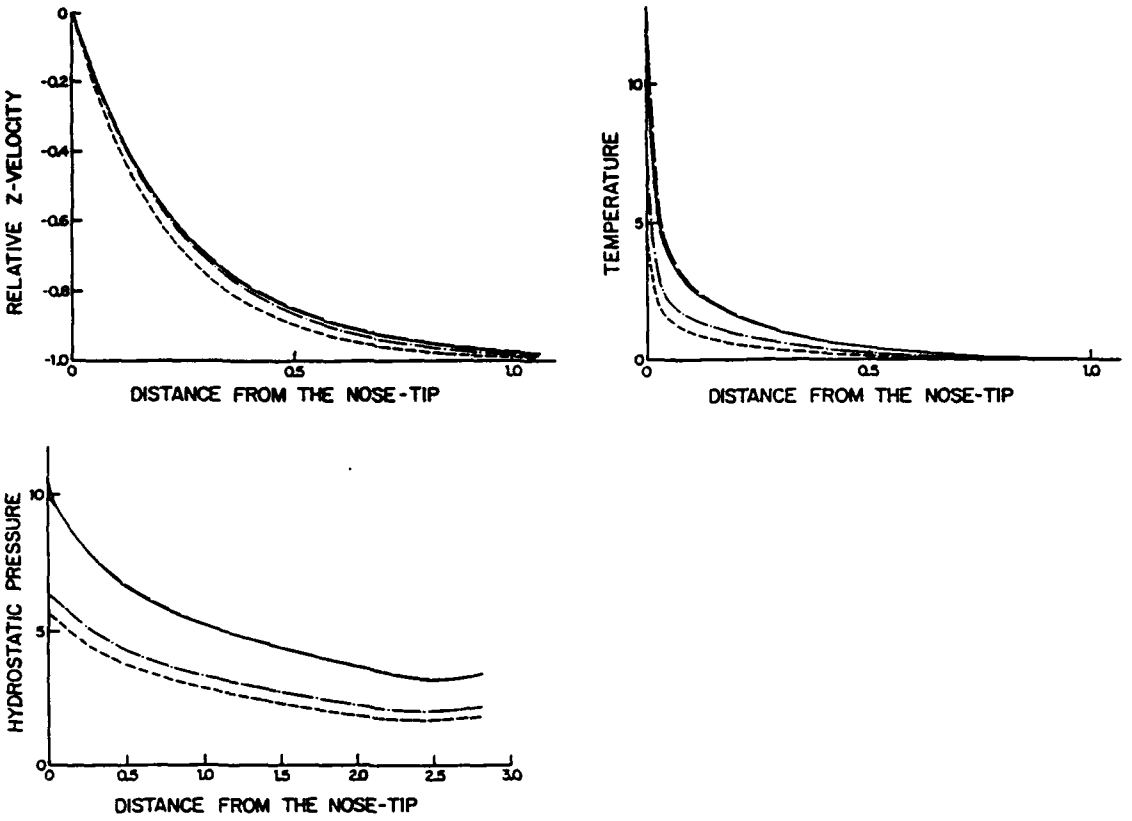

Fig. 11. Effect of strain-hardening, strain-rate hardening and thermal softening on relative z-velocity, temperature change and the hydrostatic pressure at points on the axial line. Explanations see Fig. 8.

one may conclude that the thermal softening reduces its value significantly, especially at points near the nose surface. On the axial line as well as on the nose surface, strain-rate hardening in turn increases strain-hardening. We should add that a steady-state penetration problem is being studied and thus it is tacitly assumed that the increased energy required for deforming the target is available whenever necessary. Fig. 11 depicts the variation of the hydrostatic pressure, temperature and relative z-velocity on the axial line. The hydrostatic pressure, the temperature and the absolute z-velocity of a target particle on the axial line increase with the inclusion of hardening effects but change very little by the consideration also of thermal softening. In order to investigate further the effect of thermal softening, we arbitrarily doubled the value of the thermal softening parameter a. This increased the value of the strain-rate invariant I but changed very little the value of other quantities on the penetrator nose.

On the axial line uniaxial strain conditions prevail approximately. Thus the magnitude of the deviatoric stress s_{zz} at a point should equal 2/3 the effective flow stress σ_e defined as

$$\sigma_e = \sigma_0(1 + bI)^m(1 - a\theta)(1 + \psi/\psi_0)^n.$$

Of all the points on the axial line, the nose tip is the most critical one since the strain-hardening parameter ψ assumes very high values there. In Table 1 below are compared the values of $(-s_{zz})$ and $2/3\,\sigma_e$ at the nose tip. Whereas the error is negligible when the target material is rigid/perfectly plastic, it is rather high for the other three cases. A possible reason for the high error is that values of ψ at the center are sensitive to the value of the artificial viscosity δ eventhough other field variables show negligible dependence upon the precise value of δ within a certain range. To support this reasoning, we list in Table 2 values of the same variables but with the effect of strain-hardening neglected. Note that these are for a higher value of the speed of the penetrator.

Finally we remark that results presented here are valid only for the constitutive model used herein.

Table 1. Values of s_{zz} and $2/3\sigma_e$ at the nose-tip for different material models ($\alpha = 1$)

Model	$-\sigma_{zz}$	$-p$	$-s_{zz}$	$2/3\sigma_e$	% difference
Perfectly plastic	6.34	5.64	0.7	0.67	4.5
Strain-hardening	7.05	6.36	0.69	1.12	40.2
+ Rate dependence	11.07	9.88	1.19	2.01	40.7
+ Thermal softening	11.10	10.25	0.85	1.42	40.1

Table 2. Values of s_{zz} and $2/3\sigma_e$ at the nose-tip for different material models ($\alpha = 5$)

Model	$-\sigma_{zz}$	$-p$	$-s_{zz}$	$2/3\sigma_e$	% difference
Perfectly plastic	8.97	8.35	0.62	0.67	7.46
Rate dependence	12.36	11.26	1.10	1.17	5.98
+ Thermal softening	12.28	11.39	0.89	0.96	7.29

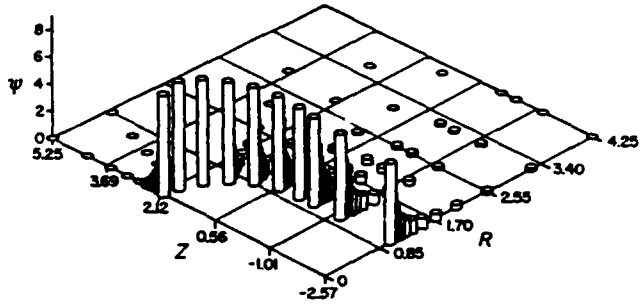

Fig. 12. Variation of strain-hardening parameter ψ in the target region. ($\alpha = 3.0$, $r_n/r_0 = 2.0$)

Conclusion

The computed results show that during the steady state portion of the penetration process, the penetrator nose shape has a significant effect on the deformations of the target. Whereas the strain-rates are higher for the sharper ellipsoidal nose, deformations spread to a larger distance away from the nose surface for the blunt nose. The speed of the penetrator has a weak effect on the axial resisting force experienced by the penetrator even though the hydrostatic pressure does increase with the speed. The inclusion of thermal softening effects increases the strain-rate in the target material but does not alter the pressure distribution on the penetrator nose.

Acknowledgements

This work was supported by the U.S. Army Research Office contract DAAG 29-85-K-0238 to the University of Missouri-Rolla. I thank Mr. Chang-Ho Kim for his help in plotting Figs. 7 and 12.

References

Alekseevskii, v. P. (1966): Penetration of a rod into a target at high velocity. Combust. Expls. and Shock Waves 2, 63–66

Batra, R.C.; Wright, T.W. (1986): Steady state penetration of rigid perfectly plastic targets. Int. J. Eng. Sci. 24, 41–54

Batra, R.C. (1987): Steady state penetration of viscoplastic targets. Int. J. Eng. Sci. 25, 1131–1141

Becker, E.; Carey, G.; Oden, J.T. (1981): Finite elements – an introduction. Englewood Cliffs: Prentice Hall

Brooks, A.N.; Hughes, T.J.R. (1982): Streamline upwind/Petrov-Galerkin formulations for convection dominated flows with particular emphasis on the incompressible Navier-Stokes equations. Comput. Methods Appl. Mech. Eng. 32, 199–259

Bell, J.F. (1968): Physics of large deformations of crystalline solids. New York, Berlin, Heidelberg: Springer
Costin, L.S.; Crisman, E.E.; Hawley, R.H.; Duffy, J. (1979): On the localization of plastic flow in mild steel tubes under dynamic torsional loading. Inst. Phy. Conf. Ser. No. 47, 90–100
Farren, W.D.; Taylor, G.I. (1925): The heat developed during plastic extrusion of metal. Proc. R. Soc. London Ser. A. 107, 422–429
Green, A.E.; McInnis, B.C.; Naghdi, P.M. (1968): Elastic-plastic continua with simple force dipole. Int. J. Eng. Sci. 6, 373–390
Lin, M.R.; Wagoner, R.H. (1986): Effect of temperature, strain, and strain-rate on the tensile flow stress of I.F. steel and stainless steel type 310. Scripta Metallurgica 20, 143–148
Lindholm, U.S.; Johnson, G.R. (1983): Strain-rate effects in metals at large strain-rates. In: Mescal, J.; Weiss, V. (eds.): Material behavior under high stresses and ultrahigh loading rates, pp. 61–79. New York: Plenum Press
Litonski, J. (1977): Plastic flow of a tube under adiabatic torsion. Bull. de l'academic, Polonaise des Sciences, 25, 7–14
Pidsley, P.H. (1984): A numerical study of long rod impact onto a large target. J. Mech. Phys. Solids. 32, 315–333
Tate, A. (1967): A theory for the deceleration of long rods after impact. J. Mech. Phys. Solids. 15, 387–399
Tate, A. (1969): Further results in the theory of long rod penetration. J. Mech. Phys. Solids. 17, 141–150
Wright, T.W.; Batra, R.C. (1986): Adiabatic shear bands in simple and dipolar plastic materials. In: Kawata, K. (ed.): Macro- and micro-mechanics of high velocity deformation and fracture. New York, Berlin, Heidelberg: Springer (in press)
Zienkiewicz, O.C.; Onate, E.; Heinrich, J.C. (1981): A general formulation for coupled thermal flow of metals using finite elements. Int. J. Numer. Methods Eng. 17, 1497–1514

Communicated by S.N. Atluri, January 29, 1987

Int. J. Engng Sci. Vol. 26, No. 11, pp. 1177–1187, 1988
Printed in Great Britain. All rights reserved.

0020–7225/88 $3.00 + 0.00
Copyright © 1988 Pergamon Press plc

EFFECT OF MULTIPLE INITIAL IMPERFECTIONS ON THE INITIATION AND GROWTH OF ADIABATIC SHEAR BANDS IN NONPOLAR AND DIPOLAR MATERIALS

Y. W. KWON and R. C. BATRA

Department of Engineering Mechanics, University of Missouri-Rolla, Rolla, MO 65401-0249, U.S.A.

Abstract—Simple shearing deformations of a viscoplastic block made of nonpolar and dipolar materials, and placed in a hard loading device are studied. Multiple defects in the block are modeled by perturbing the uniform temperature within the block when the material just starts deforming plastically to that given by a cosine function which assumes relative maximum values at several points in the block. It is found that for simple materials, the deformation localizes at points where the perturbed temperature has relative minima when the average applied strain-rate $\dot{\gamma}_0$ is $500\,s^{-1}$ and at the locations of the relative maxima of the perturbed temperature when the applied strain-rate is more than $1000\,s^{-1}$. This transition occurs possibly due to different thermal lengths and the time scales associated with the work-hardening in the two cases. For dipolar materials the deformation localizes near the boundaries of the block abutting the loading device when $\dot{\gamma}_0 = 500\,s^{-1}$ but at the locations of the relative maxima of the perturbed temperature when $\dot{\gamma}_0 = 50{,}000\,s^{-1}$. For both simple and dipolar materials the initiation of the localization of the deformation is considerably delayed as compared to the case when the temperature perturbation has only one bump with its center coinciding with the center of the block.

INTRODUCTION

Recently there has been considerable interest in the study of the localization of the shearing deformation in bodies being deformed at very high strain-rates. These narrow regions of severe deformation are usually referred to as adiabatic shear bands because of the little time available for the heat generated to diffuse away to colder regions of the body. These shear bands are believed to be precursors to shear fractures.

Most analytical studies (e.g. Recht [1], Staker [2], Clifton [3], Burns [4], Bai [5] and Shawki *et al.* [6]), aimed at delineating factors that inhibit or enhance the initiation and growth of adiabatic shear bands, have involved analyzing the thermomechanical deformations of a block undergoing simple shearing deformations. Whereas Recht, Staker and Clifton derived conditions based on the assumption that the material point becomes unstable when the shear stress at that point attains a maximum value, Burns, Bai and Shawki *et al.* studied the growth of small perturbations superimposed on a finitely deformed body. In these latter analytical studies the governing equations were linearized around the finitely deformed state. Clifton *et al.* [7], Wright and Batra [8, 9], Wright and Walter [10] and Batra [11] studied, numerically, the effect of introducing a perturbation on a finitely deformed body and did not need to linearize the governing equations. Subsequently Batra [12] introduced the temperature perturbation when the body just starts deforming plastically and investigated the effect of various material parameters on the value of the average strain at which the deformation begins to localize. These perturbations are supposed to simulate the flaws or inhomogeneities present in the material. Whereas in previous works one or two flaws/defects were presumed to be present, here we assume that the flaws are periodically distributed and represent these by an initial temperature distribution given by a cosine function which assumes relative maximum values at several points in the specimen. It is found that the presence of many flaws/defects delays considerably the initiation of the localization of the deformation.

Wright and Batra [9] and Batra [11] have shown that the inclusion of the strain gradients as an independent kinematic variable has a stiffening effect in the sense that it delays considerably the onset of shear bands. Batra [11] also studied the interaction among shear bands in simple and dipolar materials. His numerical calculations revealed that two bands that will grow independently in simple materials will coalesce in dipolar materials. Herein it is found that in dipolar materials the deformation localizes near the boundaries of the specimen at an applied

strain-rate $\dot{\gamma}_0$ of $500\,s^{-1}$ but at the locations of the relative maxima of the initial temperature when $\dot{\gamma}_0 = 50{,}000\,s^{-1}$. In simple materials the deformation localized at points between the locations of the relative maxima of the initial temperature at $\dot{\gamma}_0 = 500\,s^{-1}$. However, at $\dot{\gamma}_0 = 50{,}000\,s^{-1}$ the points where the deformation localized coincided with the locations of the relative maxima of the initial temperature.

FORMULATION OF THE PROBLEM

Equations governing the thermomechanical deformations of a block occupying the region $-1 \leq y \leq +1$ and made of a viscoplastic material undergoing simple shearing deformations may be written [9, 11] as

$$\dot{v} = \frac{1}{\rho}(s - l\sigma_{,y})_{,y}, \tag{1}$$

$$\dot{\theta} = k\theta_{,yy} + \Lambda(s^2 + \sigma^2), \tag{2}$$

$$\dot{s} = \mu(v_{,y} - \Lambda s), \tag{3}$$

$$\dot{\sigma} = l\mu\left(v_{,yy} - \frac{\Lambda}{l}\sigma\right), \tag{4}$$

$$\dot{\psi} = \Lambda(s^2 + \sigma^2)\Big/\left(1 + \frac{\psi}{\psi_0}\right)^n, \tag{5}$$

$$\Lambda = \max\left\{0, \left[\left(\frac{(s^2 + \sigma^2)^{\frac{1}{2}}}{\left(1 + \frac{\psi}{\psi_0}\right)^n (1 - a\theta)}\right)^{1/m} - 1\right]\Big/[b(s^2 + \sigma^2)^{1/2}]\right\}. \tag{6}$$

These equations are written in terms of nondimensional variables. Equations (1) and (2) represent, respectively, the balance of linear momentum and the balance of internal energy. The balance of mass simply gives that the mass density ρ stays constant since the simple shearing deformation is isochoric. Here v is the x-velocity of a material particle, θ its temperature change from that in the reference configuration, s is the shear stress in the x direction acting on the plane y = constant, σ is the dipolar stress on this plane, k the thermal diffusivity, parameters ψ_0 and n describe the strain-hardening of the material, parameters b and m characterize the strain-rate sensitivity of the material, the parameter a defines the thermal softening, the parameter l is the material characteristic length, and μ is the shear modulus. The parameter ψ may be thought of as an internal variable and eqn (5) its growth equation. It is used to describe the work-hardening of the material. Note that the numerator on the right-hand side of eqn (5) equals the plastic working. A comma followed by y signifies partial differentiation with respect to y and a superimposed dot stands for the material time differentiation. Implicit in eqn (2) are the assumptions that the specific internal energy equals the specific heat multiplied by the change in temperature, Fourier's law of heat conduction holds and that all of the plastic working is converted into heat. The material characteristic length l equals zero for nonpolar materials and is positive for dipolar materials.

In eqns (1)–(6) it has also been assumed that the strain rate $\dot{\gamma} = v_{,y}$ and its gradient $\dot{d} = v_{,yy}$ have additive decompositions into elastic $\dot{\gamma}_e$, $\dot{d}_e$ and plastic parts $\dot{\gamma}_p$, $\dot{d}_p$. That is

$$\dot{\gamma} = \dot{\gamma}_e + \dot{\gamma}_p, \qquad \dot{d} = \dot{d}_e + \dot{d}_p. \tag{7}$$

For the plastic parts $\dot{\gamma}_p$ and $\dot{d}_p$ we have made the following constitutive assumptions:

$$\dot{\gamma}_p = \Lambda s, \qquad \dot{d}_p = \frac{\Lambda\sigma}{l}. \tag{8}$$

Λ in these equations equals zero whenever the deformations are elastic and is positive for plastic deformations. In order to determine whether a material point is deforming elastically or

plastically, we presume that a scalar loading or yield function f exists such that

$$f(s, \sigma, \theta, \dot{\gamma}_p, \dot{d}_p) = \kappa \tag{9}$$

and

$$\frac{\partial f}{\partial \Lambda}(s, \sigma, \theta, \Lambda s, \Lambda \sigma) < 0 \tag{10}$$

for all admiss.ible values of s, σ and θ. κ in eqn (9) describes the work hardening of the material. The criterion for elastic and plastic deformation at a material point is

$$f(s, \sigma, \theta, 0, 0) \leq 0, \text{ elastic} \tag{11}$$

$$f(s, \sigma, \theta, 0, 0) > 0, \text{ plastic.} \tag{12}$$

When eqn (12) holds, eqn (9) has a unique solution for Λ because of the requirement (10). Equation (6) gives the value of Λ for the choices

$$f(s, \sigma, \theta, \dot{\gamma}_p, \dot{d}_p) = \frac{(s^2 + \sigma^2)^{\frac{1}{2}}}{(1 - a\theta)[1 + b(\dot{\gamma}_p^2 + \dot{d}_p^2)^{\frac{1}{2}}]^m}, \tag{13}$$

and

$$\kappa = \left(1 + \frac{\psi}{\psi_0}\right)^n. \tag{14}$$

The details of deriving eqns (1)–(6) may be found in Wright and Batra [9] and Green *et al.* [13].

The governing equations (1)–(6) are to be supplemented by initial conditions and boundary conditions. For the former we take

$$\begin{aligned} &v(y, 0) = y, \quad \theta(y, 0) = 0, \quad \sigma(y, 0) = 0, \quad \psi(y, 0) = 0, \\ &\theta(y, 0) = (1 + \cos 20\pi y)/20, \\ &s(y, 0) = [1 - a\theta(y, 0)], \end{aligned} \tag{15}$$

and for the latter

$$v(\pm 1, t) = \pm 1, \quad \theta_{,y}(\pm 1, t) = 0, \quad \sigma(\pm 1, t) = 0. \tag{16}$$

Thus the material point is initially presumed to lie on its yield surface that corresponds to quasistatic deformations, no work hardening and its initial temperature. The initial stress distribution is nonuniform and $\dot{\gamma}_p = 0$ initially at all points in the body.

We seek solutions of eqns (1)–(6) subjected to initial and boundary conditions (15) and (16) that exhibit the following symmetries and antisymmetries:

$$\begin{aligned} &v(-y, t) = -v(y, t), \quad \theta(-y, t) = \theta(y, t), \\ &\sigma(-y, t) = -\sigma(y, t), \quad s(-y, t) = s(y, t), \quad \psi(-y, t) = \psi(y, t). \end{aligned} \tag{17}$$

However we do not assume *a priori* that the solution is periodic. Hence we can reduce the domain of study to $[0, 1]$ and replace boundary conditions (16) by

$$\begin{aligned} &v(1, t) = 1, \quad v(0, t) = 0, \quad \theta_{,y}(1, t) = 0, \quad \theta_{,y}(0, t) = 0, \\ &\sigma(1, t) = 0, \quad \sigma(0, t) = 0. \end{aligned} \tag{18}$$

The nonlinear coupled governing equatic.is (1)–(5) under the side conditions (15) and (18) are solved numerically by the finite element method. We note that there are no existence and uniqueness theorems available for such a system of equations. Also there is no hope of solving these equations analytically, therefore we solve them numerically.

COMPUTATION AND DISCUSSION OF RESULTS

We introduce the auxiliary variables

$$u = v_{,y}, \qquad g = \theta_{,y}, \qquad p = \sigma_{,y} \tag{19}$$

and rewrite eqns (1)–(4) as

$$\dot{v} = \frac{1}{\rho}(s - lp)_{,y}, \tag{20}$$

$$\dot{\theta} = kg_{,y} + \Lambda(s^2 + \sigma^2), \tag{21}$$

$$\dot{s} = \mu(u - \Lambda s), \tag{22}$$

$$\dot{\sigma} = l\mu\left(u_{,y} - \frac{\Lambda}{l}\sigma\right). \tag{23}$$

Whereas Batra [11] integrated eqns (19)–(23) and (5) by the Crank–Nicholson–Galerkin finite element method to find u, g, p, v, θ, s, σ and ψ at a node point, we have integrated eqns (1)–(5) by the same method and computed v, θ, s, σ and ψ at a node point. For a test problem, the computed results by the two methods were identical but the core storage needed and the CPU time used was considerably less with the present method. Here we divided the domain $[0, 1]$ into 400 uniform subdomains or finite elements and used $\Delta t = 5 \times 10^{-6}$ in computing the results.

The values of the nondimensional parameters a, μ, n, ψ_0 and m do not depend upon the applied average strain-rate $\dot{\gamma}_0$ but those of ρ, k and b vary as $\dot{\gamma}_0^2$, $\dot{\gamma}_0^{-1}$ and $\dot{\gamma}_0$ respectively. The values of these variables, which correspond to a typical hard steel, used to compute numerical results are

$$a = 0.4973, \qquad \mu = 240.3, \qquad n = 0.09, \qquad \psi_0 = 0{\cdot}017, \qquad m = 0.025$$

and

$$\rho = 3.928 \times 10^{-5}, \qquad k = 3.978 \times 10^{-3}, \qquad b = 5 \times 10^{6} \text{ when } \dot{\gamma}_0 = 500\,\text{s}^{-1},$$

$$\rho = 3.928 \times 10^{-1}, \qquad k = 3.978 \times 10^{-5}, \qquad b = 5 \times 10^{8} \text{ when } \dot{\gamma}_0 = 50{,}000\,\text{s}^{-1}.$$

The presumed value of the thermal softening coefficient a is approx. 7 times the value for a typical steel. This is done so that the peak in the shear stress–shear strain curve occurs at a lower value of the average strain and therefore the computational time for the problem is significantly reduced. This choice of the value of a should not affect the qualitative nature of results presented here.

For homogeneous deformations of the block Fig. 1 depicts the shear stress–shear strain curve for an applied strain-rate of $500\,\text{s}^{-1}$. The peak in the curve occurs at an average strain of 0.093. At the higher strain-rate of $50{,}000\,\text{s}^{-1}$ the shear stress peak[illegible] at an average strain of 0.085. The temperature perturbation was introduced at an av[illegible]ain corresponding to point I in Fig. 1.

Figure 2 shows how the temperature, plastic strain-rate and the shear stress s evolve in the steel block when it is modeled as a nonpolar material, the initial temperature distribution is nonuniform, and the block is deformed at an average strain-rate of $500\,\text{s}^{-1}$. Figure 3 depicts the corresponding results for an applied strain-rate of $50{,}000\,\text{s}^{-1}$. Note that the initial temperature has the relative maximum value of 0.10 at $y = 0.0$, 0.1, 0.2, 0.3, 0.4, 0.5, 0.6, 0.7, 0.8, 0.9 and 1.0. In each case the shear stress s becomes essentially uniform after a short while and stays uniform throughout the thickness of the block. It first rises because of the work hardening and strain-rate hardening effects and begins to decrease when these hardening effects are overcome by the thermal softening. At the lower strain-rate of $500\,\text{s}^{-1}$ there is no noticeable drop in the shear stress even when the deformation has started to localize but at the higher strain-rate of $50{,}000\,\text{s}^{-1}$ the shear stress s decreases considerably after the deformation begins to localize.

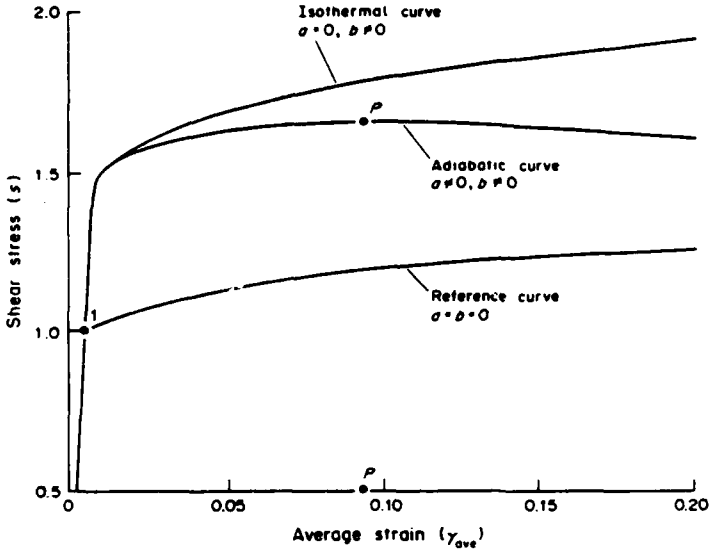

Fig. 1. Shear stress-strain curve for simple shearing deformations of a steel block at $\dot{\gamma}_0 = 500\,s^{-1}$.

This rather noticeable drop in the shear stress with increasing average strain after the deformation begins to localize has been pointed out by Wright and Walter [10]. Note that the temperature rise in the two cases at places where the deformation localizes is nearly equal to each other at the instant of the onset of the localization process. However, the temperature is more evenly distributed at $\dot{\gamma}_0 = 500\,s^{-1}$ as compared to that at $\dot{\gamma}_0 = 50{,}000\,s^{-1}$ in the sense that the difference between the maximum and the minimum temperature stays small for $\dot{\gamma}_0 = 500\,s^{-1}$ even after the deformation localizes. The rate of growth of the plastic strain-rate is more gradual at $\dot{\gamma}_0 = 500\,s^{-1}$ as compared to that at $\dot{\gamma}_0 = 50{,}000\,s^{-1}$.

The striking differences between the two cases are outlined below.

(a) First is the average strain at the instant the deformation begins to localize. For $\dot{\gamma}_0 = 500\,s^{-1}$ the average strain of 0.624 at which the deformation has essentially localized is nearly 7 times the strain at which the peak stress occurs during homogeneous deformations of the block. However, for $\dot{\gamma}_0 = 50{,}000\,s^{-1}$ the localization of the deformation occurs at an average strain of 0.09 which almost equals the strain of 0.085 at which the shear stress attains the maximum value during homogeneous deformations of the block. For comparison purposes we note [14] that when a temperature perturbation with a single bump centered at $y = 0$ is introduced, the shear bands form at an average strain of 0.0814 and 0.206 for $\dot{\gamma}_0 = 500\,s^{-1}$ and $50{,}000\,s^{-1}$, respectively. On the hypothesis that a temperature perturbation simulates material inhomogeneities or flaws in the body, the present results indicate the initiation of shear bands is delayed for $\dot{\gamma}_0 = 500\,s^{-1}$ when there are more defects uniformly distributed in the specimen, and for $\dot{\gamma}_0 = 50{,}000\,s^{-1}$ when there is only one defect present in the specimen.

(b) Secondly, the places where the peak temperature rise and the peak plastic strain-rate occur are quite different in the two cases. Whereas at $\dot{\gamma}_0 = 500\,s^{-1}$ the peak values of the temperature rise and the plastic strain-rate occur at places where the initial temperature perturbation had relative minimum values, at $\dot{\gamma}_0 = 50{,}000\,s^{-1}$ the peaks of the temperature rise and the plastic strain-rate coincide with the locations of the maxima of the temperature perturbation. That the centers of shear bands for $\dot{\gamma}_0 = 50{,}000\,s^{-1}$ coincide with the locations of the maxima of the initial temperature perturbation was also observed in the case the initial temperature perturbation assumed peak values at six equidistant points rather than eleven. In this case, the deformation localized at an average strain of 0.1122.

In order to understand the reasons for the above differences we note that, for nonpolar materials (i.e. $l = 0$), imbedded in the governing equations (1)–(6) are three length scales [9, 12] namely, the geometric length, a thermal length and a viscous length, and seven non-dimensional parameters, namely, the mass density ρ, the elastic modulus μ, the rate of

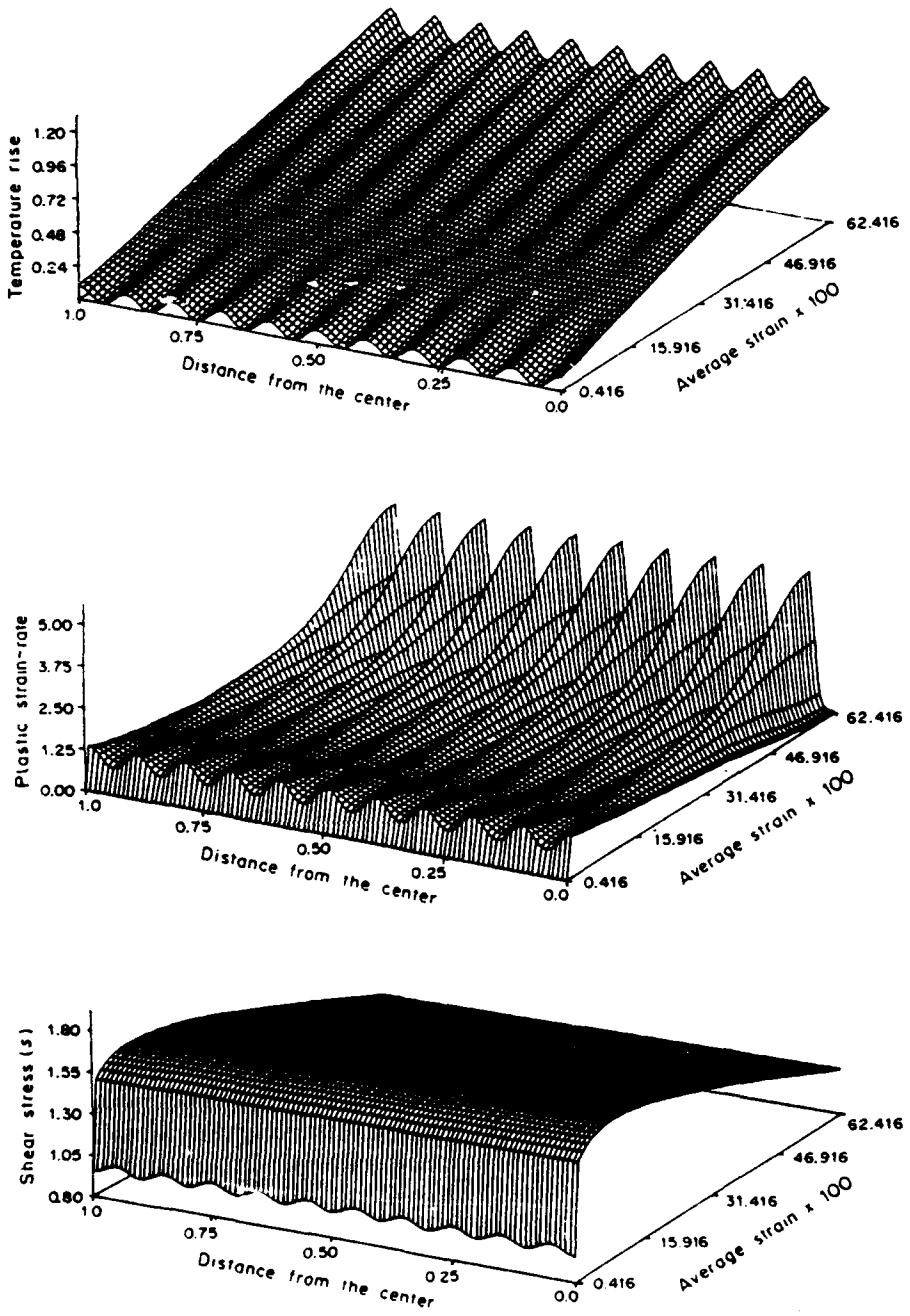

Fig. 2. Evolution of the temperature, plastic strain-rate and the shearing stress in nonpolar materials at $\dot{\gamma}_0 = 500\,s^{-1}$.

thermal softening a, two for work hardening n and ψ_0, and two for rate hardening b and m. Whereas the thermal length varies as $\dot{\gamma}_0^{-1/2}$, the viscous length does not depend upon $\dot{\gamma}_0$ but is a function of the material parameters. The non-dimensional thermal length (= thermal length/height of the specimen) is reduced from 0.6307 to 0.006307 when $\dot{\gamma}_0$ is increased from 500 to 50,000 s^{-1}. That the decrease in the thermal length is among the factors responsible for the aforementioned differences was confirmed by running the $\dot{\gamma}_0 = 500\,s^{-1}$ case with the thermal conductivity arbitrarily set equal to zero. In this case the thermal length is zero and the peak strain-rates occurred at the locations of the maxima of the initial perturbation as expected. To seek an answer to the question "For what value of $\dot{\gamma}_0$ does the above referred transition occur?", we conducted numerical experiments for different values of $\dot{\gamma}_0$ between 500

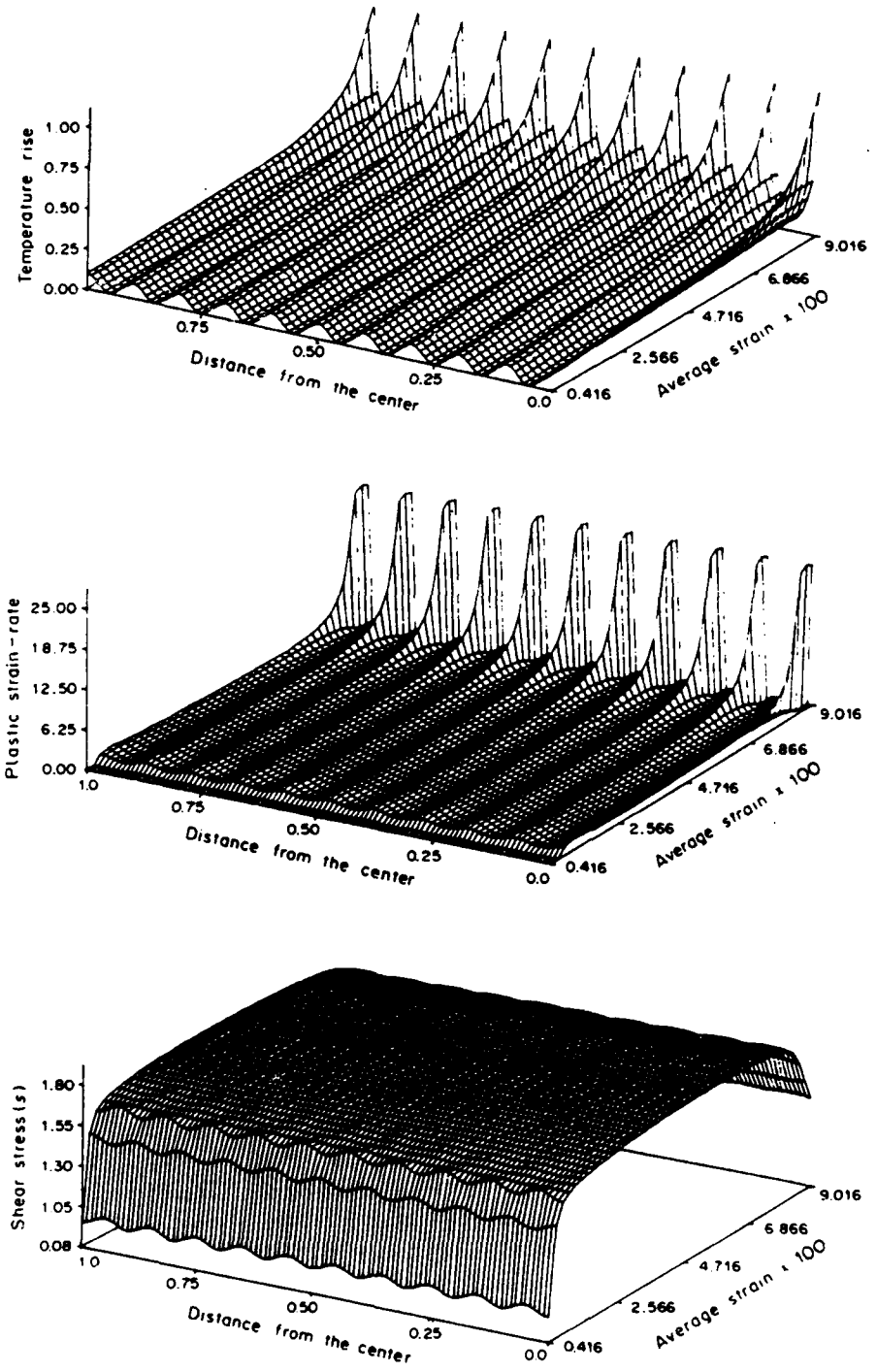

Fig. 3. Evolution of the temperature, plastic strain-rate and the shear stress in nonpolar materials at $\dot{\gamma}_0 = 50{,}000\,s^{-1}$.

and $50{,}000\,s^{-1}$ and found $\dot{\gamma}_0 = 1000\,s^{-1}$ to be the critical strain-rate above which the deformation localized at points of maxima of the initial temperature perturbation and below which it localized at other points.

It appears that it is the higher value of the thermal length at $\dot{\gamma}_0 = 500\,s^{-1}$ that delays the initiation of the localization process too. A close examination of the computed results indicated that initially the material points at the locations of the temperature maxima experienced peak plastic strain-rates and higher values of the work hardening parameter ψ as compared to their

neighbors. Since the shear stress became essentially uniform shortly after the temperature perturbation was introduced, the increased value of ψ resulted in reduced values of Λ, $\dot{\gamma}_p$ and the heat generated due to plastic working at these points. This coupled with the heat conduction tended to make the temperature virtually uniform throughout the specimen. Of course the temperature and work-hardening parameter did not become exactly uniform because if they did, the specimen will subsequently undergo homogeneous deformations only. To lend credence to this hypothesis we increased artificially the thermal conductivity to 100 times its previous value but kept $\dot{\gamma}_0 = 500\,s^{-1}$. In this case no shear band formed and the temperature field within the specimen became uniform and stayed so during the ensuing deformations. To understand the role played by the work-hardening, we conducted a numerical experiment with $n = 0$ and $\dot{\gamma}_0 = 500\,s^{-1}$. This resulted in neglecting the effect of the work-hardening on the deformations of the block. In this case the deformation localized at points where the initial temperature perturbation assumed peak values.

Another reason for the localization not to occur at the locations of the peaks in the initial temperature could be improper choices of the mesh and Δt. We reduced Δt to one-half of its value, but used the same mesh and recomputed results for $\dot{\gamma}_0 = 500\,s^{-1}$. For smaller time step the deformation localized at the same points as it did earlier for the large time step.

Since the distance between the locations of the points where the plastic strain-rate eventually peaked and points of maxima of the initial temperature perturbation equals approximately the length of 20 elements, it is unlikely that the finite-element mesh caused the shift.

When $\dot{\gamma}_0$ is increased from 500 to $50{,}000\,s^{-1}$, the non-dimensional mass density increases from 3.93×10^{-5} to 3.93×10^{-1}. In [14] the initial temperature perturbation had only one bump centered at $y = 0$. It was found that the shear stress distribution within the specimen was uniform for $\dot{\gamma}_0 = 500\,s^{-1}$ but non-uniform with the lowest value at $y = 0$ for $\dot{\gamma}_0 = 50{,}000\,s^{-1}$. No such non-uniformity in the shear stress distribution has been observed for the periodic initial temperature perturbation introduced herein.

In Figs 4 and 5 are plotted the evolution of the temperature, plastic strain-rate and the shear stress s when the material of the block is modeled as a dipolar material with $l = 0.01$ and the block is deformed at an average strain-rate $\dot{\gamma}_0$ of 500 and $50{,}000\,s^{-1}$ respectively. Whereas for $\dot{\gamma}_0 = 500\,s^{-1}$ only one shear band with center at $y = 1.0$ forms, at $\dot{\gamma}_0 = 50{,}000\,s^{-1}$ the deformation localizes around the location of the peaks of the initial temperature. In each case the initiation of the localization of the deformation is delayed as compared to that for nonpolar materials [14]; the delay is more pronounced at the higher applied strain-rate. Whereas for nonpolar materials the average strain at which the deformation localizes for $\dot{\gamma}_0 = 500\,s^{-1}$ is nearly seven times that for $\dot{\gamma}_0 = 50{,}000\,s^{-1}$, for dipolar materials the average strains at which the deformation localizes in the two cases are nearly equal to each other. Also for nonpolar materials the shear stress s becomes essentially uniform throughout the specimen soon after the initial perturbation is introduced and stays uniform within the block, such is not the case for dipolar materials. For dipolar materials the amplitude of the oscillations in the shear stress distribution is extremely small for $\dot{\gamma}_0 = 500\,s^{-1}$ but at $\dot{\gamma}_0 = 50{,}000\,s^{-1}$ it is noticeable and seems to grow as the deformation localizes. Note that for dipolar materials it is $(s - l\sigma_{,y})$ and not s that acts as a flux for the linear momentum. The average shear stress s exhibits the same behavior as that for nonpolar materials in the sense that it first increases and subsequently begins to drop when thermal softening effects exceed the combined effects of strain and strain-rate hardening.

At $\dot{\gamma}_0 = 500\,s^{-1}$ the initial temperature distribution tends to become uniform throughout the block and stays virtually uniform until the deformation begins to localize near $y = 1.0$. At that instant the temperature near $y = 1.0$ increases slightly more than that at other places. Of course the temperature at every point in the body keeps on increasing because of the plastic working. Why the shear band forms near $y = 1.0$ and not near $y = 0.0$ is not clear. At the higher applied strain-rate $\dot{\gamma}_0 = 50{,}000\,s^{-1}$ neither the temperature nor the plastic strain-rate ever becomes uniform within the block. It seems that the amplitude of the temperature oscillations keeps on increasing with the increase in the average strain in the specimen.

For dipolar materials, in addition to the thermal and viscous lengths, there are three length scales [13] characteristic of the material. Herein as well as in two previous studies [9, 11] the

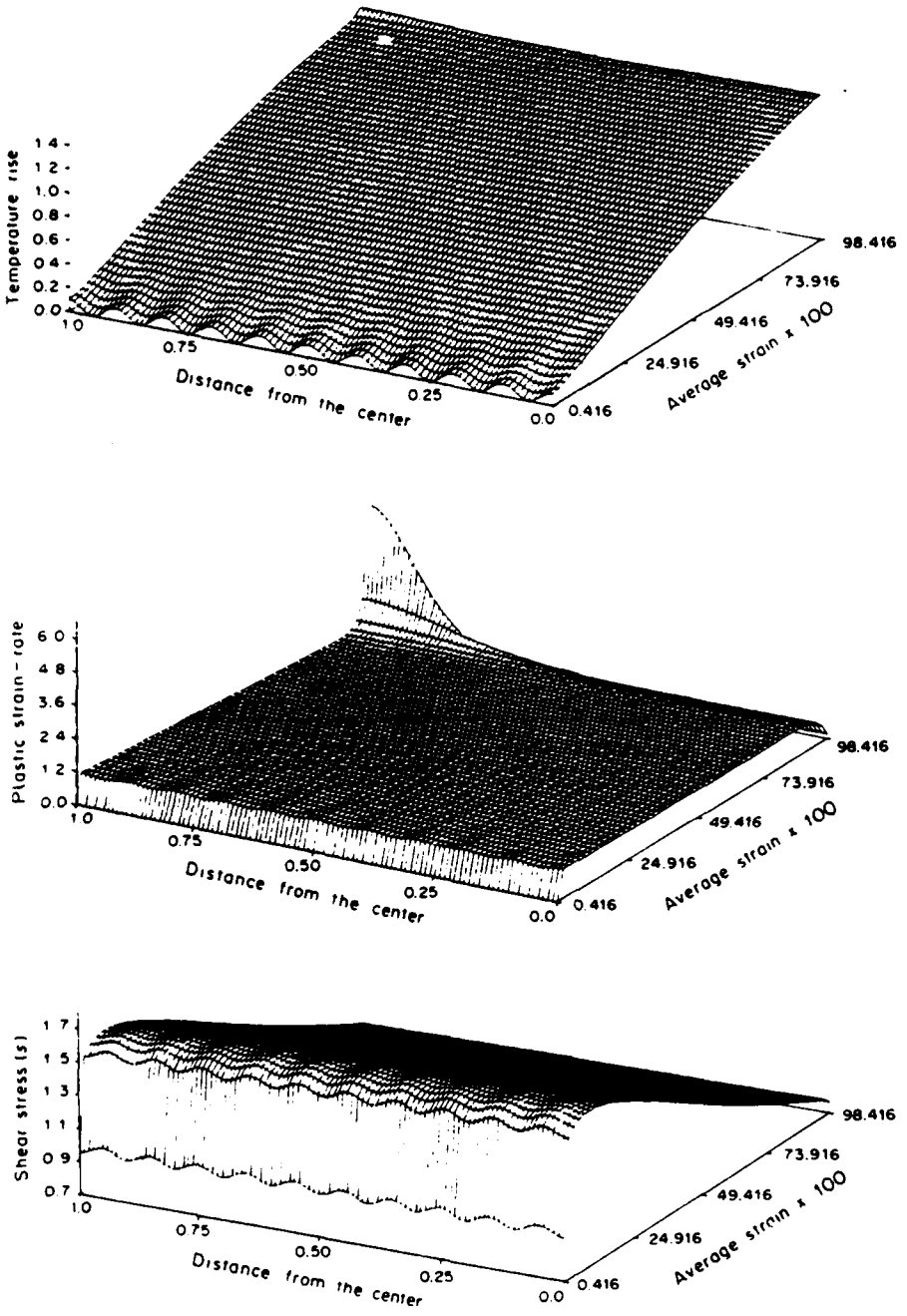

Fig. 4. Evolution of the temperature, plastic strain-rate and the shear stress in dipolar materials ($l = 0.01$) at $\dot{\gamma}_0 = 500\,s^{-1}$.

three length scales have been set equal to each other. The problem when the three length scales are different is under investigation and will be reported on in a future paper. The previous work with $\dot{\gamma}_0 = 500\,s^{-1}$ and with a single temperature perturbation centered at $y = 0$ indicated that the inclusion of dipolar effects delays considerably the localization of the deformation. The delay observed here by comparing results plotted in Figs 3 and 5 is significantly more as compared to that found previously and also that computed presently for $\dot{\gamma}_0 = 50{,}000\,s^{-1}$. The main reason for the difference between the previously computed [9, 11] and current results is due to the number of flaws/imperfections considered in the two cases. An explanation for the difference between the results computed at $\dot{\gamma}_0 = 500$ and $50{,}000\,s^{-1}$ lies in the different values of the thermal lengths in the two cases. At $\dot{\gamma}_0 = 500\,s^{-1}$ the temperature

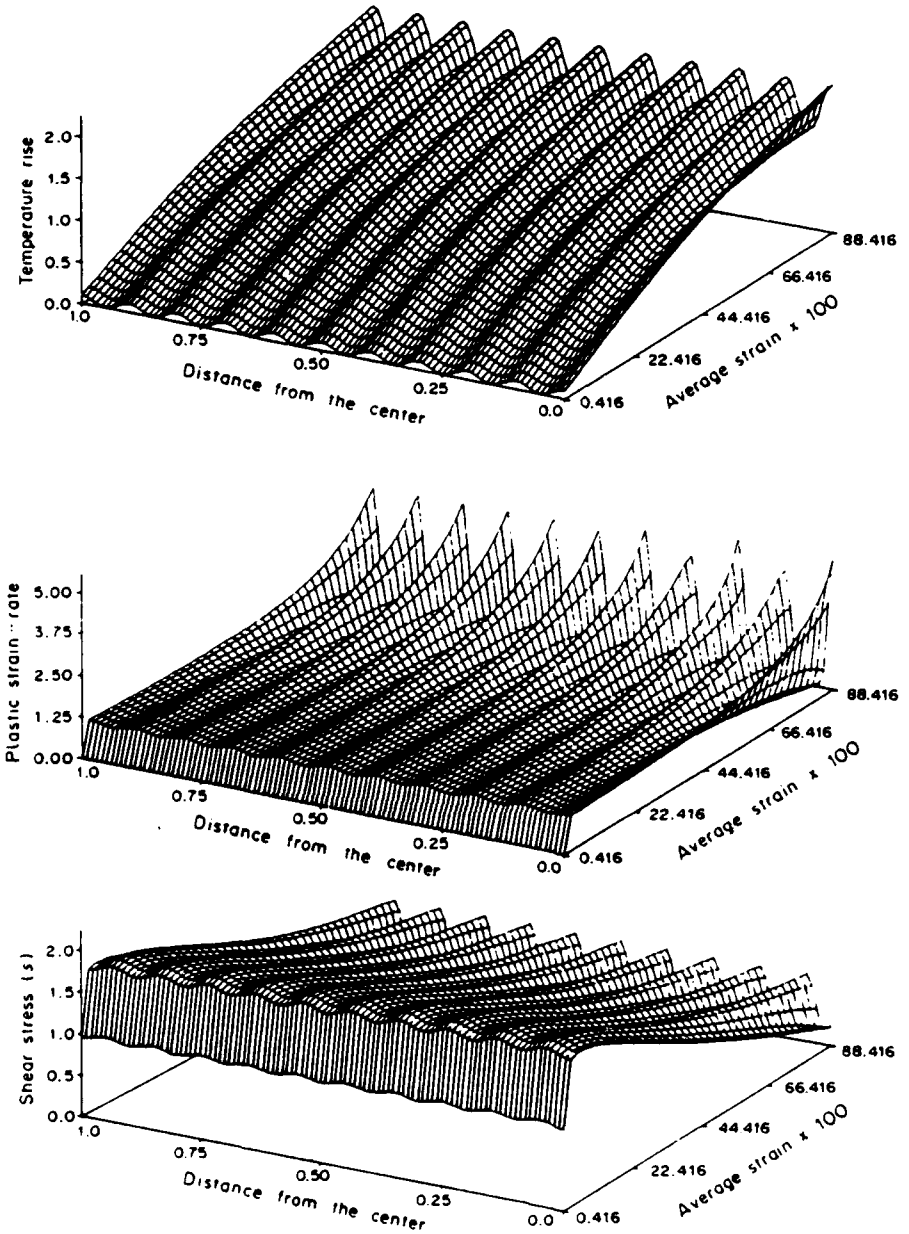

Fig. 5. Evolution of the temperature, plastic strain-rate and the shear stress in dipolar materials ($l = 0.01$) at $\dot{\gamma}_0 = 50{,}000\,s^{-1}$.

initially tends to become uniform because of heat conduction and once the temperature fluctuations die out the block deforms homogeneously. What eventually causes the temperature to rise at $y = 1.0$ and not at $y = 0.0$ is unclear.

We note that the CPU time required to compute results for the dipolar materials is nearly four times that needed for non-polar materials. Thus not many numerical experiments could be conducted for dipolar materials.

CONCLUSIONS

For nonpolar materials the initiation of the shear bands is significantly delayed at $\dot{\gamma}_0 = 500\,s^{-1}$ when a periodic temperature perturbation with eleven peaks is introduced initially as compared to the case when the initial temperature perturbation has a single bump with peak at the center

of the block. However, for $\dot{\gamma}_0 = 50{,}000\,s^{-1}$ the reverse happens. In the former case the deformation localizes at points where the initial temperature has relative minima values, in the latter case the centers of shear bands coincide with the places where the initial temperature has relative maximum values. These transitions are found to occur at $\dot{\gamma}_0 = 1000\,s^{-1}$ and seem to be caused by the lower value of the thermal length at the higher value of $\dot{\gamma}_0$ and the different time scale associated with the work-hardening in the two cases.

For dipolar materials the average strains in the specimen at which the deformation localizes at $\dot{\gamma}_0 = 500$ and $50{,}000\,s^{-1}$ are nearly equal to each other. These values of average strains are higher than the corresponding values for nonpolar materials. Only one band forms at $\dot{\gamma}_0 = 500\,s^{-1}$ but the number of shear bands equal the number of peaks in the initial temperature at $\dot{\gamma}_0 = 50{,}000\,s^{-1}$.

Acknowledgements—This work was partially supported by the U.S. Army Research Office Contract DAAG29-85-K-0238 and the U.S. NSF grant MSM-8715952 to the University of Missouri-Rolla. We are indebted to Dr T. W. Wright and John Walter for useful discussions on the subject.

REFERENCES

[1] R. F. RECHT, *ASME J. appl. Mech.* **31**, 189 (1964).
[2] M. R. STAKER, *Acta metall.* **29**, 683 (1981).
[3] R. J. CLIFTON, NRC National Material Advisory Board (U.S.) Report 356 (1980).
[4] T. J. BURNS, *Q. Jl appl. Math.* **43**, 65 (1985).
[5] Y. L. BAI, in *Shock Waves and High Strain Rate Phenomenon in Metals* (Edited by M. A. MEYERS and L. E. MURR), p. 277. Plenum Press, New York (1981).
[6] T. G. SHAWKI, R. J. CLIFTON and G. MAJDA, ARO Report DAAG 29-81-K-0121/3, Brown University (1983).
[7] R. J. CLIFTON, J. DUFFY, K. A. HARTLEY and T. G. SHAWKI, *Scripta metall* **18**, 43 (1984).
[8] T. W. WRIGHT and R. C. BATRA, *Int. J. Plasticity* **1**, 205 (1985).
[9] T. W. WRIGHT and R. C. BATRA, in *Proc. IUTAM Symposium on Macro- and Micromechanics of High Velocity Deformation and Fracture* (Edited by K. KAWATA and J. SHIOIRI), p. 189, Springer, Berlin (1987).
[10] T. W. WRIGHT and J. W. WALTER, *J. Mech. Phys. Solids.* **35**, 701 (1987).
[11] R. C. BATRA, *Int. J. Plasticity* **3**, 75 (1987).
[12] R. C. BATRA, *Int. J. Solids Struct.* **23**, 1435 (1987).
[13] A. E. GREEN, B. C. McINNIS, and P. M. NAGHDI, *Int. J. Engng Sci.* **6**, 373 (1968).
[14] R. C. BATRA, *ASME J. appl. Mech.* **55**, 229 (1988).

(*Revised version received* 2 *March* 1988)

International Journal of Plasticity, Vol. 3, pp. 75-89, 1987
Printed in the U.S.A.

0749-6419/87 $3.00 + .00
1987 Pergamon Journals Ltd

THE INITIATION AND GROWTH OF, AND THE INTERACTION AMONG, ADIABATIC SHEAR BANDS IN SIMPLE AND DIPOLAR MATERIALS

R. C. BATRA

University of Missouri-Rolla

Abstract - The problem of simple shearing of a block of simple (nonpolar) and dipolar thermoviscoplastic materials is studied with the objectives of exploring the initiation and growth of, and the interaction among, adiabatic shear bands. A shear band is assumed to have formed if the addition of a perturbation to the homogeneous fields just before the peak stress is reached results in a localization of the shear strain. The effect of adding perturbations of different sizes and of the same size but at different locations in the slab is investigated. It is shown that in simple materials, two shear bands coalesce if the distance between them is small but grow independently, although at a slower rate, if the distance between them is large. However, for dipolar materials, the two bands coalesce even when the distance between them at the time of their initiation is 20 times the material characteristic length.

1. INTRODUCTION

Adiabatic shear is the name given to a localization phenomenon that occurs during high-rate plastic deformation, such as machining, explosive forming, shock impact loading, ballistic penetration, fragmentation, ore crushing, impact tooling failure, and metal shaping and forming processes. The localization of shear strain has been observed mostly in steels, but also in nonferrous metals and polymers. Practical interest in the phenomenon derives from the fact that progressive shearing on an intense shear band provides an undesirable mode of material resistance to imposed deformation, and the bands are often precursors to shear fractures.

Shear band formation is generally enhanced at high strain rates because the lack of time for heat diffusion [1] nonuniform straining to cause nonuniform heating. Nonuniform temperatures enhance plastic flow in the hotter regions and reduce plastic flow in the colder regions. Furthermore, heat generation is greatest in the regions of highest strain rate. Thus, the strain rates in the hot, high-strain-rate regions tend to become larger, while those in the cold, low-strain-rate regions tend to become more nonuniform and may localize into a narrow region referred to as a shear band. Whether or not this thermoplastic instability mechanism leads to shear bands seems to depend upon strain hardening, strain-rate hardening, thermal softening, thermal diffusivity, and the strength of the initial inhomogeneity.

ZENER and HOLLOMAN [1944] recognized the destabilizing effect of thermal softening in reducing the slope of the stress-strain curve in nearly adiabatic deformations. The dynamic torsional experiments of CULVER [1973] on mild steel, titanium, and 6061-T6 aluminum indicate that the localization began near the peak in the stress-strain curve for each material tested. This observation seems to be borne out by the experimental work of COSTIN *et al.* [1980]. They found that in dynamic torsion tests on short specimens of 1018 CRS and 1020 HRS, the shear bands appeared in the 1018 CRS specimens

and not in 1020 HRS specimens. Extensive experiments, conducted at different temperatures and strain rates, revealed that the shear stress–shear strain curve for HRS was increasing monotonically, whereas the curve for CRS had a peak in it.

JOHNSON *et al.* [1983] and LINDHOLM and JOHNSON [1983] reported dynamic torsion test data on six ductile metals and six additional materials of much less ductility. They proposed a constitutive relation that accounts for strain and strain-rate hardening and thermal softening. Their analysis indicates that high ductility tends to produce a relatively wide shear band when compared to other materials. In their experimental setup, the frictional force at the grips provided a constraining axial force. Thus, an axial load or stress component developed with increasing torsional deformation. However, this axial load component was not measured.

STAKER [1981] made use of an instability analysis to model the appearance of adiabatic shear bands in the controlled explosive expansion of steel cylinders. He argued that because of the short times involved in explosive loading the deformation could be considered adiabatic and there was no need to consider the thermophysical properties of materials. RECHT [1964] included heat conduction and thermal softening in the interpretation of shear bands formed during high-speed machining. In his investigation of instability in the shear zone ahead of a cutting tool during orthogonal machining, he used a thermal model incorporating uniform, constant-rate heat generation at a plane in an infinite medium. He showed that the critical strain rate for catastrophic shear in mild steel is 1400 times greater than that for titanium. Based on these data it can be shown that the difference in the thermophysical properties of St and Ti contributes a factor of 6, the ratio of yield stresses a factor of 4, and the difference in mechanical behavior a factor of 58. This last factor is directly proportional to the material's capacity to strain-harden and inversely proportional to its tendency to thermally soften.

In a departure from the notion of a criterion based on a stress maximum, CLIFTON [1980] and BAI [1981] examined the growth of infinitesimal periodic nonuniformities in an otherwise uniform simple shearing deformation. They included strain hardening, thermal softening, strain rate sensitivity, and heat conduction. Bai also included the effect of inertia forces. Both linearized the field equations about the unperturbed time-dependent homogeneous deformation state and found that the magnitude of the imperfections may grow or decay in time, depending on the material parameters, the average rate of strain, and the fixed spatial wavelength of the initial imperfection. BURNS [1983] used a dual asymptotic expansion to include the time dependence of the homogeneous solution in the analysis of the growth of an initially small perturbation. His work suggests that initiation of an unstable shear band, followed by exponential growth, occurs after a critical shear strain corresponding to the peak stress in the homogeneous deformation for the same overall strain rate is reached. On the other hand, SHAWKI *et al.* [1983], by using both numerical and perturbation techniques, concluded that exponential growth is not a sufficient condition for judging whether or not a shear band forms, as the corresponding homogeneous deformation may also grow extremely rapidly once the peak stress has been reached and growth is not restricted to a narrow band.

ERLICH *et al.* [1980] noted that according to simple wave theory applied to one-dimensional plastic wave propagation, the strain level at which the shear tangent modulus becomes zero propagates at zero speed. They postulated a criterion of adiabatic shear band formation based on this "wave trapping" idea. This idea was applied by OLSON *et al.* [1981] in a numerical finite element simulation of plastic shear wave propagation under adiabatic conditions. The numerical solution did indeed exhibit a concentration

of shear strain in a layer of finite elements that was similar in nature to observed adiabatic shear bands.

In studying the growth of shear bands in the center of a finite slab after initiation at a small imperfection, MERZER [1983] concluded that the final width of the band depends on the thermal diffusivity and the overall strain rate. WU and FREUND [1984], in studying the formation of shear bands at a moving boundary, concluded that thermal diffusivity has little influence on the final shape of the band. The detailed geometry and constitutive equations considered in these two papers are quite different, so perhaps it is not surprising to find apparently contradictory results. In fact, in both papers there are two natural length scales: one arising from the rate effect in the constitutive equation and one arising from heat conductivity. In the latter paper, these scales have been arbitrarily set equal to each other, whereas in the former paper the relative effect of heat conductivity has been examined parametrically for at least one specific type of constitutive equation.

Recently, WRIGHT and BATRA [1985a, 1985b, and 1986] described the results of computations that simulate the formation of a single shear band from a local temperature inhomogeneity in simple and dipolar materials. A general theory of thermoviscoplasticity, obtained by modifying the dipolar theory of GREEN *et al.* (1968) to include rate effects, was used. Wright and Batra's calculations for simple materials, as well as the experimental observations of Moss [1981], indicated that peak strain gradients reached 0.2 per μm or higher. Therefore, they considered worthwhile to investigate the dipolar effects. Their computations show increasing inhomogeneity in the strain-, temperature-, and strain-rate fields, with the central amplitudes growing at an accelerating rate. The inclusion of dipolar effects has a stiffening effect in the sense that the rate of growth of central amplitudes of the strain, temperature, and strain-rate fields is lower as compared to that for simple materials. For dipolar materials there are at least three length scales: one is from viscous stress effects, the second is from thermal conductivity, and the third is the material characteristic length. WRIGHT and BATRA [1986] studied the case when all three length scales are equal to one another.

This paper describes the results of some numerical experiments conducted with the objective of analyzing the interaction between two shear bands. It also examines the effect of the amplitude and distribution of the initial inhomogeneity on the initiation and growth of a shear band. It is shown that a narrower inhomogeneity results in a rapid growth of the band as compared to a wider one having the same central amplitude. A stronger inhomogeneity results in the formation of a shear band even before the peak in the homogeneous stress-strain curve is reached. The two shear bands that would grow independently in simple materials seem to coalesce in dipolar materials even when the material characteristic length is $\frac{1}{50}$ of the distance between them at the time of their initiation.

We note that there is no experimental evidence available on the interaction between two or more shear bands in simple or dipolar materials.

II. FORMULATION OF THE SIMPLE SHEARING PROBLEM

We study the simple shearing deformations of a dipolar viscoplastic material and assume that all of the variables have been nondimensionalized. Thus, the body occupies the infinite slab bounded by the planes $y = \pm 1$. Referring the reader to WRIGHT and BATRA [1986] for details, we note that the governing equations are

$$\dot{v} = \frac{1}{\rho}(s - l\sigma_{,y})_{,y}, \tag{1}$$

$$\dot{\theta} = k\theta_{,yy} + \Lambda(s^2 + \sigma^2), \tag{2}$$

$$\dot{s} = \mu(v_{,y} - \Lambda s), \tag{3}$$

$$\dot{\sigma} = l\mu\left(v_{,yy} - \frac{\Lambda}{l}\sigma\right), \tag{4}$$

$$\dot{\psi} = \Lambda(s^2 + \sigma^2)\Big/\left(1 + \frac{\psi}{\psi_0}\right)^n, \tag{5}$$

$$\Lambda = \max\left[0, \left\{\left(\frac{(s^2 + \sigma^2)^{1/2}}{\left(1 + \frac{\psi}{\psi_0}\right)^n (1 - a\theta)}\right)^{1/m} - 1\right\}\Big/\{b(s^2 + \sigma^2)^{1/2}\}\right] \tag{6}$$

with boundary conditions

$$v(\pm 1, t) = \pm 1, \quad \theta_{,y}(\pm 1, t) = 0, \quad \sigma(\pm 1, t) = 0 \tag{7}$$

and a suitable set of initial conditions. Equations (1) and (2) express the balance of linear momentum and internal energy, respectively. Herein v is the velocity of a material particle, l is a material characteristic length, θ is the temperature change of the material particle from that in the reference configuration, and s and σ may be interpreted as the shear stress and the dipolar shear stress, respectively. A superimposed dot indicates material time differentiation, and a comma followed by y signifies partial differentiation with respect to y. The nondimensional variables are related to their dimensional (barred) counterparts as follows:

$$\begin{aligned}
&y = \bar{Y}/H, \quad t = \bar{t}\dot{\gamma}_0, \quad \dot{\gamma} = v_{,y}, \quad \dot{d} = v_{,yy}, \quad \dot{\gamma} = \dot{\gamma}_e + \dot{\gamma}_p, \quad \dot{d} = \dot{d}_e + \dot{d}_p, \\
&v = \bar{v}/H\dot{\gamma}_0, \quad s = \bar{s}/\kappa_0, \quad \sigma = \bar{\sigma}/\bar{l}\kappa_0, \quad \theta = \bar{\theta}\bar{\rho}\bar{c}^2/\kappa_0, \\
&\gamma = \bar{\gamma}, \quad d = \bar{d}H, \quad \dot{\gamma}_p = \dot{\bar{\gamma}}_p/\dot{\gamma}_0, \quad \dot{d}_p = \dot{\bar{d}}_p H/\dot{\gamma}_0, \quad \Lambda = \bar{\Lambda}\kappa_0/\dot{\gamma}_0.
\end{aligned} \tag{8}$$

Besides m, n, and ψ_0, there are six other nondimensional parameters, which are related to their dimensional (barred) counterparts as follows:

$$\begin{aligned}
&a = \bar{a}\kappa_0/\bar{\rho}\bar{c}^2, \quad b = \bar{b}\dot{\gamma}_0, \quad k = \bar{k}/\bar{\rho}\bar{c}^2\dot{\gamma}_0 H^2, \quad l = \bar{l}/H, \\
&\mu = \bar{\mu}/\kappa_0, \quad \rho = \bar{\rho}H^2\dot{\gamma}_0^2/\kappa_0.
\end{aligned} \tag{9}$$

In eqns (8) and (9), $\dot{\gamma}_0 = \bar{v}(H, \bar{t})/H$ is the average applied strain rate between the boundaries $\bar{Y} = \pm H$, and κ_0 is the yield stress in a reference quasistatic test.

The constitutive relations (3)–(6) give one possible model of viscoplastic materials.

Equation (6) implies that the plastic parts, Δs and $\Delta\sigma/l$, of the strain rate and the dipolar strain rate vanish when

$$(s^2 + \sigma^2)^{1/2} \leq \left(1 + \frac{\psi}{\psi_0}\right)^n (1 - a\theta). \tag{10}$$

The material parameters ψ_0 and n describe the strain hardening of the material, a the thermal softening, and b and m the strain-rate sensitivity of the material.

We presume that the initial values of θ, s, and ψ are symmetric and the initial values of v and σ are antisymmetric in y and seek solutions of eqns (1) through (6) with the same symmetry. Thus, the problem is to be studied over the spatial domain [0,1] and the boundary conditions become

$$v(0,t) = 0, \quad \theta_{,y}(0,t) = 0, \quad \sigma(0,t) = 0, \tag{11}$$

$$v(1,t) = 1, \quad \theta_{,y}(1,t) = 0, \quad \sigma(1,t) = 0. \tag{12}$$

For the initial conditions we take

$$\begin{aligned} &v(y,0) = y, \quad \sigma(y,0) = 0, \quad \psi(y,0) = \tilde{\psi}_0, \\ &\theta(y,0) = \tilde{\theta}_0 + \tilde{\theta}(y), \\ &s(y,0) = s_0 = \left(1 + \frac{\psi_0}{\psi_0}\right)^n (1 + b\Delta\tilde{s}_0)^m (1 - a\theta(y,0)). \end{aligned} \tag{13}$$

The values of $\tilde{\theta}_0$, $\tilde{s}_0$, and $\tilde{\psi}_0$ are such that during homogeneous deformations of the block the shear stress $\tilde{s}_0$ and the strain corresponding to $\tilde{\psi}_0$ lie on the shear stress–shear strain curve for the material. Δ in eqn (13)$_3$ is given by eqn (6), with $\theta = \tilde{\theta}_0$, $s = \tilde{s}_0$, $\psi = \tilde{\psi}_0$, and $\sigma = 0$. The function $\tilde{\theta}$ describes the aberration in the initial temperature distribution and will result in nonhomogeneous deformations of the body.

III. NUMERICAL INTEGRATION OF GOVERNING EQUATIONS

With the auxiliary variables

$$u = v_{,y}, \quad g = \theta_{,y}, \quad p = \sigma_{,y}, \tag{14}$$

we rewrite eqns (1)–(4) as

$$\dot{v} = \frac{1}{\rho}(s - lp)_{,y}, \tag{15}$$

$$\dot{\theta} = kg_{,y} + \Delta(s^2 + \sigma^2), \tag{16}$$

$$\dot{s} = \mu(u - \Delta s), \tag{17}$$

$$\dot{\sigma} = l\mu\left(u_{,y} - \frac{\Delta}{l}\sigma\right). \tag{18}$$

Thus, only first-order spatial derivatives of the unknowns v, θ, s, σ, u, g, and p appear in the governing equations. Let H^1 denote the space of functions defined on [0,1] the square of whose first-order derivative is integrable over [0,1]. We approximate the unknown functions v, θ, s, etc. by linear combination of the finite element basis functions $\{\phi_i(y), i = 1,2, \ldots, N\}$ in an N-dimensional subspace of H^1. For example,

$$v(y,t) = v_i(t)\phi_i(y). \tag{19}$$

Throughout the article, a repeated index implies summation over the range of the index. Using Galerkin's method (e.g., see BECKER *et al.* [1981]) we thus reduce eqns (14) through (18) to the following set of equations:

$$M_{ij}u_i = -Q_{ij}v_i, \quad M_{ij}g_i = -Q_{ij}\theta_i, \quad M_{ij}p_i = -Q_{ij}\sigma_i, \tag{20}$$

$$M_{ij}\dot{v}_i = -\frac{1}{\rho}A_{ij}s_i + \frac{l}{\rho}Q_{ij}p_i, \quad M_{ij}\dot{\theta}_i = -kQ_{ij}g_i + \Delta_i P_{ij}, \tag{21}$$

$$M_{ij}\dot{s}_i = \mu M_{ij}u_i - \mu\Delta_i s_k R_{ijk}, \quad M_{ij}\dot{\sigma}_i = -\mu l\tilde{Q}_{ij}u_i - \mu\Delta_i\sigma_k R_{ijk}, \tag{22}$$

where

$$M_{ij} = \int_0^1 \phi_i\phi_j\,dy = M_{ji}, \quad Q_{ij} = \int_0^1 \phi_i\phi_{j,y}\,dy, \tag{23}$$

$$\tilde{Q}_{ij} = Q_{ij} - (\phi_i\phi_j)|_0^1, \tag{24}$$

$$R_{ijk} = \int_0^1 \phi_i\phi_j\phi_k\,dy = R_{ikj} = R_{kij}, \tag{25}$$

$$P_{ij} = \int_0^1 \phi_i\phi_j(s^2 + \sigma^2)\,dy = P_{ji}. \tag{26}$$

We note that because of the nonlinear dependence of P_{ij} and Δ upon s, σ, ψ, and θ, the coupled set of ordinary differential eqns (20)–(22) is not that easy to integrate. The matrices M_{ij}, Q_{ij}, $\tilde{Q}_{ij}$, R_{ijk}, and P_{ij} have been evaluated by using the linear basis functions. Also, $v_i(t)$ denotes the velocity of node i at time t.

We use the Crank-Nicolson method to integrate eqns (20)–(22), with respect to time t. In it, eqns (20)–(22), assumed to hold at time $(t + \Delta t/2)$, are used to predict the values of v, θ, s, σ, g, p, u, and ψ at time $(t + \Delta t)$ from a knowledge of their values at time t. This is accomplished by approximating $\dot{\theta}_i(t + \Delta t/2)$ by $(\theta_i(t + \Delta t) - \theta_i(t))/\Delta t$, $\theta_i(t + \Delta t/2)$ by $(\theta_i(t + \Delta t) + \theta_i(t))/2$, and so forth and by first evaluating the nonlinear terms on the right-hand side of eqns (20)–(22) at time t. The resulting system of linear algebraic equations is solved for $v_i(t + \Delta t)$, etc., the right-hand side in eqns (20)–(22) is now evaluated at time $(t + \Delta t/2)$, and the system of equations is solved again for $v_i(t + \Delta t)$ etc. This iterative process is continued until at each nodal point,

$$\left|\frac{\Delta v}{v} + \frac{\Delta\theta}{\theta} + \frac{\Delta s}{s} + \frac{\Delta\psi}{\psi}\right| + \Delta\sigma + \Delta g + \Delta p + \Delta u \leq \epsilon \tag{27}$$

where the subscript i has been dropped from v_i and elsewhere, Δv denotes the difference between the newly found value of v and that used to compute the right-hand side in eqns (20)–(22), and ϵ is a preassigned small number. The initial conditions (13) were used to find $v_i(0)$ and so forth.

IV. COMPUTATION AND DISCUSSION OF RESULTS

In order to compute numerical results, the following values of various nondimensional parameters that correspond to a typical hard steel and the average applied strain rate $\dot{\gamma}_0 = 500\ \text{sec}^{-1}$ were chosen.

$$\rho = 3.928 \times 10^{-5}, \quad k = 3.978 \times 10^{-3}, \quad a = 0.4973, \quad \mu = 240.3,$$

$$n = 0.09, \quad \psi_0 = 0.017, \quad b = 5 \times 10^{6}, \quad m = 0.025.$$

For homogeneous deformations of the block, the peak (marked as point P in Fig. 1) in the shear stress–shear strain curve occurs at a strain of 0.093. The uniform temperature $\theta_0 = 0.1003$ in the block when $\gamma = 0.0692$, corresponding to the point I in Fig. 1, was perturbed by adding a smooth temperature bump

$$\tilde{\theta}(y) = \Delta\theta_0(1 - y^2 - y_0^2)^p e^{-a(y^2 - y_0^2)}, \tag{28}$$

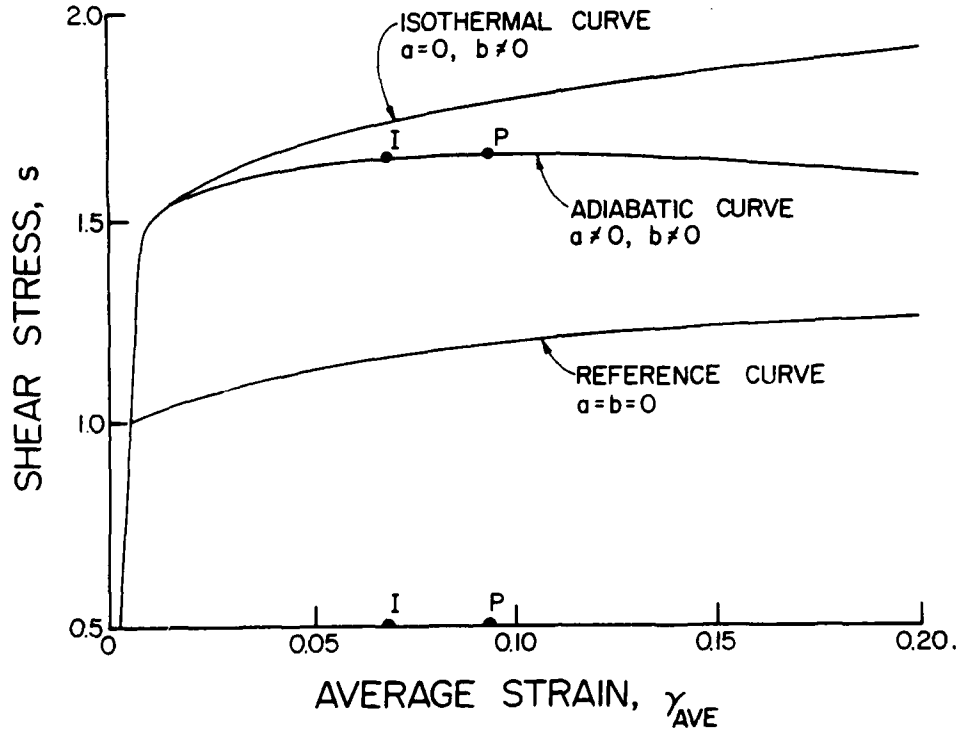

Fig. 1. Average shear stress–average shear strain curve for a typical steel.

and the resulting initial-boundary-value problem was solved by using the aforementioned method. The domain was divided into either 20 uniform subdomains (usually called finite elements) or 20 nonuniform subdomains, with nodes at 0, 0.0025, 0.01, 0.0225, 0.04, 0.0625, 0.09, 0.1225, 0.160, 0.2025, 0.2500, 0.3025, 0.360, 0.4225, 0.490, 0.5625, 0.640, 0.7225, 0.81, 0.9025, and 1.0. The two temperature perturbations for $\Delta\theta_0 = 0.1$, $p = 9$, $\alpha = 5$ and for $\Delta\theta_0 = 0.1$, $p = 2$, $\alpha = 1$ are shown in Fig. 2. For nonpolar materials, Fig. 3 depicts the growth of the central plastic strain rate in time for the two subdivisions of the domain. Numerical experiments with different values of Δt indicated that $\Delta t = 5 \times 10^{-6}$ gave accurate results. All of the results presented herein are for this value of Δt and $\epsilon = 0.01$. Unless otherwise noted, the nonuniform grid has been used. WRIGHT and BATRA [1986] gave a heuristic reasoning to explain that the pla-

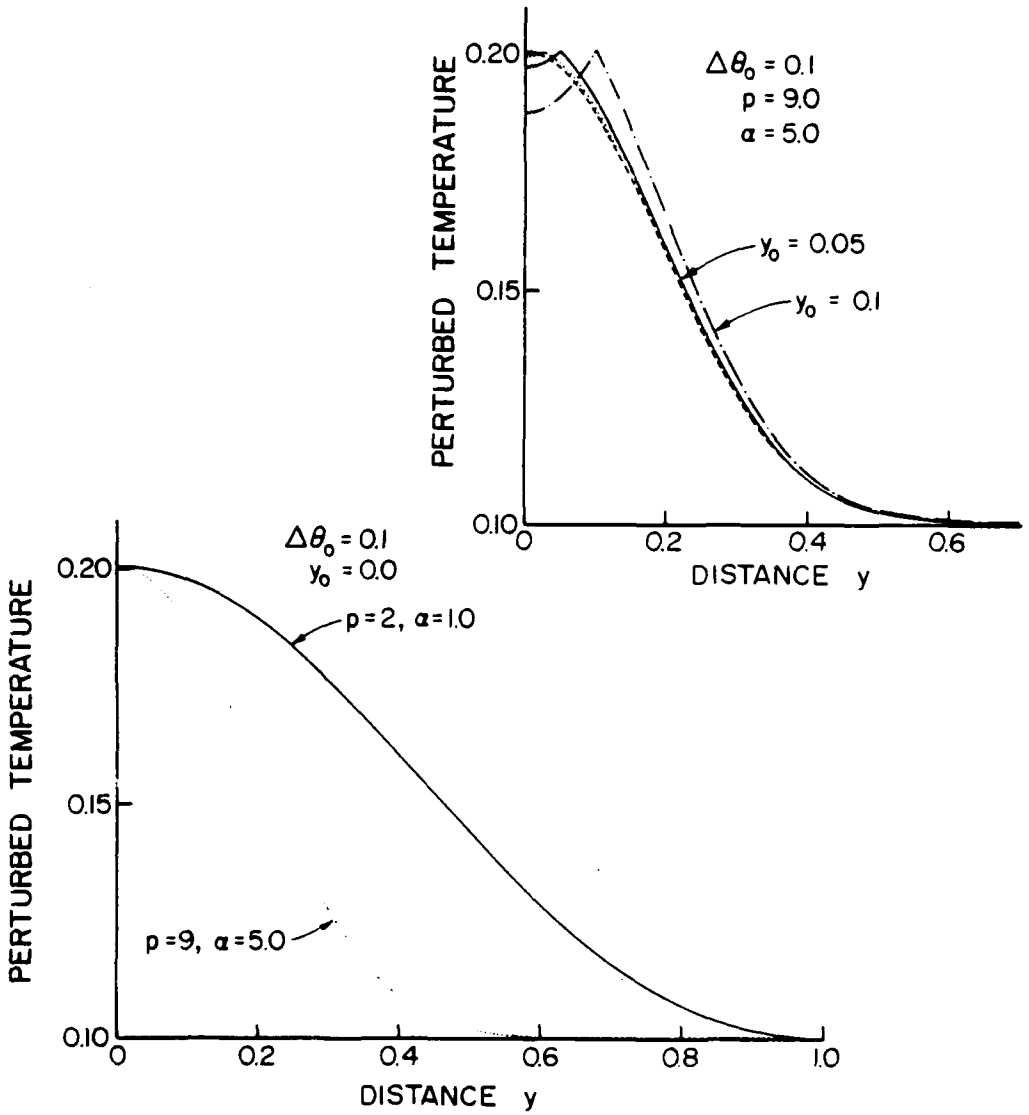

Fig. 2. Temperature perturbations

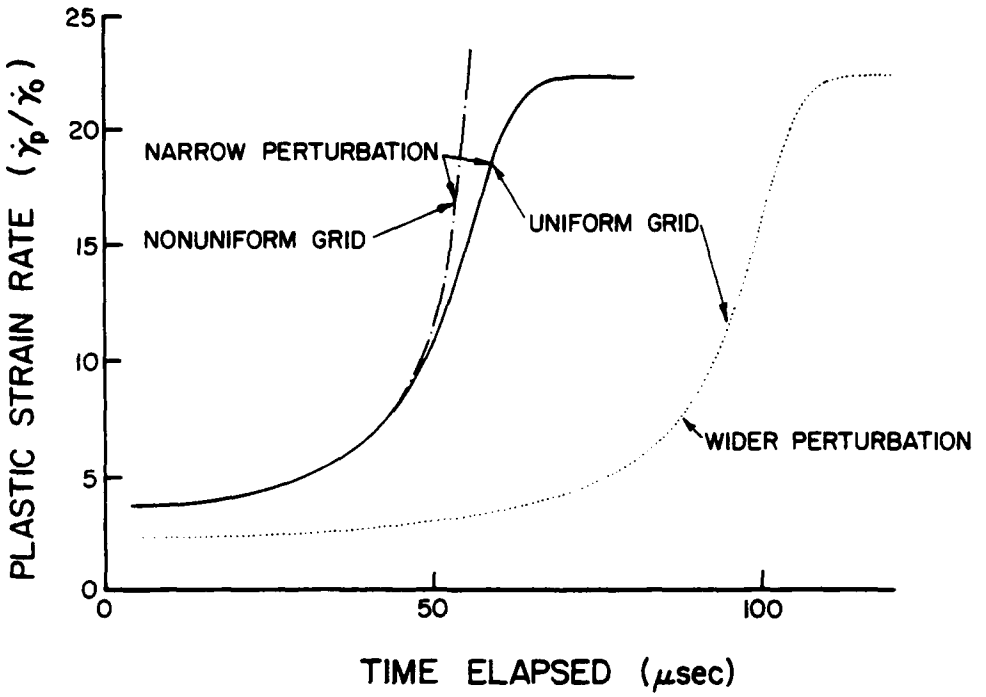

Fig. 3. Central plastic strain rate vs. elapsed time.

teau was formed because of the coarse mesh. The plot in Fig. 2 clearly proves that. Also, for the wider perturbation the rate of growth of the central plastic strain rate is quite a bit slower. Whereas for the narrower perturbation the shear band is formed when the average strain in the block corresponds to the point just past the peak in the shear stress–shear strain curve, the broader perturbation results in the formation of the band well past the peak in the average shear stress–average shear strain curve, which occurs at $t = 47.6$ μsec after the temperature field was perturbed. That a band is indeed formed for the wider perturbation should be clear from the plot of Fig. 4. It is apparent that the rapidly deforming region progressively narrows down to the one close to the center. The width of the rapidly deforming region is narrower for the finer mesh. Whether we have obtained the final band width or not is not quite clear yet, since we have not experimented with other fine meshes. Figure 5 depicts how the central shear stress changes in time. It decreases at a very slow rate and essentially follows the average shear stress–shear strain curve. It stays nearly uniform throughout the specimen. Numerical instabilities developed for values of time t a little beyond the one up to which results are plotted here. These can be due to the improper size of the time increment and/or to the mesh size, among other factors. Efforts are now under way to overcome these and to extend calculations for longer values of time.

Figures 6 and 7 depict the effect of the amplitude $\Delta\theta_0$ of the perturbation upon the growth of the central plastic strain rate for simple and dipolar materials with $l = 0.01$. Obviously, for larger amplitudes of the perturbation, the shear band is formed well before the peak in the average shear stress–average shear strain curve is reached. A comparison of the results presented in Figs. 3, 6, and 7 clearly brings out the stiffening caused by the inclusion of the dipolar stresses.

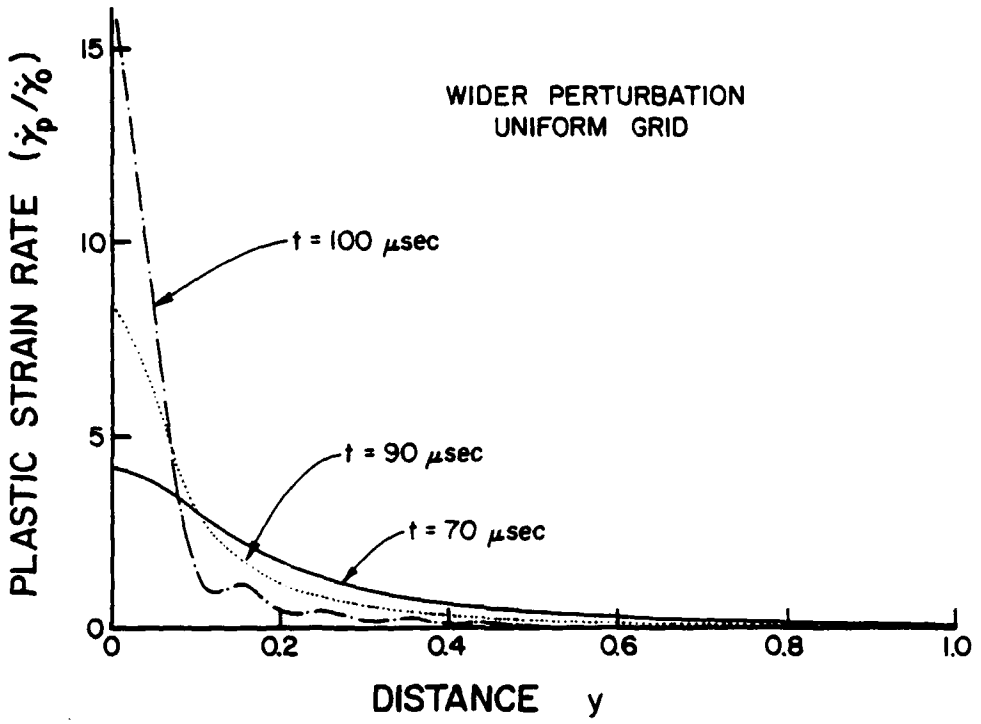

Fig. 4. Plastic strain rate distribution in a finite block of material at various times as a shear band forms.

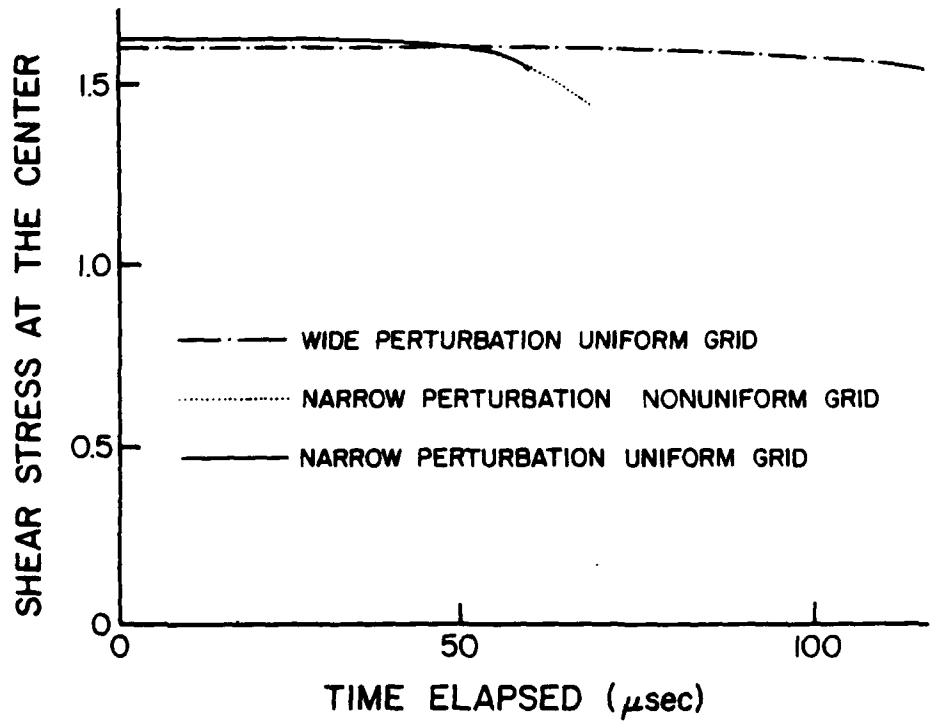

Fig. 5. Central shear stress vs. elapsed time.

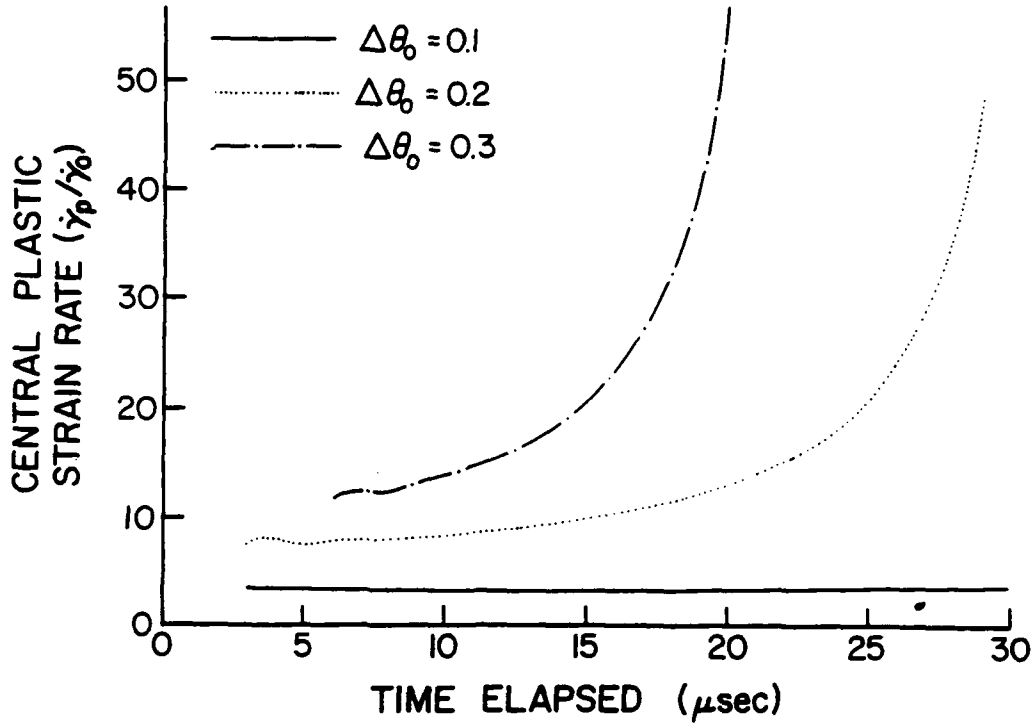

Fig. 6. Central plastic strain rate vs. elapsed time for nonpolar materials.

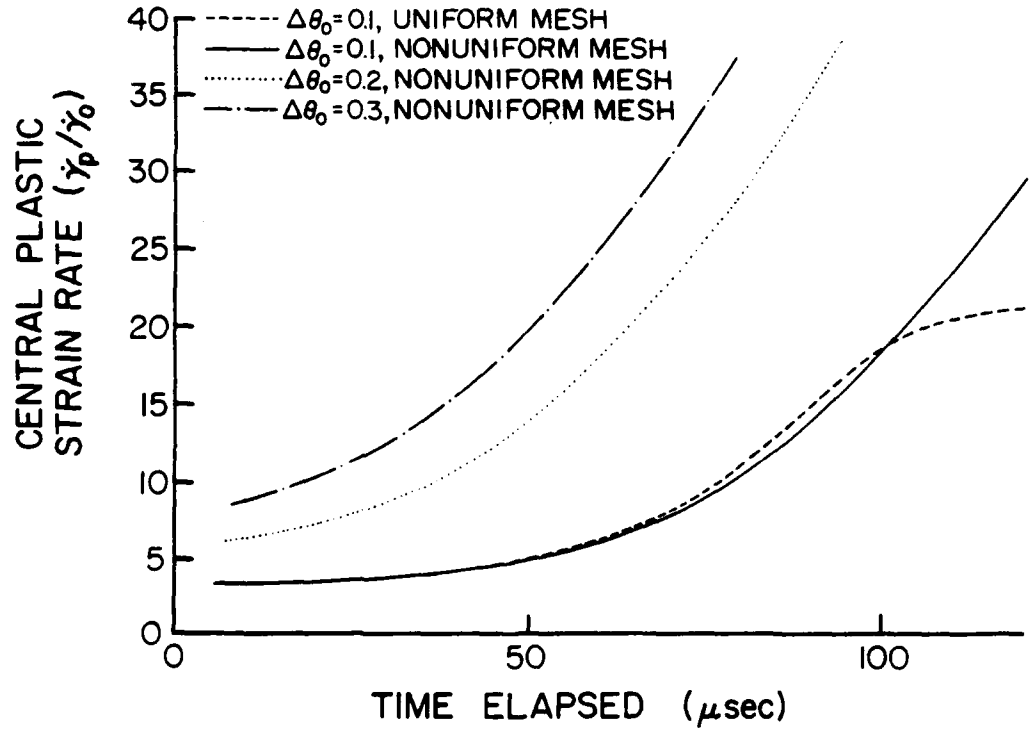

Fig. 7. Central plastic strain rate vs. elapsed time for dipolar materials ($l = 0.01$).

In order to understand the interaction among shear bands, we introduced a perturbation in the temperature centered at different points along the thickness of the slab. Because of the symmetry of θ about the horizontal axis, this amounts to introducing two aberrations symmetrically placed about the center line $y = 0$. The hypothesis here is that if the resulting nonhomogeneous fields, such as the plastic strain rate, temperature, and the plastic strain, eventually peak out at the center of the slab, then the two bands have coalesced; otherwise they grow independently. Perturbations in the temperature centered at $y = 0.025$, $y = 0.05$, and $y = 0.1$ but $\Delta\theta_0 = 0.1$ were introduced and the ensuing initial-boundary-value problems were solved. Figures 8 and 9 show the distribution of the plastic strain rate through the thickness of the slab for simple and dipolar materials, respectively. For simple materials (Fig. 8), the two bands initially centered at $y = \pm 0.025$ coalesce but the ones centered at $\pm .05$ and $\pm .1$ grow independently of each other. The rate of growth of the peak strain rate (not the strain rate at $y = 0$) is considerably less as compared to that when either only one band appears at $y = 0$ or two bands initially centered at $y = \pm .025$ merge and grow as a single band. For dipolar materials, the bands coalesce in all three cases. Recall that the material characteristic length is $\frac{1}{20}$ of the distance between the bands originating at $y = \pm 0.1$.

The distribution of the dipolar stress across the slab is plotted in Fig. 10. Because of the boundary conditions $\sigma(0, t) = \sigma(1, t) = 0$ and the fact that the dipolar stress for the elastic problem is proportional to the curvature, the maximum value of σ cannot occur at the center of the slab. Note that σ is very small as compared to 1.0, whereas s is gen-

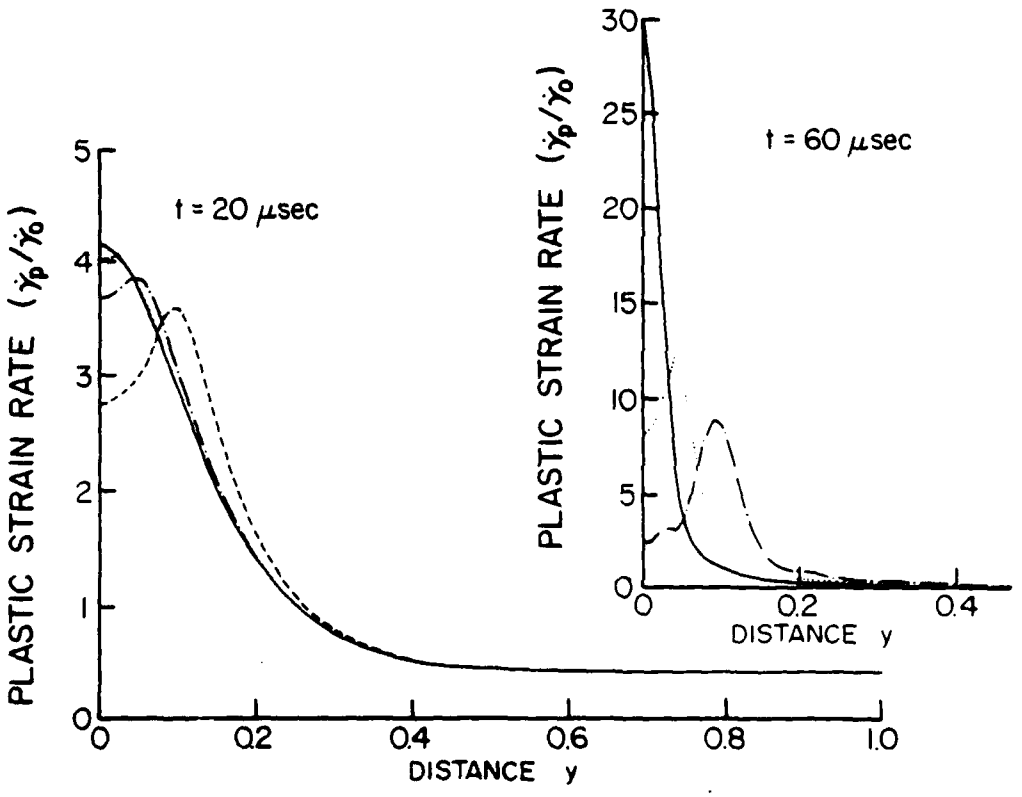

Fig. 8. Plastic strain rate distribution for four perturbations centered at different points (nonpolar materials).

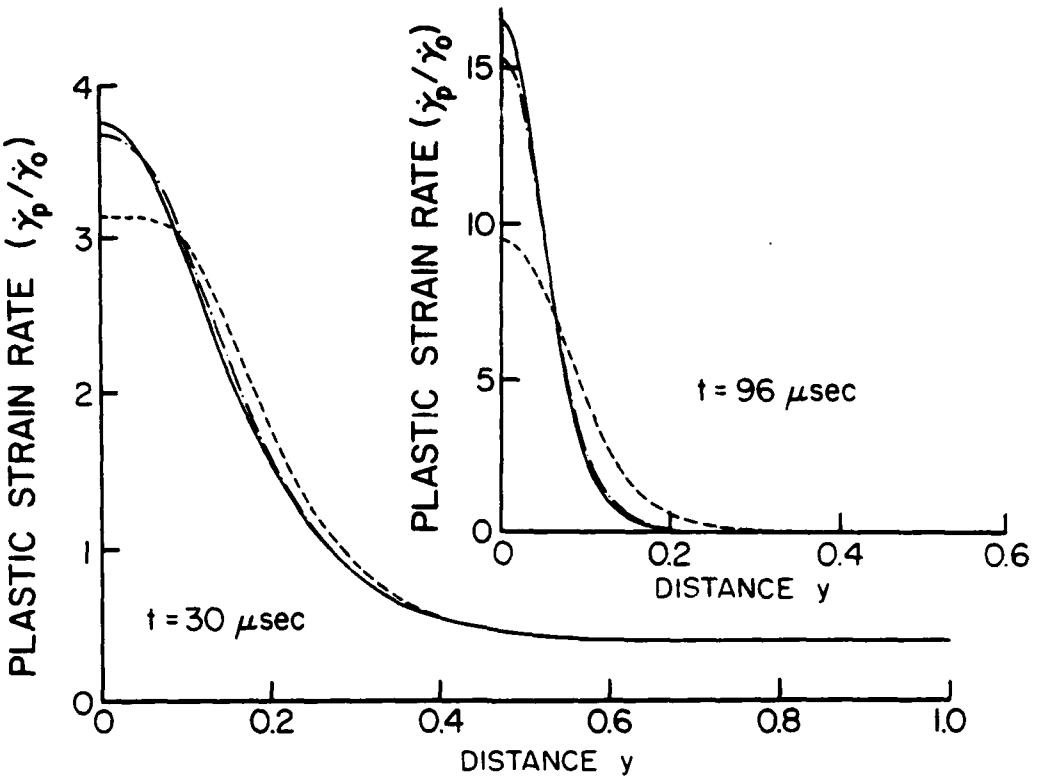

Fig. 9. Plastic strain rate distribution for four perturbations centered at different locations (dipolar materials, $l = 0.01$).

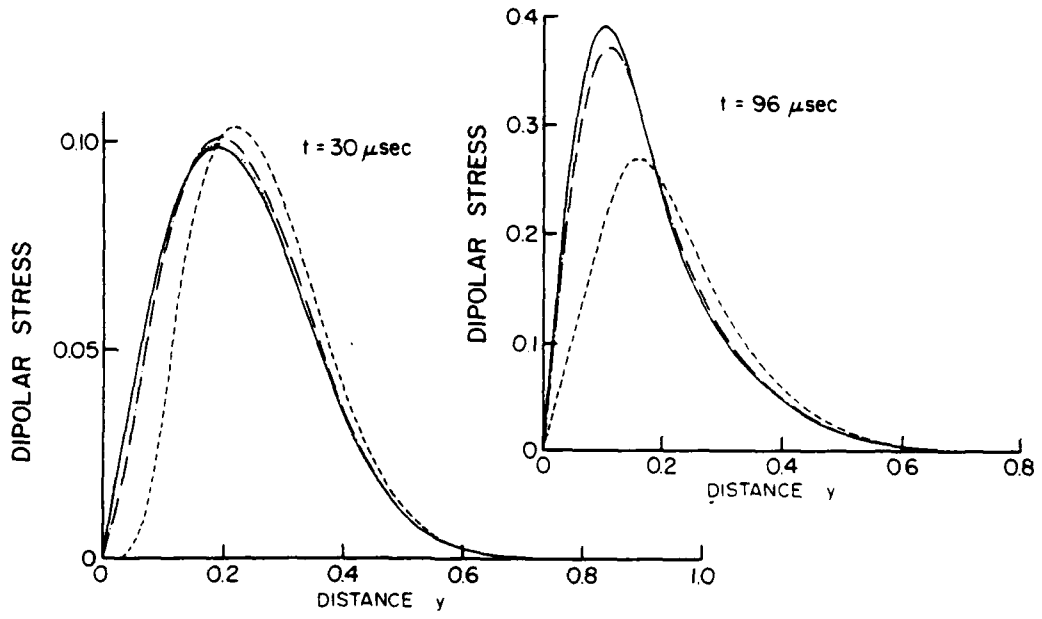

Fig. 10. Dipolar stress distribution for four perturbations centered at different locations ($l = 0.01$).

erally greater than or equal to 1.0. At a point where $\dot{\gamma}_p \neq 0$, $\dot{d}_p \neq 0$, the dipolar stress has negligible contribution to the effective stress $(s^2 + \sigma^2)^{1/2}$ that determines whether $\Lambda > 0$ or $\Lambda = 0$ at that point.

V. CONCLUSION

It is shown that the constitutive model proposed by WRIGHT and BATRA [1986] does predict adiabatic shear bands in a block undergoing simple shearing. The rate at which a band grows depends upon the strength of the inhomogeneity, herein modeled as a perturbation in the otherwise uniform temperature within the block. Perturbations of larger amplitude result in the formation of a shear band even before the peak in the shear stress–shear strain curve is reached. Also, a wider perturbation results in the shear strain localization at a lower rate as compared to the narrow perturbation, both being of the same amplitude. The inclusion of dipolar effects results in a very stiffening effect in the sense that the formation of bands is delayed considerably as compared to that in simple materials. In addition, two bands that would grow independently in a simple material coalesce when dipolar effects are included. Of course, the minimum distance between two shear bands to grow independently of each other will possibly depend upon, among other factors, the value of the material characteristic length l.

Acknowledgements—The author is deeply indebted to Dr. Thomas W. Wright of the U.S. Army Ballistic Research Laboratory for many useful discussions on the subject. This work was supported by the U.S. Army Research office through contract ARO-DAAG29-85-K-0238 to the University of Missouri-Rolla.

REFERENCES

1944 ZENER, C., and HOLLOMAN, J.H., "Effect of Strain Rate on Plastic Flow of Steel," J. Appl. Phys., **15**, 22.

1964 RECHT, R.F., "Catastrophic Thermoplastic Shear," ASME J. Appl. Mech., **31**, 189.

1968 GREEN, A.E., MCINNIS, B.C., and NAGHDI, P.M., "Elastic-Plastic Continua with Simple Force Dipole," Int. J. Eng. Sci., **6**, 373.

1973 CULVER, R.S., "Thermal Instability Strain in Dynamic Plastic Deformation," in RHODE, R.W. *et al.* (eds.), Metallurgical Effects at High Strain-Rates, Plenum Press, New York, 519-530.

1980 CLIFTON, R.J., "Material Response to Ultra High Loading Rates," NRC National Material Advisory Board (U.S.) Report 356.

1980 COSTIN, L.S., CRISMAN, E.E., HAWLEY, R.H., and DUFFY, J., "On the Localization of Plastic Flow in Mild Steel Tubes Under Dynamic Torsional Loading" in HARDING, J. (ed.), Mechanical Properties at High Rates of Strain, Proc. 2nd Oxford Conf. Inst. Phys., London, 90-100.

1980 ERLICH, D.C., CURRAN, D.R. and SEAMAN, L., "Further Development of a Computational Shear Band Model," SRI Rept. AMMRC TR 80-3.

1981 BAI, Y.L., "A Criterion for Thermoplastic Shear Instability," in MEYERS, M.A. and MURR, L.E. (eds.), Shock Waves and High Strain Rate Phenomenon in Metals, Plenum Press, New York, 277-283.

1981 BECKER, E.B., CAREY, G.F., and ODEN, J.T., Finite Elements: An Introduction, Vol. 1, Prentice-Hall, Englewood Cliffs, N.J.

1981 MOSS, G.L., "Shear Strain, Strain Rates, and Temperature Changes in Adiabatic Shear Bands," in MEYERS, M.A. and MURR, L.E. (eds.), Shock Waves and High Strain Rate Phenomenon in Metals, Plenum Press, New York, 299-312.

1981 OLSON, G.B., MESCALL, J.F., and AZRIN, M., "Adiabatic Deformation and Strain Localization," in MEYERS, M.A. and MURR, L.E. (eds.), Shock Waves and High Strain Rate Phenomenon in Metals, Plenum Press, New York, 221-247.

1981 STAKER, M.R., "The Relation between Adiabatic Shear Instability Strain and Material Properties," Acta Met., **29**, 683.

1983 BURNS, T.J., "Approximate Linear Stability Analysis of a Model of Adiabatic Shear Band Formation," SAND 83-1907, Sandia National Laboratories, Albuquerque, New Mexico.

1983 JOHNSON, G.R., HOLEGTEDT, J.M., LINDHOLM, U.S., and NAGY, A., "Response of Various Metals to Large Torsional Strains over a Large Range of Strain Rates Part I: Ductile Metals," ASME J. Eng. Materials Technol., **105**, 48.

1983 LINDHOLM, U.S., and JOHNSON, G.R., "Strain-Rate Effects in Metals at Large Strain Rates," in MESCALL, J. and WEISS, V. (eds.), Material Behavior Under High Stresses and Ultrahigh Loading Rates, Plenum Press, New York, 61–79.

1983 MERZER, A.M., "Modeling of Adiabatic Shear Band Development from Small Imperfections," J. Mech. Phys. Sol., **30**, 323.

1983 SHAWKI, T.G., CLIFTON, R.J., and MAJDA, G., "Analysis of Shear Strain Localization in Thermal Visco-Plastic Materials," ARO Report DAAG 29-81-K-0121 3.

1984 WU, F.H., and FREUND, L.B., "Deformation Trapping due to Thermoplastic Instability in One-Dimensional Wave Propagation," J. Mech. Phys. Sol., **32**, 119.

1985a WRIGHT, T.W., and BATRA, R.C., "The Initiation and Growth of Adiabatic Shear Bands," Int. J. Plasticity, **1**, 205.

1985b WRIGHT, T.W., and BATRA, R.C., "Further Results on the Initiation and Growth of Adiabatic Shear Bands," J. Physique, **46**(C5), 323.

1986 WRIGHT, T.W., and BATRA, R.C., "Adiabatic Shear Bands in Simple and Dipolar Plastic Materials," in KAWATA, K. (ed.), Proc. IUTAM Symposium on Macro- and Micro-mechanics of High Velocity Deformation and Fracture, Springer-Verlag, Berlin-Heidelberg-New York (in press).

Department of Engineering Mechanics
University of Missouri-Rolla
Rolla, MO 65401-0249, USA

(*Received* 3 *June* 1986; *In final revised form* 22 *September* 1986)

Int. J. Solids Structures Vol. 23, No. 10, pp. 1435–1446, 1987
Printed in Great Britain

0020–7683/87 $3.00 + .00
© 1987 Pergamon Journals Ltd

EFFECT OF MATERIAL PARAMETERS ON THE INITIATION AND GROWTH OF ADIABATIC SHEAR BANDS

R. C. BATRA
Department of Engineering Mechanics, University of Missouri–Rolla, Rolla, MO 65401-0249, U.S.A

(*Received* 3 *December* 1986; *in revised form* 14 *April* 1987)

Abstract—The thermomechanical problem involving simple shearing of a finite slab made of an isotropic and viscoplastic material is studied with the objective of finding the effect of the strain hardening parameter, strain-rate hardening parameters, thermal softening coefficient and thermal conductivity on the initiation and growth of adiabatic shear bands. The body is placed in a hard loading device, i.e. the velocity is prescribed at its top and bottom surfaces. A shear band is presumed to have formed if the addition of a perturbation in the temperature at the onset of plastic flow results in a localization of the shear strain. The critical strain at which the band begins to form is found and its dependence on various material parameters is investigated.

INTRODUCTION

IN 1944 Zener and Hollomon[1] recognized the destabilizing effect of thermal softening in reducing the slope of the stress–strain curve in nearly adiabatic deformations. They postulated that a negative slope of the stress–strain curve implies an intrinsic instability of the material. Thus the strain at which the shear strain localization may initiate corresponds to the peak in the stress–strain curve. They observed 32 μm wide shear bands in a steel plate punched by a standard die and estimated the maximum strain in the band to be 100. Recht[2], assuming that the instability occurs at the peak in the stress–strain curve and this curve is independent of the strain rate, derived values of strain rate necessary to produce shear strain localization and compared these values for different materials. Staker[3] used the same instability criterion but included the dependence of the flow stress upon strain rate also. Assuming parabolic strain and strain-rate hardening laws, he concluded that important material parameters are the specific heat, slope of the temperature dependence of the flow stress, and parameters indicating the strain hardening capacity of the material. The thermal conductivity, yield strength and strain-rate sensitivity do not enter in as a first-order effect.

Instead of presuming that the material becomes unstable at a stress maximum, Clifton[4] and Bai[5] studied the growth of infinitesimal periodic perturbations superimposed on a body deformed by a finite amount in simple shear. Both investigators included the effect of strain hardening, strain-rate sensitivity, thermal softening and heat conduction. Bai also included the effect of inertia forces. Bai's instability criterion is essentially insensitive to strain-rate hardening parameters and for a parabolic type strain hardening material gives the same value of critical strain as that derived by Staker[3]. Burns[6] used a dual asymptotic expansion to account for the time dependence of the homogeneous solution in the analysis of the growth of superimposed infinitesimal perturbations. He showed that the growth rate of small perturbations is controlled by the ratio of the slope of the homogeneous stress vs strain curve to the rate of change of the plastic flow stress with respect to the strain rate. However, this growth rate was not large enough for Litonski's[7] constitutive relation to account for the experimental observations of Costin *et al.*[8]. Costin *et al.* observed 370–500 μm wide shear bands during dynamic torsion tests involving strain rates of 500 s^{-1} on short specimens of 1018 cold rolled steel. Similar observations on twelve ductile materials have been reported by Johnson *et al.*[9] and Lindholm and Johnson[10].

Merzer[11], by using a material model due to Bodner and Partom[12], studied the problem of twisting of a thin tubular specimen having a notch in its periphery. He concluded

that the thermal conductivity played a key role in determining the width of the shear band. On the other hand Wu and Freund[13], by using a different material model, studied wave propagation in an infinite medium and concluded that the thermal conductivity has essentially no effect on the width of a shear band.

Clifton *et al.*[14] used both numerical and perturbation techniques to study the initiation and growth of shear bands. They used a power law model and reported that the thermal conductivity had virtually no effect on their results. They did not compute the band width explicitly. Also the rate of growth of the nonuniformity increased strongly with decreasing strain-rate sensitivity.

Recently, Wright and Batra[15–17] and Batra[18] described the results of computations that simulate the formation of a shear band from a local temperature inhomogeneity in simple and dipolar materials. The constitutive relation was derived by modifying the dipolar theory of Green *et al.*[19] to include rate effects. For simple materials this constitutive relation reduces to one that is very similar to that proposed by Litonski[7] and Lindholm and Johnson[10]. Whereas Litonski, and Lindholm and Johnson suggested constitutive relations valid for simple shearing deformation of a ductile material, that proposed by Wright and Batra is easily amenable to a general state of stress. Wright and Batra[15–17] and Batra[18] studied the simple shearing of a block made of an isotropic and viscoplastic material and perturbed the homogeneous solution by adding a temperature bump just prior to the occurrence of the peak stress. The stress field was calculated so that every material point was on the yield surface corresponding to its new temperature when all other variables were held fixed. The full set of non-linear coupled governing equations was solved numerically. In Ref. [18] Batra used a similar method to study the interaction among shear bands in simple and dipolar materials.

Herein, for simple materials, we study the effect of various material parameters on the initiation and growth of adiabatic shear bands by adding the temperature perturbation in the configuration when the body just starts deforming plastically. Since this point is far from the peak in the stress–strain curve, our results should reflect the dependence of the rate of growth of the perturbation upon the material parameter being changed. We should add that the complete set of coupled non-linear equations are solved numerically by the Galerkin–Crank–Nicolson method. The computed results show that for the problems studied in which the non-dimensional thermal length varied from 0 to 0.063, the thermal conductivity has no noticeable effect on the strain at which the shear strain localization occurs. In all but one of the cases studied, the stress–strain curve had a peak in it and a narrow region near the center eventually deformed very rapidly with the rest of the material essentially not deforming at all. For the exceptional case noted earlier, the combination of the values of material parameters was such that the stress–strain curve had no peak in it. In this case no localization of deformation occurred even when the amplitude of the initial temperature perturbation was increased to three times its value for other cases. This seems to confirm that the peaking out of stress is a necessary condition for the shearing deformation to localize.

FORMULATION OF THE PROBLEM

We study the simple shearing deformations of a semi-infinite, isotropic and viscoplastic body bounded by the planes $Y = \pm H$ and consider deformation fields of the type

$$x = X + u(Y, t), \qquad y = Y, \qquad z = Z, \qquad \theta = \theta(Y, t). \tag{1}$$

Thus, with respect to a rectangular Cartesian set of axes, (x, y, z) denote the current coordinates of a material point that occupied the place (X, Y, Z) in a stress-free reference configuration. The functions u and θ give, respectively, the displacement of the material point in the x-direction and its temperature change from that in the reference configuration. In the absence of body forces and external sources of heat, the balance of linear momentum

divided into 20 subdomains (finite elements) with nodes at 0, 0.0025, 0.01, 0.0225, 0.04, 0.0625, 0.09, 0.1225, 0.160, 0.2025, 0.2500, 0.3025, 0.3600, 0.4225, 0.4900, 0.5625, 0.6400, 0.7225, 0.8100, 0.9025, 1.0. The uniform time increment $\Delta t = 5 \times 10^{-6}$ was used in the Crank–Nicolson method.

The following values of material parameters that correspond to a typical hard steel were chosen:

$$\rho = 7860 \text{ kg m}^{-3}, \quad k = 49.216 \text{ W m}^{-1}\,^{\circ}\text{C}^{-1}, \quad \mu = 80 \text{ GPa},$$
$$\kappa_0 = 333 \text{ MPa}, \quad a = 0.00552\,^{\circ}\text{C}^{-1}, \quad c_v = 473 \text{ J kg}^{-1}\,^{\circ}\text{C}^{-1}, \quad (20)$$
$$m = 0.025, \quad n = 0.09, \quad \psi_0 = 0.017, \quad b = 10^4 \text{ s}.$$

For this choice of parameters, $\theta_0 = 89.6^{\circ}$C. Also we took $\dot{\gamma}_0 = 500 \text{ s}^{-1}$ and $H = 2.58$ mm.

As pointed out by Wright and Batra[15], implicit in eqns (16) are two relative length scales, namely a thermal length $(k/\rho c_v \dot{\gamma}_0 H^2)^{1/2}$ and viscous length $(b/H)(\kappa_0/\rho)^{1/2}$. The effect of a change in these as well as in the values of parameters describing thermal softening, work hardening, and rate hardening of the material is studied. The viscous length was varied by altering the value of the material parameter b while keeping the values of all other parameters unchanged. Figure 1 shows the shear stress, the temperature change and the plastic strain rate at the center vs the time elapsed. Since the average strain rate in the specimen is kept fixed at 500 s^{-1}, the average strain γ_{avg} plotted as abscissa in Fig. 1 and other figures is related to the elapsed time Δt in seconds by $\gamma_{avg} = 500\,\Delta t$. We note that the shear stress in the specimen was initially nonuniform. However, after a brief interval during which the field variables essentially regain their balance, the shear stress becomes uniform throughout the slab and stays uniform up to the time results plotted here. It is obvious from the stress–strain curves plotted in Fig. 1 that with the increase in the value of b the peak stress increases but this peak occurs at a lower value of average strain. The amount by which the peak moves to the left decreases with every 10 fold increase in the value of b suggesting that eventually an increase in the value of b will not affect the strain at which the peak stress occurs. The central plastic strain rate increases rather slowly first, but begins to increase rapidly as the peak in the stress–strain curve is reached and eventually increases

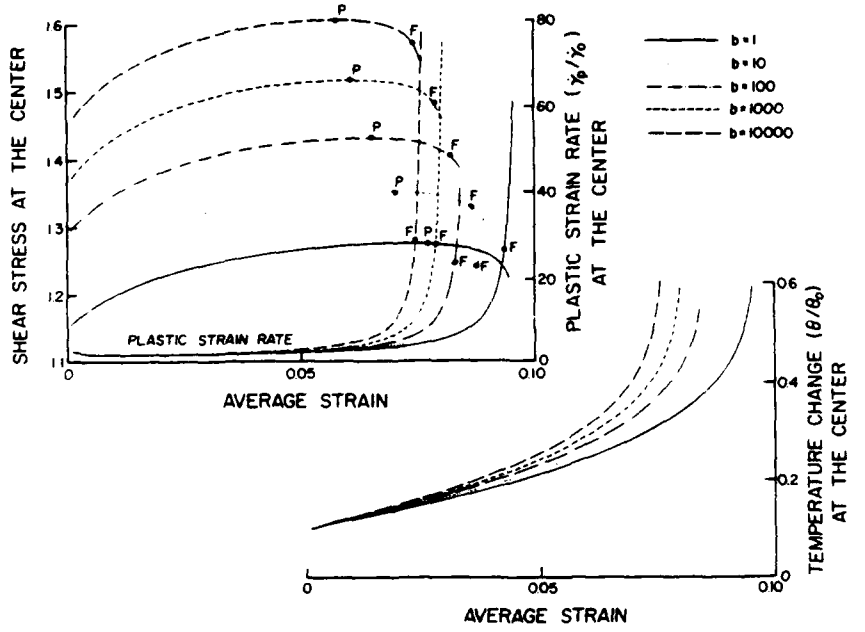

Fig. 1. Effect of the value of material parameter b on the evolution of the central stress, central plastic strain rate and the central temperature.

at an infinite rate when the average strain in the specimen is well past that corresponding to the peak stress. This point is indicated by F on the stress–strain curves. The temperature at the center first increases linearly but soon begins to increase at a faster rate and eventually grows extremely rapidly. Since the shear stress decreases once the peak is passed, the rate of increase of temperature is not as fast as the rate of increase of the plastic strain rate. For the same value of average strain, a higher value of b results in a higher value of θ. We should add that unlike the shear stress, the temperature, plastic strain, plastic strain rate, and particle velocity fields are not uniform throughout the thickness of the slab. Figure 2 depicts the cross-plots of the plastic strain rate, temperature change and the particle velocity for different values of b. The values of time elapsed or the average strain for different curves are not quite the same. This is due to the fact that computed results were printed for identical values of t but the explosive growth in central plastic strain rate occurs at different times. Except for a narrow region near the center, the temperature distribution within the specimen is unaffected by a change in the value of material parameter b. As expected the deformation has localized, and the majority of the block away from the center moves as a rigid body.

Following Wright[22] we define the width of a shear band as twice the distance of the point from the center where the value of the plastic strain rate drops to one-tenth of its maximum value at the center. We note that during the development of the shear band, the plastic strain rate is maximum at the center. At a time later than the one when a dramatic rise in the growth rate of the central plastic strain rate occurs, the value of the plastic strain rate at a node adjoining the center of slab becomes greater than that at the center. This is due to the grid being not as fine as is perhaps required for the proper resolution of the deformation field. Notwithstanding this shortcoming, one can still investigate the effect of the viscous length on the band width. For all five values of the viscous length, the band width came out to be 116 μm. In each case, the central plastic strain rate had reached a value of 80 times the applied average strain rate of 500 s^{-1}. Numerical experiments with a mesh that was finer near the center yielded the same value of the band width and gave a maximum value of the plastic strain rate at the center. We are currently developing a computer code that will refine the mesh adaptively and give a much better resolution of the deformation fields near the center of the slab.

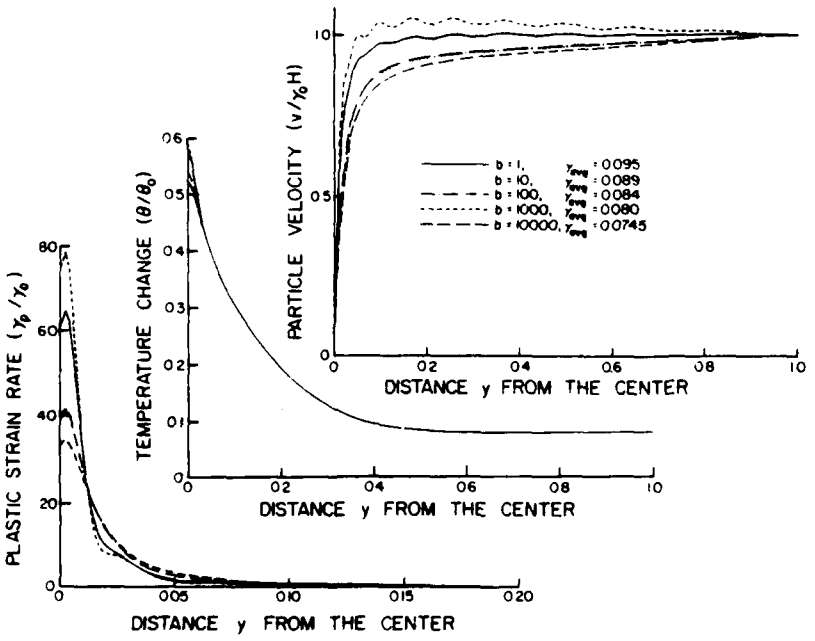

Fig. 2. Effect of the value of material parameter b on the distribution of particle velocity, temperature change and plastic strain rate within the specimen

and internal energy may be written as

$$\rho\ddot{u} = s_{,x} \tag{2}$$

$$\rho\dot{e} = s\dot{u}_{,x} - q_{,x}. \tag{3}$$

Here ρ is the mass density which stays constant since the deformations considered are isochoric and the effect of temperature changes on the mass density is being neglected, s is the shearing stress in the x-direction on a plane y = constant, e is the specific internal energy, q is the heat flux, a superimposed dot indicates material time derivative, and a comma followed by x signifies partial differentiation with respect to x. We assume that the shear strain has an additive decomposition

$$\gamma \equiv u_{,x} = \gamma_e + \gamma_p \tag{4}$$

and that a loading or yield function f exists such that

$$f(s, \theta, \dot{\gamma}_p) = \kappa \tag{5}$$

where f is a monotonically decreasing function in $\dot{\gamma}_p$ and κ is a measure of the work hardening of the material. The criterion for elastic and plastic loading is

$$f(s, \theta, 0) \leqslant \kappa, \quad \text{elastic} \tag{6}$$

$$f(s, \theta, 0) > \kappa, \quad \text{plastic}. \tag{7}$$

In the latter case, the sign of $\dot{\gamma}_p$ is the same as that of s and its absolute value can be found uniquely from eqn (5) because of the assumed monotonicity of f. The reader is referred to Wright and Batra[15, 17] for further discussion of the yield surface.

Here we make the following choice of constitutive functions

$$\rho e = \tfrac{1}{2}\mu\gamma_e^2 + \rho c_v\theta \tag{8}$$

$$q = -k\theta_{,x} \tag{9}$$

$$\kappa = \kappa_0\left(1 + \frac{\psi}{\psi_0}\right)^n \tag{10}$$

$$\kappa\dot{\psi} = s\dot{\gamma}_p \tag{11}$$

$$f = s/(1 - a\theta)(1 + b\dot{\gamma}_p)^m \tag{12}$$

where μ is a constant shear modulus, c_v is the specific heat at constant volume, k is the thermal conductivity, ψ is the plastic strain in a slow isothermal reference test for which the stress–strain curve (neglecting elastic strains) is given by eqn (10), parameter a describes the thermal softening of the material and material parameters b and m give its strain-rate sensitivity. From eqn (8) it follows by using standard thermodynamic arguments [17] that

$$s = \mu\gamma_e. \tag{13}$$

Therefore

$$\dot{s} = \mu(\dot{\gamma} - \dot{\gamma}_p). \tag{14}$$

Before stating the initial and boundary conditions we introduce non-dimensional variables (indicated by superimposed bars in eqn (15)) as follows:

$$y = H\bar{y}, \quad u = H\bar{u}, \quad s = \kappa_0\bar{s}, \quad \theta = \frac{\kappa_0}{\rho c_v}\bar{\theta} \equiv \theta_0\bar{\theta},$$

$$t = \frac{1}{\dot{\gamma}_0}\bar{t}, \quad \gamma = \bar{\gamma}, \quad \kappa = \kappa_0\bar{\kappa}, \quad \psi = \bar{\psi}, \quad \bar{v}H\dot{\gamma}_0 = v,$$

$$\bar{a} = a\theta_0, \quad \bar{b} = b\dot{\gamma}_0, \quad \bar{\rho} = \rho H^2\dot{\gamma}_0^2/\kappa_0, \quad \bar{k} = k_i/(\rho c_v\dot{\gamma}_0 H^2). \tag{15}$$

Here $\dot{\gamma}_0$ is the average strain rate imposed in the problem. Dropping the overbars, the complete set of equations in non-dimensional variables may be written as

$$\begin{aligned} \dot{v} &= \frac{1}{\rho}s_{,y} \\ \dot{\theta} &= k\theta_{,yy} + s\dot{\gamma}_p \\ \dot{s} &= \mu(v_{,y} - \dot{\gamma}_p) \\ \dot{\psi} &= s\dot{\gamma}_p\left(1 + \frac{\psi}{\psi_0}\right)^n \end{aligned} \tag{16}$$

$$\dot{\gamma}_p = \max\left[0, \left\{\left(\frac{s}{(1+\psi/\psi_0)^n(1-a\theta)}\right)^{1/m} - 1\right\}\frac{1}{b}\right].$$

Whereas we have assumed that all of the plastic work is converted into heat, some authors (e.g. Sulijoadikusumo and Dillon[20]) assume that only about 90% of the plastic work is transformed into heat. Farren and Taylor[21] found that in tensile experiments on steels, copper and aluminum, the heat rise represented 86.5, 90.5–92 and 95%, respectively, of the plastic work. In eqns (16) v is the particle velocity in the x-direction. The boundary conditions

$$v(\pm 1, t) = \pm 1, \quad \theta_{,y}(\pm 1, t) = 0 \tag{17}$$

ensure that the overall applied strain rate is $\dot{\gamma}_0$ and the deformations are adiabatic. For the initial conditions we take

$$v(y, 0) = y, \quad \psi(y, 0) = 0, \quad \theta(y, 0) = 0.1(1 - y^2)^n e^{-y^2} \tag{18a}$$

$$s(y, 0) = (1 - a\theta(y, 0))(1 + b)^m. \tag{18b}$$

Thus the initial perturbation in the temperature is introduced when the material just starts deforming plastically and the initial stress distribution is adjusted so that all of the material points are on their corresponding yield surfaces.

We seek solutions of eqns (16)–(18) such that v is antisymmetric in y, and s and θ are symmetric in y. Thus we can study the problem on the domain [0, 1] and replace boundary conditions (17) by

$$v(0, t) = 0, \quad \theta_{,y}(0, t) = 0, \quad v(1, t) = 1, \quad \theta_{,y}(1, t) = 0. \tag{19}$$

RESPONSE TO PERTURBATIONS

The details of integrating the governing equations (16) under side conditions (18) and (19) by the Galerkin–Crank–Nicolson method are given in Ref. [18]. The domain [0, 1] was

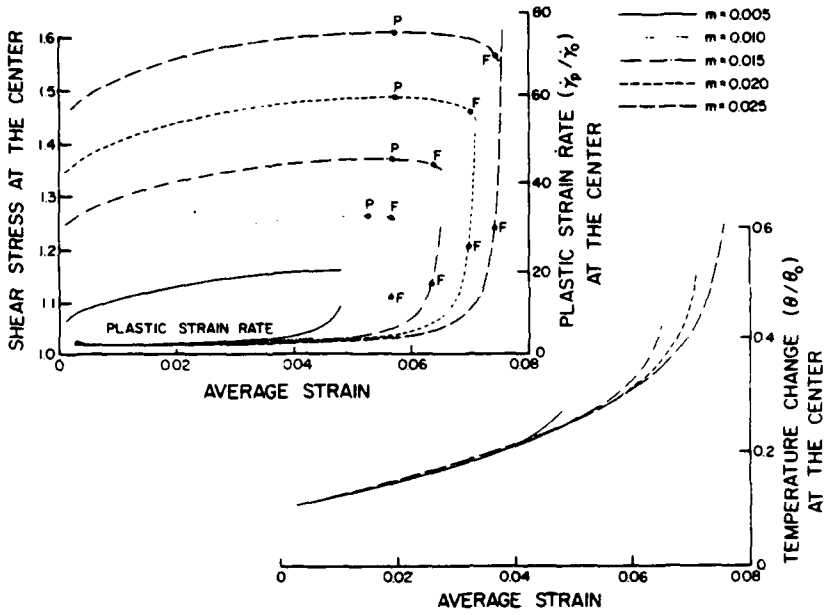

Fig. 3. Stress–strain curves and the evolution of the central plastic strain rate and temperature for different values of m.

Another way to alter viscous effects in the materials is to keep h fixed but change the rate sensitivity exponent m. The effect of this change in the value of m is depicted in Figs 3 and 4. Whereas an increase in the value of m from 0.005 to 0.015 resulted in higher values of the critical strains at which the peak P in the stress–strain curve occurs, subsequent increases in the value of m hardly changed the critical strain. However, the difference between the value of the average strains corresponding to point F when the explosive growth in the central plastic strain rate occurs and the point P increases with m. Our numerical results agree with the analytical results of Staker[3] and Clifton *et al.*[14] if we restrict ourselves to $m \geq 0.015$, a value typical for many metals. Clifton *et al.*[14] also noted

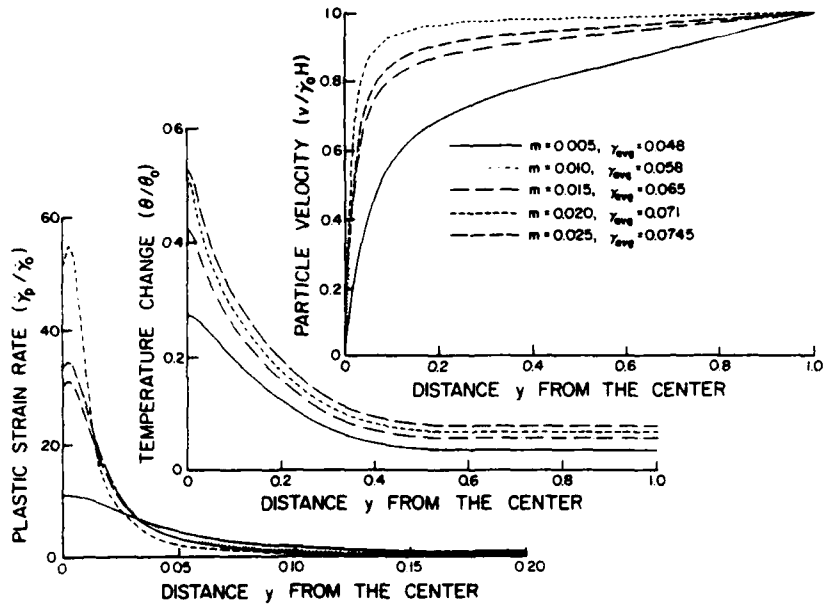

Fig. 4. Distribution of the temperature, particle velocity and plastic strain rate in the specimen for different values of m.

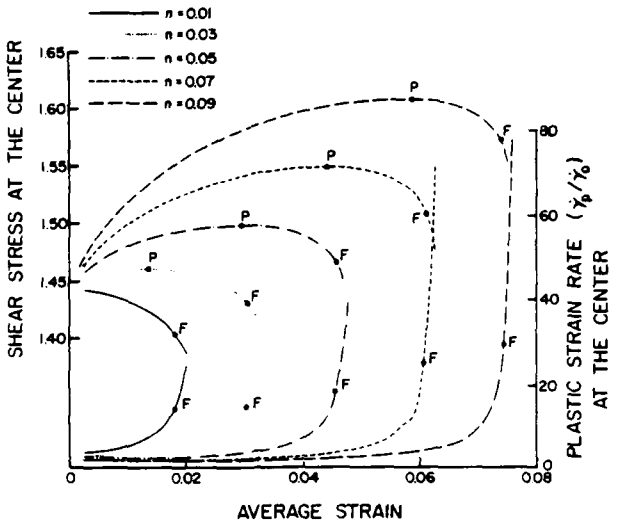

Fig. 5. Stress–strain curves and the evolution of the central plastic strain rate for different values of n.

that even though the critical strain may be insensitive to the value of m, subsequent growth of the instability will be affected by its value. At early times, the central temperature is unaffected by m. Curves representing the evolution of the central temperature more or less coincide until the temperature at the center begins a sharp rise. This behavior differs from that when the values of b were increased. Figure 4 depicts the distribution of the plastic strain rate, temperature and particle velocity through the thickness of the slab. Note that these curves do not correspond to the time when the shear band had fully developed in each case. Achieving that goal would have required sorting through a tremendous amount of computer output.

Figures 5 and 6 show results for different values of the strain-hardening exponent n. An increase in the value of n increases the strain at which the peak P in the stress–strain curve occurs and also the value of the strain at which the explosive growth in the central plastic strain rate occurs. Whereas Bai[5] and Staker[3] showed that the critical strain is proportional to n, our computed values of the critical strain divided by n gave 8.67, 11.4, 12.14, and 12.67 for $n = 0.03$, 0.05, 0.07, and 0.09, respectively. They assumed a parabolic type $(\gamma_p)^n$ hardening rule and we have represented this effect by $(1+\psi/\psi_0)^n$. Since $\psi_0 \ll 1$, our criterion will increase the flow stress more than the simple parabolic hardening rule will for the same amount of plastic deformation and identical values of n. In Fig. 6 are plotted the central temperature vs time or average strain, and the distribution of the particle velocity, temperature and plastic strain rate within the specimen. Again these plots of quantities vs the distance from the center are at different stages of the shear band development for different values of n. These depict that qualitatively there is no change in the way various field variables evolve in the specimen as the strain-hardening exponent is increased.

In Fig. 7 are plotted the shear stress at the center, the central plastic strain rate and the central temperatures vs the average strain for three different values of the thermal softening coefficient a. For $a = 0.000552$, no peak in the stress–strain curve occurred for strains up to 35%, and the central plastic strain rate grew at a snail's pace, the central temperature increased linearly with average strain and the particle velocity (cf. Fig. 8) had a linear variation through the thickness of the specimen. The temperature was slightly higher at the center than it was at the edge. To see if the increase in the amplitude of the temperature perturbation given by eqn (18a) would result in shear-strain localization, two more cases with the central amplitudes equal to 0.2 and 0.3 were tried. In neither case did the deformation localize. When similar numerical experiments were conducted with $a = 0.00552$, the deformation localized near the center at values of strain well below the

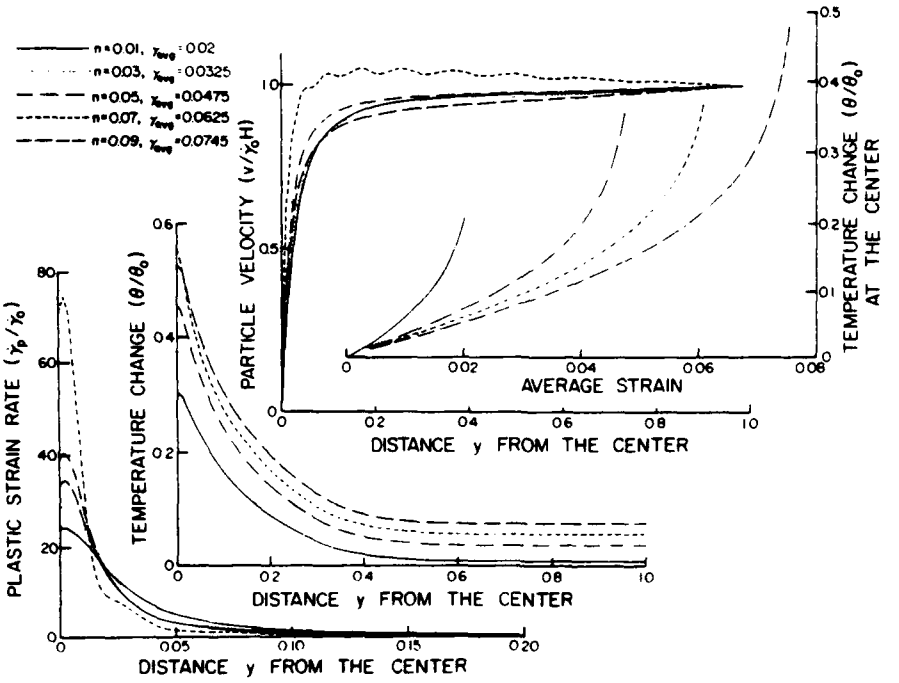

Fig. 6. Temperature change vs average strain and the distribution of the temperature change, plastic strain rate and particle velocity within the slab for different values of n.

ones at which the peak stress occurred. This supports the viewpoint that the existence of the peak in the stress–strain curve is a necessary condition for the deformation to localize.

The expressions for the critical strain derived by Staker[3] and Bai[5] imply that the critical strain is inversely proportional to the thermal softening coefficient a. When we halved the value of a from 0.005552 to 0.002776, the peak in the stress–strain curve occurred at an average strain of 0.0551 instead of 0.15. Whereas we have solved a complete set of equations both Staker and Bai approximated the change in temperature caused by plastic working. As in the other cases studied, the dramatic growth in the central plastic strain rate occurs at a value of strain well past the peak in the stress–strain curve. The width of the shear band is hardly affected by the value of the thermal softening coefficient a provided that the deformation does localize.

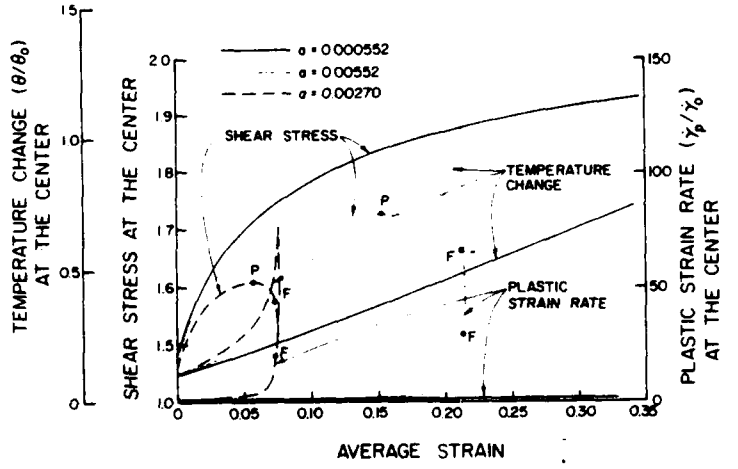

Fig. 7 Effect of the value of the thermal softening coefficient a on the growth of the central stress, plastic strain rate and temperature.

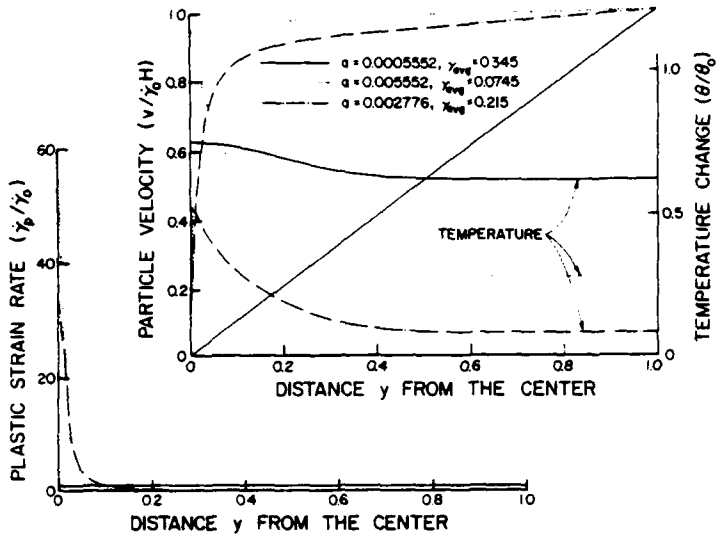

Fig. 8. Variation of the particle velocity, temperature and plastic strain rate within the specimen for different values of a.

Finally we investigated the effect of the thermal length by changing the value of the thermal conductivity k. We note that for the values of ρ, $\dot{\gamma}_0$ and H given in eqns (20), the non-dimensional thermal length decreases from 0.0631 to 0 when the values of thermal conductivity k are changed from 49.216 to 0. For values of k in this range, the stress–strain curves, plotted in Fig. 9, up to the peak stress are unaffected. However, beyond this peak the drop in the stress is slightly affected by the value of the thermal conductivity. Also the strain at which the explosive growth in the central plastic strain rate occurs increases slightly with an increase in the value of k. In Fig. 10 are plotted the variations of the plastic strain rate, temperature and particle velocity in the specimen. Again qualitatively there is no difference in these plots when the thermal conductivity is varied.

For all four values of the thermal length used, the band width came out to be 116 μm. In each case, the central plastic strain rate had reached a value of 80 times the applied strain rate. These results are in agreement with those of Wu and Freund[13] but disagree with the conclusions drawn by Merzer[11]. Note that the constitutive relation and the method of

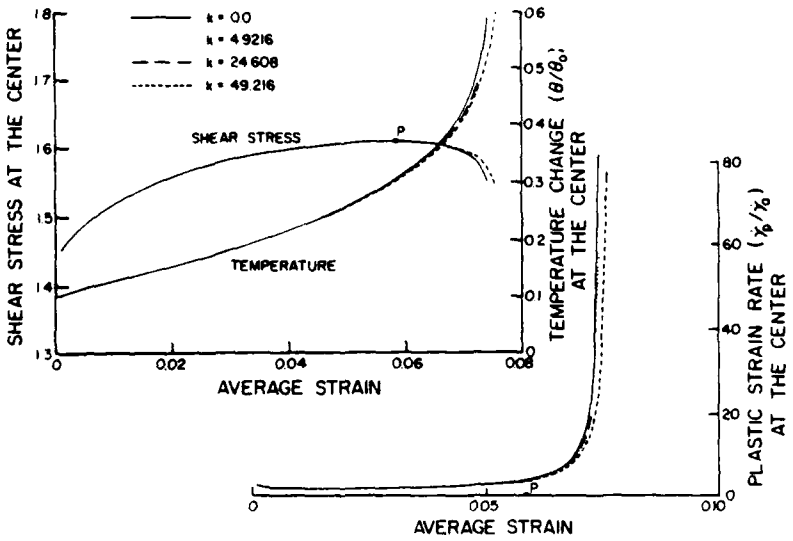

Fig. 9. Effect of the thermal conductivity on the growth of the central shear stress, temperature and the plastic strain rate.

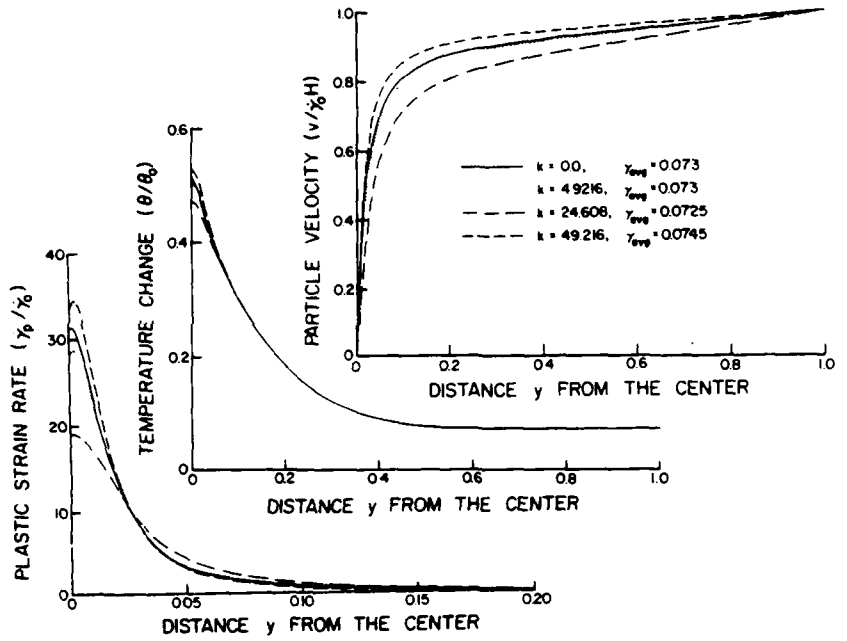

Fig. 10. Distribution of the plastic strain rate, temperature change and the particle velocity in the specimen at four different values of thermal conductivity.

studying the shear band development used herein are different from those employed by Merzer, and Wu and Freund.

CONCLUSIONS

The problem of shear strain localization in simple viscoplastic materials has been studied by using a constitutive relation proposed earlier by Wright and Batra[15]. A shear band is presumed to have formed if the addition of a temperature bump at the center of the specimen in the configuration in which it just deforms plastically results in the localization of the deformation. The complete set of coupled non-linear equations is integrated numerically by using the Galerkin–Crank–Nicolson method.

These numerical experiments reinforce the belief that the existence of a peak in the stress–strain curve is a necessary condition for the shear band to develop. The non-dimensional thermal length with values between 0 and 0.063 has little effect on the critical strain at which the peak in the stress–strain curve occurs, the strain at which the plastic strain rate at the center begins an extremely rapid rise and the width of the band. The critical strain did not come out to be inversely proportional to the thermal softening parameter as has been approximated in some theoretical studies. Even though values of the rate-hardening exponent m greater than 0.015 did not increase the value of the critical strain, the strains at which dramatic growth in the band development occurs did increase with m. Thus from a practical viewpoint, higher values of the strain-rate hardening exponent m, the viscous length and the strain hardening exponent n would delay the development of a shear band.

Finally we note that conclusions drawn herein are strictly applicable to the constitutive model used.

Acknowledgements—This work was supported by the ARO contract DAAG 29-85-K-0238 to the University of Missouri-Rolla.

REFERENCES

1. C. Zener and J. H. Hollomon, Effect of strain rate upon plastic flow of steel. *J. Appl. Phys.* **15**, 22 (1944).
2. R. F. Recht, Catastrophic thermoplastic shear. *J. Appl. Mech.* **31**, 189 (1964).
3. M. R. Staker, The relation between adiabatic shear instability strain and material properties. *Acta Metall.* **29**, 683 (1981).

4. R. J. Clifton, Adiabatic shear in material response to ultrahigh loading rates. NRC National Material Advisory Board (U.S.) Report NMAB-356 (Edited by W. Herrmann *et al.*), Washington, DC (1980).
5. Y. L. Bai, A criterion for thermoplastic shear instability. In *Shock Waves and High Strain-rate Phenomenon in Metals* (Edited by M. A. Meyers and L. E. Murr), pp. 277–284. Plenum Press, New York (1981).
6. T. J. Burns, Approximate linear stability analysis of a model of adiabatic shear band formation. *Q. Appl. Math.* **43**, 65 (1985).
7. J. Litonski, Plastic flow of a tube under adiabatic torsion. *Bull. Acad. Pol. Sci.* **25**, 7 (1977).
8. L. S. Costin, E. E. Crisman, R. H. Hawley and J. Duffy, On the localization of plastic flow in mild steel tubes under dynamic torsional loading. *Inst. Phys. Conf.* Ser. No. 47, 90 (1979).
9. G. R. Johnson, J. M. Hoegfeldt, U. S. Lindholm and A. Nagy, Response of various metals to large torsional strains over a large range of strain rates—Part 1: ductile metals. *ASME J. Engng Mater. Tech.* **105**, 48 (1983).
10. U. S. Lindholm and G. R. Johnson, Strain-rate effects in metals at large strain rates. In *Material Behavior under High Stresses and Ultrahigh Loading Rates* (Edited by J. Mexall and V. Weiss), pp. 61–79. Plenum Press, New York (1983).
11. A. M. Merzer, Modelling of adiabatic shear band development from small imperfections. *J. Mech. Phys. Solids* **30**, 323 (1982).
12. S. R. Bodner and Y. Partom, Mechanical properties at high rate of strain. *Inst. Phys. Conf.* Ser. No. 21, 102 (1975).
13. F. H. Wu and L. B. Freund, Deformation trapping due to thermoplastic instability in one-dimensional wave propagation. *J. Mech. Phys. Solids* **32**, 119 (1984).
14. R. J. Clifton, J. Duffy, K. A. Hartley and T. G. Shawki, On critical conditions for shear band formation at high strain rates. *Scripta Metall.* **18**, 443 (1984).
15. T. W. Wright and R. C. Batra, The initiation and growth of adiabatic shear bands. *Int. J. Plasticity* **1**, 205 (1985).
16. T. W. Wright and R. C. Batra, Further results on the initiation and growth of adiabatic shear bands at high strain rates. *J. Phys.* **46**, 323 (1985).
17. T. W. Wright and R. C. Batra, Adiabatic shear bands in simple and dipolar plastic materials. In *Proceedings of the IUTAM Symposium on Macro- and Micro-mechanics of High Velocity Deformation and Fracture*, Tokyo (August 1985).
18. R. C. Batra, The initiation and growth of, and the interaction among adiabatic shear bands in simple and dipolar materials. *Int. J. Plasticity* **3**, 75 (1987).
19. A. E. Green, B. C. McInnis and P. M. Naghdi, Elastic–plastic continua with simple force dipole. *Int. J. Engng Sci.* **6**, 373 (1968).
20. A. U. Sulijoadikusumo and O. W. Dillon, Jr., Temperature distribution for steady axisymmetric extrusion, with an application to Ti–6Al–4V: Part 1. *Thermal Stresses* **2**, 97 (1979); Part 2. *Ibid.* **2**, 113 (1979); Part 3. *Ibid.* **3**, 265 (1979).
21. W. S. Farren and G. I. Taylor, The heat developed during plastic extrusion of metal. *Proc. R. Soc.* **A107**, 422 (1925).
22. T. W. Wright, Some aspects of adiabatic shear bands. In *Metastability and Incompletely Posed Problems* Edited by S. Antman, J. L. Ericksen, D. Kinderlehrer and I. Müller), pp. 353–372. Springer, Berlin (1987).